

Sixteen overlooked open clusters in the fourth Galactic quadrant

A combined analysis of UBVI photometry and Gaia DR2 with ASteCA

G. I. Perren¹, E. E. Giorgi², A. Moitinho³, G. Carraro⁴, M. S. Pera¹, and R. A. Vázquez²

¹ Instituto de Astrofísica de La Plata (IALP-CONICET), La Plata, Argentina
e-mail: gabrielperren@gmail.com

² Facultad de Ciencias Astronómicas y Geofísicas (UNLP-IALP-CONICET), 1900 La Plata, Argentina

³ CENTRA, Faculdade de Ciências, Universidade de Lisboa, Ed. C8, Campo Grande, 1749-016 Lisboa, Portugal

⁴ Dipartimento di Fisica Astronomia Galileo Galilei, Vicolo Osservatorio 3, Padova, I-35122, Italy

Received November xx, 2019; accepted xxxx xx, 2019

ABSTRACT

Aims. This paper has two main objectives: (1) To determine the intrinsic properties of sixteen faint and mostly unstudied open clusters in the poorly known sector of the Galaxy at $270^\circ - 300^\circ$, to probe the Milky Way structure in future investigations. (2) To address previously reported systematics in Gaia DR2 parallaxes by comparing the cluster distances derived from photometry with those derived from parallaxes.

Methods. Deep UBVI photometry of 16 open clusters was carried out. Observations were reduced and analyzed in an automatic way using the ASteCA package to get individual distances, reddening, masses, ages and metallicities. Photometric distances were compared to those obtained from a Bayesian analysis of Gaia DR2 parallaxes.

Results. Ten out of the sixteen clusters are true or highly probable open clusters. Two of them are quite young and follow the trace of the Carina Arm and the already detected warp. The rest of the clusters are placed in the interarm zone between the Perseus and Carina Arms as expected for older objects. We found that the cluster van den Berg-Hagen 85 is 7.5×10^9 yrs old becoming then one of the oldest open cluster detected in our Galaxy so far. The relationship of these ten clusters with the Galaxy structure in the solar neighborhood is discussed. The comparison of distances from photometry and parallaxes data, in turn, reveals a variable level of disagreement.

Conclusions. Various zero point corrections for Gaia DR2 parallax data recently reported were considered for a comparison between photometric and parallax based distances. The results tend to improve with some of these corrections. Photometric distance analysis suggest an average correction of $\sim +0.026$ mas (to be added to the parallaxes). The correction may have a more intricate distance dependency, but addressing that level of detail will require a larger cluster sample.

Key words. Methods: statistical – Galaxies: star clusters: general – (Galaxy:) open clusters and associations: general – Techniques: photometric – Parallaxes – Proper motions

1. Introduction

Galactic open clusters are routinely used as probes of the structure and evolution of the Milky Way disk. Their fundamental parameters, like age, distance, and metallicity allow us to define the large scale structure of the disk and to cast light on its origin and assembly (Janes & Adler 1982; Moitinho 2010; Cantat-Gaudin et al. 2018). Young open clusters can be used to trace spiral arms and star forming regions (Moitinho et al. 2006; Vázquez et al. 2008), while older clusters are better probes of the chemical evolution of the thin disk (Magrini et al. 2009). The recent second release of Gaia satellite data (Gaia Collaboration et al. 2018) is producing a tremendous advance in the study of the Galactic disk and its star cluster population.

Basic parameters for a large number of clusters are now available with unprecedented accuracy (Cantat-Gaudin et al. 2018; Soubiran et al. 2018; Bossini et al. 2019; Monteiro & Dias 2019). Proper motions may be employed to select cluster members and parallaxes can be used to derive distances. However, in some cases Gaia parallax distances disagree with distances derived from other methods (i.e., photometric or spectrophotometric). It may occur that for short distances the photometric

and parallax distances yield similar results within the uncertainties (Cantat-Gaudin et al. 2018). But the situation is complex regarding the existence of a bias correction to be applied to Gaia parallaxes. The analysis of quasar measurements in Gaia DR2 by Lindegren et al. (2018) led to the determination of a global zero point correction to parallaxes of approximately 0.03 mas, with variations of a comparable size depending on magnitude, colour, and position. More recently, by analyzing a sample of stars Schönrich et al. (2019) have put in evidence that not only a parallax offset must be applied to Gaia data but also that exists a quasi linear dependence with distances. The study presented by Xu et al. (2019), who compared distances of a variety of astronomical objects between Gaia and VLBI parallaxes, also report a zero point parallax correction of ~ 0.075 mas. It is difficult to establish the critical distance at which Gaia parallax distances start diverging from values from other methods and the dependence of the bias on position, parallax or other measurements. The task of establishing distances and other essential parameters for open clusters using the Gaia data looks arduous, since other factors such as the interstellar absorption and the level of crowding of a given star cluster also play a role.

In this article we present a sample of sixteen catalogued star clusters (Dias et al. 2002) previously unstudied, located in a poorly known Galactic sector at approximately $270^\circ < l < 300^\circ$ along the galactic plane. With one exception, this is the first systematic study carried out for the clusters in our sample. In this sense, we provide CCD *UBVI* photometry complemented with data available from Gaia DR2. The purpose of this investigation is twofold. First, we look for a reliable estimation of the true nature of these objects. Gaia DR2 offers us a long sought opportunity since we can make our analysis more robust by combining ground-based *UBVI* CCD data with space-based astrometry (parallax, and proper motions) and photometry. Second, since distance is the main derived parameter for mapping the Galaxy's structure, we seek to understand and take into account the corresponding biases in Gaia DR2 parallaxes. In following studies we aim at investigating the structure of the Galactic disk in this region. Traces of the Perseus Arm coming from of the third Galactic quadrant would be expected, despite this arm being only prominent in the second quadrant. However, one must keep in mind that some of these clusters may be associated to the Carina Arm.

Analyzing this sector of the Galaxy has proved to be quite a challenging task since the extinction is particularly strong and variable. This makes it not only difficult to derive accurate basic parameters of a cluster but, even worse, to establish if a visual stellar aggregate is a physical cluster or simply a random enhancement of field stars produced by patchy extinction. For achieving these two purposes, we employed the Automated Stellar Cluster Analysis code (ASteCA; Perren et al. 2015) to derive clusters' fundamental parameters from *G-UBVI* data, and two Bayesian techniques to extract membership probabilities and distances from Gaia DR2. The sample of clusters studied in this paper is shown in Table 1 together with their galactic coordinates and their equatorial coordinates referred to the J2000.0 equinox.

The layout of the paper is as follows: in Section 2 we present the cluster sample. Section 3 is devoted to explain the observations and the reduction process of photometry. In Section 4 we describe the tools to analyze the photometric data and the method to connect Gaia DR2 with photometric results. A cluster by cluster report of the results obtained is presented in Section 5. In Section 6 three different corrections to Gaia DR2 parallax data are applied and discussed. Conclusions of the paper are given in Section 7.

2. The cluster sample

Table 1 lists the equatorial coordinates (α , δ) and galactic coordinates (l , b) of the 16 cluster fields studied here, ordered by increasing right ascension α . Equatorial coordinates refer to the J2000.0 equinox.

These objects form part of a long term joint effort aimed at studying the complicated structure of the Galaxy in the solar neighborhood. With this motivation, during the last decade we have been collecting and producing homogeneous *UBVI* observations of open clusters in the third Galactic quadrant (3GQ: $180^\circ \leq l \leq 270^\circ$) of the Milky Way. We understand that for a better interpretation of the galaxy structure from an optical point of view is essential to increase the number of these objects with well estimated parameters. In this fashion, we have contributed significantly to the present understanding of the spiral structure in this Galactic region (Carraro et al. 2005; Moitinho et al. 2006; Vázquez et al. 2008; Carraro et al. 2010). In this article we decided to focus in unknown open clusters placed between the end

Table 1. List of objects surveyed in the present article. Note: van den Bergh-Hagen clusters (van den Bergh & Hagen 1975) are indicated by vdBH. In a similar way Ruprecht (Ruprecht et al. 1996) and Trumpler (Trumpler 1930) clusters are mentioned as RUP and TR followed by the respective numbers.

Cluster name	α_{2000} hh:mm:ss	δ_{2000} dd:mm:ss	l °	b °
vdBH 73	09:31:56	-50:13:00	273.634	0.951
vdBH 85	10:01:52	-49:34:00	276.914	4.544
RUP 87	10:15:32	-50:43:00	279.372	4.883
RUP 85	10:01:33	-55:01:12	280.15	0.160
vdBH 87	10:04:18	-55:26:00	280.719	0.059
vdHB 92	10:19:07	-56:25:00	282.984	0.438
TR 12	10:06:29	-60:18:00	283.828	-3.698
vdBH 91	10:17:16	-58:42:00	284.03	-1.600
TR 13	10:23:48	-60:08:00	285.515	-2.353
vdBH 106	10:52:42	-54:14:00	286.048	4.700
RUP 88	10:18:55	-63:08:00	286.661	-5.186
RUP 162	10:52:54	-62:19:00	289.638	-2.545
Lynga 15	11:42:24	-62:29:00	295.053	-0.672
Loden 565	12:08:06	-60:43:12	297.65	1.710
NGC 4230	12:17:20	-55:06:06	298.025	7.445
NGC 4349	12:24:08	-61:52:18	299.719	0.830

of the 3GQ and 300 in galactic longitude, aimed at a similar purpose.

Positions of the clusters in the Galaxy are shown in Fig. 1 superposed onto the Aladin Sky Atlas DSS2 color image. Our sampling covers essentially the first 30 degrees of the fourth Galactic quadrant, from latitudes $l \sim 273^\circ$ to $l \sim 300^\circ$, encompassing the region around the Carina OB association and the south-east part of Vela with some objects in Crux and Centaurus.

3. Photometric observations

A first series of CCD *UBVI* photometry was carried out in 13 open clusters placed in the galactic region going from 270° to 300° in galactic longitude and from 7° to -5° in galactic latitude. This region covers the Carina Arm, the inter-arm region between the Perseus and Carina arms and also a part of the Local Arm. The observations were made on 9 nights in April and May 2002, using the YALO (Yale, AURA, Lisbon, OSU) ¹ facilities at Cerro Tololo Inter-american Observatory (CTIO). The images were taken with a 2048×2048 px CCD attached to the 1.0 m telescope and the set of *UBVI* filters. The field of view is $10' \times 10'$ given the $0.3''/\text{px}$ plate scale. All images were acquired using the ANDICAM ² which was moved to the 1.3 m CTIO telescope in 2003.

A second series of CCD photometry was implemented during on March 2010 at CTIO to get *UBVI* photometry in two other clusters, NGC 4349 and Lynga 15; both at a slightly larger galactic longitude (298°). Images in a first run were taken with the SMARTS 0.9 m telescope ³ using a 2048×2046 px Tek2K detector ⁴ with a scale $0.401''/\text{px}$ covering thus $13.6'$ on a side. A sec-

¹ <http://www.astronomy.ohio-state.edu/YALO/>

² <http://www.astronomy.ohio-state.edu/~depoy/research/instrumentation/andicam/andicam.html>

³ <http://www.ctio.noao.edu/noao/content/SMARTS-09-m-Telescope>

⁴ <http://www.ctio.noao.edu/noao/content/Tek2K>

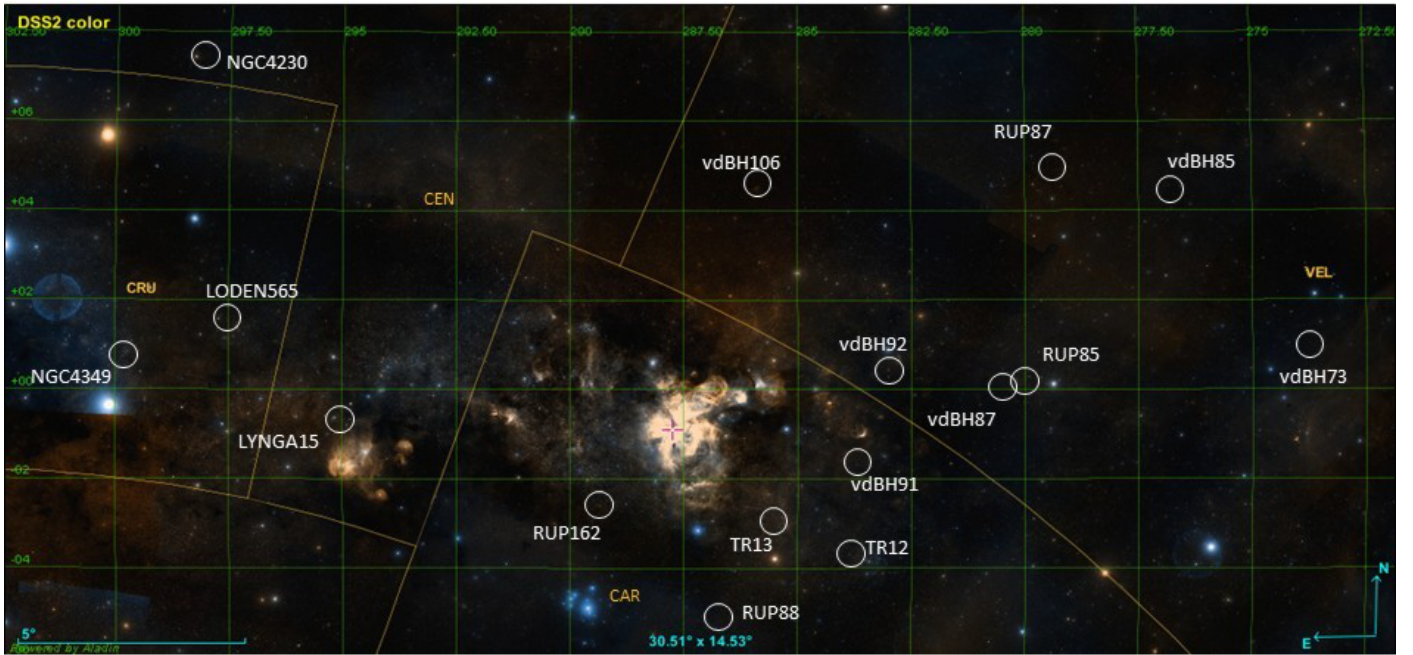


Fig. 1. DSS2 color Aladin image showing with white circles the position of the clusters surveyed in the present sample. The galactic coordinates l and b are depicted by a green grid while constellation limits for Carina, Vela, Centaurus and Crux appear in yellow lines.

ond run of images taken at the SMARTS 1.0 m telescope⁵ of the same clusters was carried out with a 4064×4064 px Y4KCam⁶ CCD with a scale of $0.289''/\text{px}$ thus covering $20' \times 20'$ on a side. The first run (at the 0.9 m) was not photometric, and therefore we tied all the images to the second run (at the 1.0 m), which was photometric. During this second run, we took multiple images of the standard star fields PG 1047 and SA98 (Landolt 1992).

Finally, in the year 2015 the open cluster vdBH 73, located at a smaller longitude ($\sim 273^\circ$) was observed in the *UBVI* filters with the 1.0 m Swope telescope⁷ at Las Campanas Observatory, Chile. On this occasion, direct images were acquired with the $4\text{K} \times 4\text{K}$ E2V CCD with a scale of $0.435''/\text{px}$ covering $29.7' \times 29.8'$.

Short exposures were always obtained to avoid bright star saturation in the frame. Notwithstanding, sometimes we could not help to lose very bright stars. Details of air masses, seeing values, and exposure times per filter and telescope can be seen in Table 2 for all the observations.

3.1. Photometric reduction process

The basic reduction of the CCD science frames has been done in the standard way using the IRAF 4 package *ccdred*. The photometry was performed using IRAF's DAOPHOT (Stetson 1987; Stetson et al. 1990) and *photcal* packages. Aperture photometry was performed to obtain the instrumental magnitudes of standard stars and some bright cluster stars. Profile-fitting photometry was performed in each program frame by constructing the corresponding point spread function. The zero-point of the

instrumental magnitudes for each image was determined with aperture photometry and growth curves.

The transformation equations to convert instrumental magnitudes into the standard system were always of the form:

$$\begin{aligned} u &= U + u_1 + u_2 xX + u_3 x(U - B), \\ b &= B + b_1 + b_2 xX + b_3 x(B - V), \\ v &= V + v_1 + v_2 xX + v_3 x(B - V), \\ i &= I + i_1 + i_2 xX + i_3 x(V - I) \end{aligned} \quad (1)$$

where u_2, b_2, v_2, i_2 are the extinction coefficients computed for each night and X is the air-mass. No color dependence of higher order was found for either filter.

In each case detector coordinates were cross-matched with Gaia astrometry to convert pixels into equatorial α and δ for the equinox J2000.0, thus providing Gaia-based positions for the entire cluster catalog. This process was performed in three steps. First the Astrometry.net⁸ service was used to assign (α, δ) coordinates to the brightest stars in our observed frames. The second step involves employing our own code called *astrometry*⁹ to apply a transformation from pixel to equatorial coordinates to all the observed stars, using the coordinates already assigned to the brightest stars matched in the previous step. The algorithm in this code applies the affine transformation method developed by J Elonen¹⁰ based on the work by Späth (2004). The transformation equations are of the form $\alpha = c_0 + c_1 x + c_2 y$ where α is the right ascension, (x, y) are the pixel coordinates, and the c_X coefficients are fitted (similarly for δ , more details in the code's site). Finally, in the third step we use another one of our open source codes called *CatalogMatch*¹¹ to cross match our frames (which by now have equatorial coordinates assigned) with Gaia DR2¹² data. The matching tolerance used here ranges from 2

⁵ <http://www.ctio.noao.edu/noao/content/SMARTS-10-m-Telescope>

⁶ <http://www.ctio.noao.edu/noao/content/y4kcam>

⁷ <http://www.lco.cl/telescopes-information/henrietta-swope/telescope-control-system/telescopes-information/henrietta-swope/instruments/>

⁸ <http://astrometry.net/>

⁹ <https://github.com/Gabriel-p/astrometry>

¹⁰ <https://elonen.iki.fi/code/misc-notes/affine-fit/>

¹¹ https://github.com/Gabriel-p/catalog_match

¹² <https://www.cosmos.esa.int/web/gaia/dr2>

Table 2. Log of observations at YALO (CTIO) and Las Campanas. Reference for the telescopes used: 1 (1.0 m YALO), 2 (0.9 m, 1.0 m SMARTS), 3 (1.0 m Swope). Air masses and seeing are averaged values for the short and long exposures.

Cluster	Date	Telescope	U	B	V	I
(airmass, seeing ["], short exp/long exp [sec])						
vdBH 73	06/2015	3	1.2, 2.8, 50/150	1.2, 2.8, 20/60	1.17, 2.0, 15/45	1.16, 2.43, 15/45
vdBH 85	04/2002	1	1.09, 1.7, 30/300	1.07, 1.7, 5/200	1.07, 1.5, 3/160	1.14, 1.6, 1/120
RUP 87	04/2002	1	1.14, 1.9, 30/300	1.11, 1.7, 5/200	1.09, 2.0, 3/160	1.07, 1.6, 1/120
RUP 85	04/2002	1	1.11, 2.5, 30/300	1.11, 2.1, 5/200	1.11, 1.9, 3/160	1.13, 1.7, 1/120
vdBH 87	04/2002	1	1.11, 2.2, 30/300	1.11, 2.5, 5/200	1.12, 2.0, 3/160	1.14, 1.7, 1/120
vdBH 92	05/2002	1	1.12, 1.9, 60/300	1.12, 1.9, 20/200	1.12, 2.0, 10/160	1.12, 1.8, 10/120
TR 12	04/2002	1	1.19, 1.7, 30/300	1.17, 1.8, 5/200	1.16, 1.6, 3/160	1.16, 1.5, 1/120
vdBH 91	05/2002	1	1.14, 2.1, 60/300	1.14, 2.0, 20/200	1.15, 2.0, 10/160	1.17, 1.8, 10/120
TR 13	05/2002	1	1.17, 1.8, 60/300	1.16, 1.6, 20/200	1.16, 1.6, 10/160	1.16, 1.4, 10/120
vdBH 106	05/2002	1	1.10, 2.3, 60/300	1.11, 2.3, 20/200	1.13, 2.1, 10/160	1.15, 2.1, 10/120
RUP 88	05/2002	1	1.19, 2.2, 60/300	1.19, 2.1, 20/200	1.2, 2.0, 10/160	1.21, 1.8, 10/120
RUP 162	05/2002	1	1.18, 1.6, 60/300	1.19, 1.6, 20/200	1.0, 1.5, 10/160	1.2, 1.4, 10/120
Lynga 15	03/2010	2	1.19, 1.9, 5/2400	1.25, 1.9, 3/1800	1.28, 1.19, 3/1100	1.27, 1.19, 3/1100
Loden 565	05/2002	1	1.16, 1.9, 60/300	1.17, 1.7, 20/200	1.17, 1.7, 10/160	1.19, 1.6, 10/120
NGC 4230	05/2002	1	1.11, 2.1, 60/300	1.12, 1.8, 20/200	1.13, 1.8, 10/160	1.16, 1.6, 10/120
NGC 4349	03/2010	2	1.18, 1.8, 5/2400	1.18, 1.6, 3/1800	1.18, 1.5, 3/1100	1.18, 1.4, 3/1100

to 4 arcsec, with mean minimum/maximum differences in the matches of 0.3 and 0.9 arcsec respectively (for all the observed frames).

With the exception of the cluster NGC 4349, the rest of the objects in our sample have no dedicated photometric studies. Notwithstanding we could perform a comparison of our photometry in V , B , and $(B - V)$ with available photometry from APASS DR10 (The AAVSO Photometric All-Sky Survey¹³) that has a magnitude limit near 18 mag (enough to identify the presence of RGB stars), and Gaia DR2. In this comparison we have put special care in those clusters belonging to the observing runs in 2002 since they are mostly very faint.

For APASS data, we downloaded a region centered on each observed frame and cross-matched it with our data, taking care of removing bad matches by enforcing a tolerance of 0.7 arcsec in the matches for all the frames (this value was selected because it gave a reasonable number of matches with a minimum of bad-match contamination).

We also compared our photometry with that from Gaia DR2 using the Carrasco photometric relationships¹⁴ between the Johnson-Cousins system and Gaia passbands. The process requires to transform the G magnitude into V and B magnitudes through the transformation equations provided there. For the V filter we employed the $(G - V)$ vs $(BP - RP)$ polynomial. For the B filter there is no similar polynomial presented, so we fitted our own using the same list of cross-matched Landolt standards used by Carrasco.¹⁵ This third degree polynomial is:

$$G - B = 0.003[0.009] - 0.64[0.02] (BP - RP) - 0.42[0.03] (BP - RP)^2 + 0.067[0.007] (BP - RP)^3 \quad (2)$$

where the values in brackets are the standard deviations of each coefficient, and the RMS of the residuals is $\sigma \sim 0.066$. As a

result of applying these two polynomials we obtain transformed G magnitude values into V_{Gaia} and B_{Gaia} magnitudes, which we can use to compare with our own V and B magnitudes directly.

The results are shown in Table 3 where the ΔV , ΔB and $\Delta(B - V)$ columns display the mean differences between our photometry and APASS DR10/Gaia DR2 data for all the observed regions. In each frame the groups of stars to compare were selected according to the filter criteria imposed by Carrasco: $G < 13$, $\sigma_G < 0.01$. The mean differences for V , B and $(B - V)$ combining all the frames are shown in Fig 2. Although there are no visible trends, there are offsets in the V and B magnitudes between our photometry and APASS of ($\Delta V = -0.07 \pm 0.07$, $\Delta B = 0.06 \pm 0.08$) and between our photometry and Gaia of ($\Delta V = -0.03 \pm 0.04$, $\Delta B = -0.01 \pm 0.08$). The reason for the differences found for the offsets between our data and APASS/Gaia arises from the fact that APASS DR10 has itself an offset with Gaia DR2 of ($\Delta V = 0.04 \pm 0.07$, $\Delta B = 0.05 \pm 0.10$), in the sense (Gaia - APASS). These values were found cross-matching APASS data (for the regions where our 16 frames are located) directly with Gaia data, and applying the mentioned transformations for the G magnitude into V , B . In any case, these offsets are not relevant because we only use the $(B - V)$ color in the analysis so that the offsets tend to compensate each other and result in a smaller value of ~ 0.015 mag. The effect that this $(B - V)$ offset in our photometry has on the estimated photometric distances will be addressed in Sect 6.

Figure 3 shows the CCD V images of the clusters areas where we have carried out the photometric surveys. The series of panels shown from upper left to the lower right are ordered by increasing longitude and labeled with the cluster name inserted in every panel. Equatorial decimal coordinates, α and δ , for the J2000.0 equinox are shown in each panel as reference for the reader.

Final tables containing star number, x,y detector coordinates and α , δ equatorial coordinates together with magnitude and colors are accessible in separate form for each cluster at Vizier¹⁶.

¹³ <https://www.aavso.org/apass>

¹⁴ https://gea.esac.esa.int/archive/documentation/GDR2/Data_processing/chap_cu5pho/sec_cu5pho_calibr/ssec_cu5pho_PhotTransf.html

¹⁵ This list was kindly provided by Carrasco upon our request. We thank Dr Carrasco very much for sharing this data.

¹⁶ <http://vizier.u-strasbg.fr/viz-bin/VizieR?-source=XXX>

Table 3. Mean differences between APASS and the Carrasco transformation polynomials and our own photometry. The columns named N show the number of stars used to estimate these values for each cluster.

Cluster	APASS				Gaia			
	ΔV	ΔB	$\Delta(B - V)$	N	ΔV	ΔB	$\Delta(B - V)$	N
vdBH 73	-0.07 ± 0.05	-0.04 ± 0.05	0.03 ± 0.03	301	-0.03 ± 0.03	-0.01 ± 0.07	0.01 ± 0.07	95
vdBH 85	0.01 ± 0.04	0.03 ± 0.05	0.03 ± 0.04	32	0.01 ± 0.02	0.02 ± 0.07	0.00 ± 0.07	11
RUP 87	-0.02 ± 0.05	0.01 ± 0.09	0.02 ± 0.07	41	0.00 ± 0.02	0.00 ± 0.03	0.00 ± 0.04	17
RUP 85	-0.04 ± 0.05	-0.02 ± 0.10	0.02 ± 0.08	36	-0.01 ± 0.02	0.02 ± 0.03	0.03 ± 0.03	22
vdBH 87	-0.03 ± 0.05	-0.02 ± 0.06	0.01 ± 0.04	37	-0.02 ± 0.03	0.02 ± 0.06	0.04 ± 0.08	18
vdBH 92	-0.06 ± 0.05	-0.05 ± 0.06	0.01 ± 0.04	34	-0.02 ± 0.04	0.02 ± 0.07	0.03 ± 0.04	20
TR 12	-0.07 ± 0.07	-0.07 ± 0.07	0.00 ± 0.05	37	-0.01 ± 0.04	-0.03 ± 0.09	-0.02 ± 0.07	29
vdBH 91	-0.06 ± 0.06	-0.04 ± 0.09	0.02 ± 0.05	81	-0.01 ± 0.02	0.00 ± 0.04	0.01 ± 0.05	33
TR 13	-0.13 ± 0.10	-0.08 ± 0.07	0.05 ± 0.05	38	-0.04 ± 0.03	0.01 ± 0.10	0.04 ± 0.10	42
vdBH 106	-0.07 ± 0.08	-0.07 ± 0.08	-0.01 ± 0.06	44	-0.01 ± 0.01	-0.04 ± 0.04	-0.03 ± 0.04	12
RUP 88	-0.06 ± 0.05	-0.04 ± 0.07	0.02 ± 0.04	44	-0.01 ± 0.01	-0.02 ± 0.06	-0.01 ± 0.06	29
RUP 162	-0.16 ± 0.14	-0.13 ± 0.19	0.04 ± 0.10	20	-0.02 ± 0.05	0.02 ± 0.14	0.04 ± 0.11	28
Lynga15	-0.08 ± 0.08	-0.09 ± 0.06	-0.01 ± 0.07	98	-0.06 ± 0.04	-0.06 ± 0.09	0.00 ± 0.07	53
Loden 565	-0.03 ± 0.04	-0.02 ± 0.07	0.00 ± 0.04	43	-0.01 ± 0.03	0.01 ± 0.04	0.02 ± 0.04	23
NGC 4230	-0.03 ± 0.04	0.00 ± 0.06	0.03 ± 0.04	23	-0.03 ± 0.02	0.02 ± 0.10	0.05 ± 0.10	11
NGC 4349	-0.11 ± 0.08	-0.10 ± 0.09	0.01 ± 0.07	296	-0.05 ± 0.04	-0.03 ± 0.09	0.02 ± 0.08	131

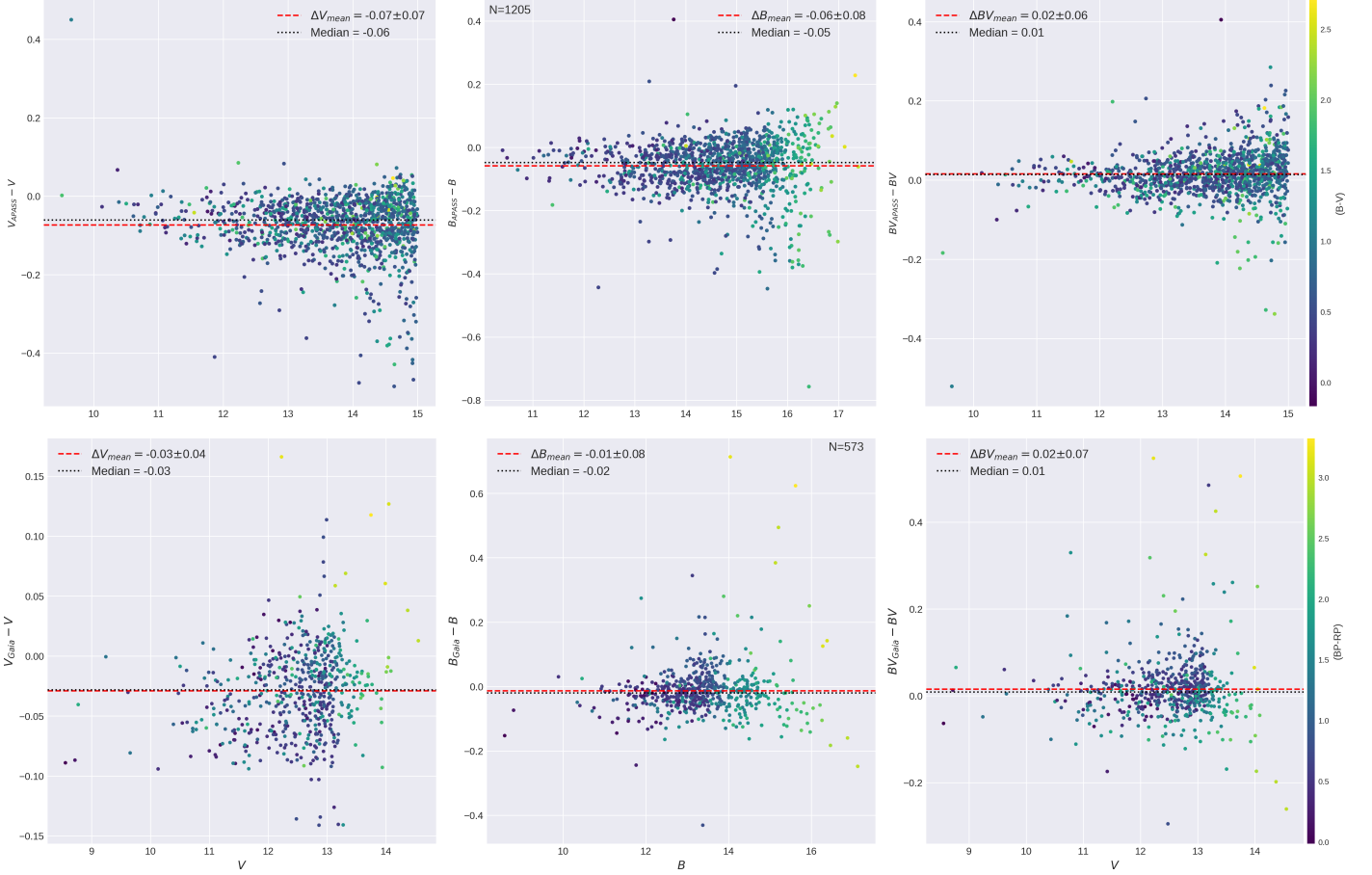


Fig. 2. Top row: differences between the APASS DR10 data for the V (left), B (center) magnitudes and $(B - V)$ color (right) and our own photometry. Bottom row: same for Gaia DR2 data versus our photometry. Details in the text.

4. Photometric data analysis process: Gaia data and the ASteCA code

For analyzing the large number of objects studied in this paper in a systematic, reproducible and homogeneous way, we have used

the ASteCA code¹⁷. The main goal of this code is to put the user apart, as much as possible, from the analysis of a stellar cluster to derive its fundamental parameters. We shall limit ourselves to give a brief summary about the way the positional and photometric data are employed by the code. A complete description of

¹⁷ <http://asteca.github.io/>

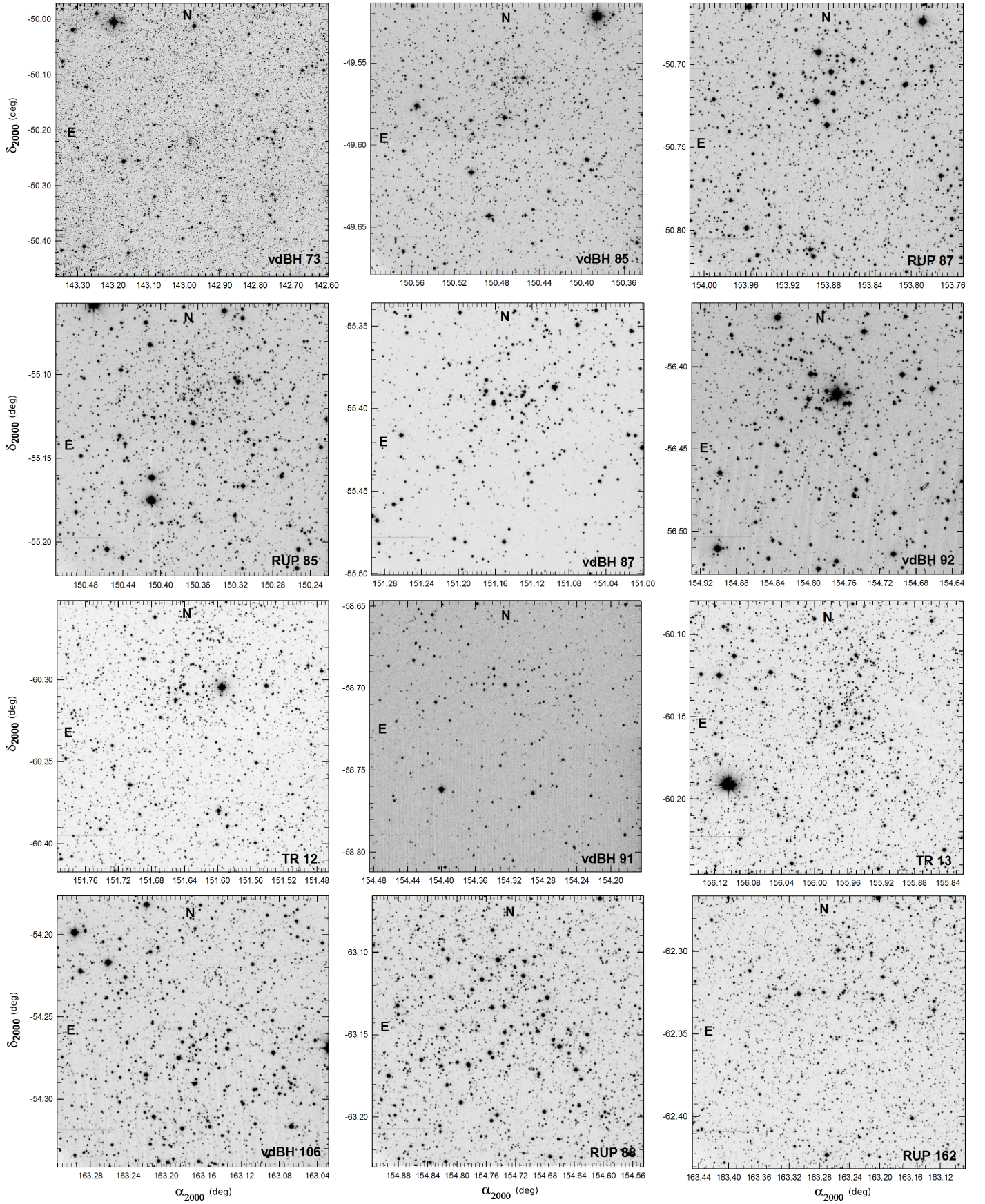


Fig. 3. The V images (charts) of the observed clusters (names inserted) ordered from top to bottom and from left to right by increasing longitude. Decimal α and δ coordinates for the 2000 equinox are indicated. North and East are also shown.

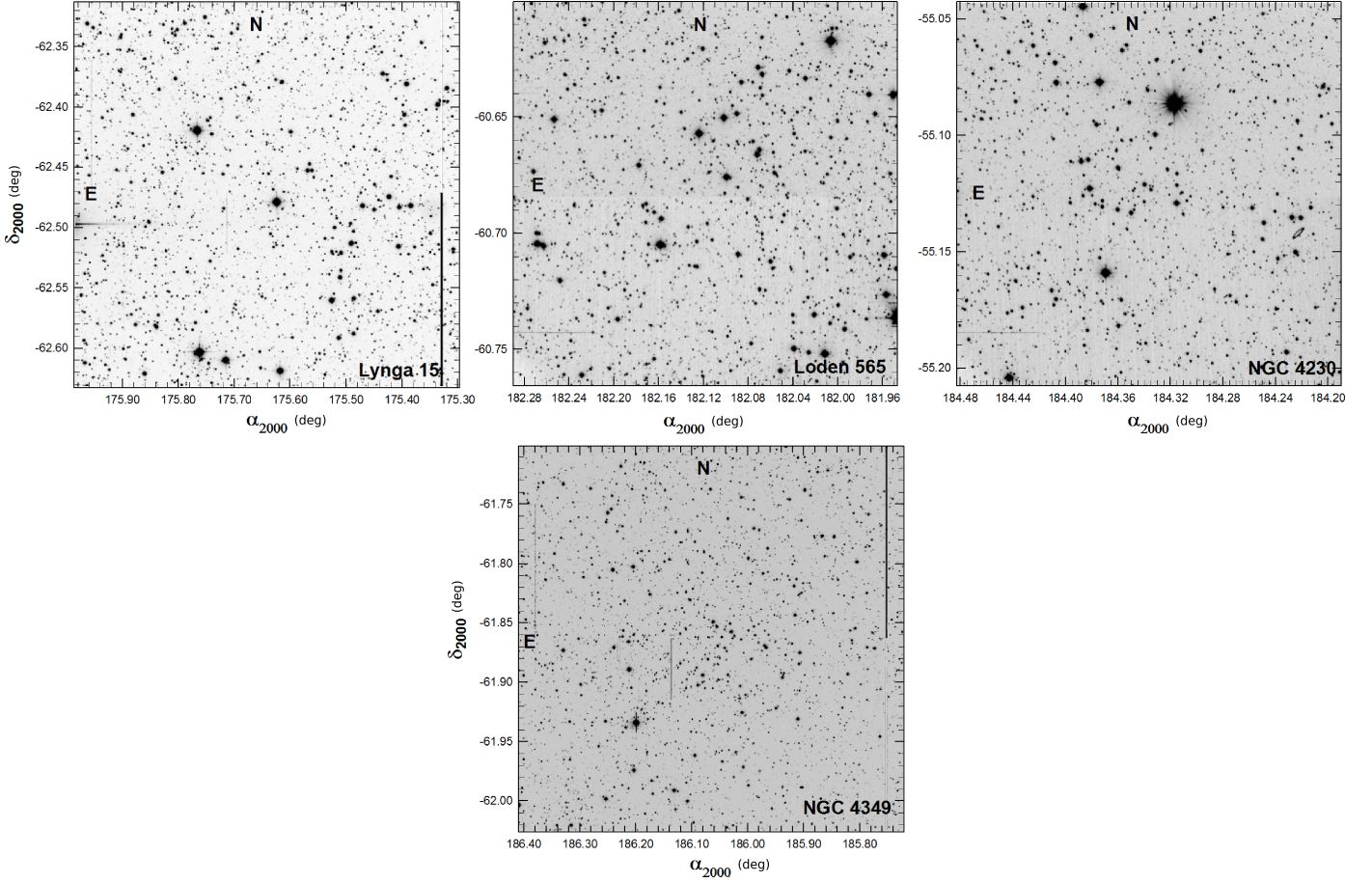


Fig. 3. Continued

the analysis carried out by AStECA can be found in Perren et al. (2015) and Perren et al. (2017). The basic hypothesis of any stellar cluster analysis is that the region occupied by a real cluster and the surrounding field should show “a priori” different properties. This is, we should see an increase in the star density (not always true) where a cluster is supposed to exist; the kinematic properties of cluster members should differ from similar ones for the surrounding region; members of a cluster must be at a same distance while non members may show all kind of distances; the photometric diagrams composed by members of a cluster should follow a well defined star sequence while field stars should not.

4.1. Gaia data

The second data release for the Gaia mission (Gaia Collaboration et al. 2018) was presented on April 2018 with improved coverage, particularly for the five-parameter astrometric solution. We crossed-match our complete set of photometric data with those of Gaia DR2 and employed Gaia’s G magnitude, parallax, and proper motions in our analysis as described in Sect 4.2.

No uncertainty-based cut-off has been done on Gaia DR2 parallax or proper motion data following the advice given in Luri et al. (2018), where the authors explain that even parallaxes with negative values or large uncertainties carry important information. Negative values in the parallax data were thus kept during the processing. The parallax values were processed with a Bayesian approach to get an independent estimate of the distance to each cluster. In this approach, the model for the cluster is taken from the accompanying tutorial by Bailer-Jones on inferring the

distance to a cluster via astrometry data¹⁸. The full model (i.e., the likelihood in the Bayesian approach) can be written as:

$$P(\{\varpi\}|r_c) = \prod_{i=1}^N \int \int \frac{1}{2\pi\sigma_{\varpi_i}s_c} \exp\left[-\frac{1}{2}\left(\frac{(\varpi_i - 1/r_i)^2}{\sigma_{\varpi}^2} + \frac{(r_i - r_c)^2}{s_c^2}\right)\right] dr_i ds_c \quad (3)$$

where $\{\varpi\}$ is the set of all parallax values (our data), N is the number of processed stars in the cluster, ϖ_i and σ_{ϖ_i} are the parallax value and its uncertainty for star i , r_i is the distance to that star in parsec, s_c is a shape parameter that describes the size of the cluster, and r_c the distance to the cluster (the parameter we want to estimate). Our model marginalizes not only over the individual distances (r_i ; as done in the original model by Bailer-Jones) but also over the shape parameter (s_c), estimating only the overall cluster distance r_c using the parallax value and its uncertainty for each star in the decontaminated cluster region (the membership probabilities process is described with more detail in Sect. 4.2). The prior for the distance in the Bayesian model is a Gaussian centered at a maximum likelihood estimate of the distance to the cluster region, with a large standard deviation (1 kpc). This maximum likelihood was obtained through a Differential Evolution algorithm built into *scipy*¹⁹, applied on Eq. 3,

¹⁸ <https://github.com/agabrown/astrometry-inference-tutorials>

¹⁹ https://docs.scipy.org/doc/scipy/reference/generated/scipy.optimize.differential_evolution.html

i.e., the model. The results of this analysis will be shown in Sect 5 and discussed in Sect. 6.

We include in our analysis a two-sample Anderson-Darling test,²⁰ comparing the distribution of Gaia parallax and proper motions, between the cluster and the estimated stellar field regions, to quantify how “similar” these two regions are among each other. The results of the test in each case are indicated with AD and the corresponding p-value²¹ in Fig 7 and the similar figures for the remaining clusters. The p-value indicates at what significance level the null hypothesis can be rejected. This is, the smaller the p-value, the larger the probability for the cluster region of being a true physical entity rather than a random clustering of field stars. When using parallax and proper motions three p-values are generated that are combined into a single p-value using Fisher’s combined probability test²².

4.2. The way ASteCA works

Since the first release of ASteCA the code has grown considerably. The purpose of the tool and the core set of analysis it is able to perform are still properly described in Perren et al. (2015), although several modifications have been implemented since. The most relevant changes include the ability to combine parallax and proper motion data in the membership analysis algorithm, which was initially purely photometric. This means one can currently use up to 7 dimensions of data in this process: magnitude, three colors, parallax, and proper motions.

The several tasks performed by ASteCA can be roughly divided into three main, independent analysis blocks: structural study including the determination of a cluster region identified primarily by an overdensity, individual membership probability estimation for stars inside the overdensity, and the search for the best fit parameters.

The first block estimates center and radius values that define in each case the cluster region. Robust estimations of these two quantities can only be achieved when a clear overdensity and a large number of members are detected. If a cluster is not clearly defined as an overdensity on the observed frame and if its boundaries are weakly established, ASteCA allows center and radius to be manually fixed since the automatic procedure may return incorrect values. We have chosen to fix all radii values manually since many of our observed frames are structurally sparse and with a low number of members, and display very noisy radial density profiles (hereafter RDP).²³ Every point of the RDP was obtained by generating rings around the center defined for the potential cluster, i.e., the comparison field. In the present case the comparison field may contain between 1 and 10 regions of equal area to that of the cluster, depending on the cluster area and the available size of the remaining of the frame. In each ring the found number of stars (with no magnitude cut applied) is divided by the respective area to get a value

of the radial density. For the computation of the density level of the field (foreground/background), outliers in the RDP are iteratively discarded to avoid biasing the final value. This procedure is repeated until converging to an equilibrium value, equivalent to the density of the star field at a given distance from the potential cluster center.

King profile (King 1962) fittings have been performed in those cases when a fit could be generated. No formal core or tidal radius are given because their values, due mainly to the shape of the RDP, were not within reasonable estimates (the process to fit the King profiles to the RDP returned either large and unrealistic values, or values with very large uncertainties). This could be due to the non-spheric geometry of sparse open clusters combined with the field contamination within the cluster region. Although photometric incompleteness is not taken into account in the generation of the RDP, these are not clusters largely affected by crowding; thus we do not expect this to have a major effect on the estimated radii.

The second block assigns membership probabilities to the defined cluster region, an often disregarded process in simpler cluster studies, and removes the most probable field stars that contaminate this region. By itself, an over-density does not guarantee the presence of a real cluster; many times an overdensity is generated by random fluctuations in the field star density. To avoid such a mistake a comparison of the properties for cluster and field stars must be done. Ideally, we look for firm evidence of the presence of a cluster sequence at some evolutionary stage. ASteCA employs a Bayesian algorithm to compare the photometric, parallax, and proper motions distribution of the stars in the cluster region with a similar distribution in the surrounding field areas (Perren et al. 2015). Initially the analysis was carried out in an N-dimensional data space that combined the G magnitude, parallax, and proper motions from Gaia, with colors from our own photometry: $(V - I)$, $(B - V)$, $(U - B)$. In this case thus, the data space where the algorithm works is characterized by $N=7$. Combining all the available data is though not always optimal. A data dimension can sometimes introduce noise in the analysis instead of helping disentangle members from field stars. In our case we found that using parallax and proper motions, i.e., $N=3$, resulted in more clearly defined cluster sequences than if we included photometric dimensions (with $N=7$ as mentioned above).

Briefly, the algorithm compares the properties of this N-dimensional data space, for stars inside (cluster region) and outside (field region) the adopted cluster limits. All the data dimensions are previously normalized (to prevent any dimension from out-weighting others) and 4 sigma outliers are rejected. The position of every star inside the cluster in this data space is compared against each star in all the defined equivalent-area field regions, assuming a Gaussian probability density (centered at the given values for each data dimension, with standard deviations given by the respective uncertainties). This procedure is repeated hundreds or thousands of times (defined by the user) each time selecting different stars to construct an approximation of the clean cluster region. The outcoming result of this algorithm are thousands of probability values that are averaged to a final single membership probability value for each star within the cluster region.

This block ends with the cleaning of the photometric diagrams in the cluster region. Each cluster region photometric diagram is divided into cells, and the same is done for the equivalent diagram of the field regions. The star density number found in the field is then subtracted from the cluster photometric diagram, cell by cell, starting with stars that have low mem-

²⁰ https://docs.scipy.org/doc/scipy/reference/generated/scipy.stats.anderson_ksamp.html

²¹ The null hypothesis (H_0) is the hypothesis that the distributions of the two samples are drawn from the same population. The significance level (α) is the probability of mistakenly rejecting the null hypothesis when it is true, also known as Type I error. The p-value indicates the α with which we can reject H_0 . The usual 5% significance level corresponds to an AD test value of 1.961, for the case of two samples.

²² https://docs.scipy.org/doc/scipy/reference/generated/scipy.stats.combine_pvalues.html

²³ The radii values are estimated using the frames in pixels coordinates, and then converted to arcmins.

bership probabilities. Therefore, the final cluster photometric diagrams contain not only star membership assignation but it is also cleaned from the expected field star contamination. This two-step process is of the utmost importance to ensure that the fundamental parameters analysis that follows is performed on the best possible approximation to the cluster sequence (particularly when the cluster contains few members).

Finally, the third block performs the cluster's parameters estimation through the minimization of a likelihood function (Dolphin 2002) employing a genetic algorithm numerical optimization (Charbonneau 1995). This last stage includes the assignment of uncertainties for each fitted parameter via a standard bootstrap method (Efron & Tibshirani 1986). Again, all of these processes are described in much more detail in Perren et al. (2015) and Perren et al. (2017).

It is worth noting that, unlike other tools (e.g.: Yen et al. 2018), ASteCA does not fit isochrones to cluster sequences in photometric diagrams. Instead, it fits synthetic clusters generated from a set of theoretical isochrones, a given initial mass function, and completeness and uncertainties functions estimated directly from the observations. These synthetic clusters are represented as two or three-dimensional color-magnitude diagrams, depending on the number of photometric colors available in our observations. The “best fit” isochrones shown in green in the photometric diagrams shown in Fig 6 for vdBH85 (and similar figures for the rest of the clusters) are there for convenience purposes only as a way to guide the eye.

The code makes use of the PARSEC v1.2S (Bressan et al. 2012) theoretical isochrones (obtained from the CMD service²⁴), and the Kroupa (2002) form for the initial mass function. A dense grid of isochrones with fixed z and $\log(\text{age})$ values is requested to the CMD service²⁵, which are later on used in the fundamental parameters estimation process. The full processing yields five parameters: metallicity, age, extinction, distance, and mass, along with their respective uncertainties. The binary fraction was always fixed to 0.3, a reasonable estimate for open clusters (Sollima et al. 2010). As for the final mass of each cluster, although the values are corrected by the effects of star loss due to photometric incompleteness at large magnitudes and the percentage of rejected stars with large photometric uncertainties, it is not corrected by the dynamical mass loss due to the cluster's orbiting through the Galaxy. Hence, it should be regarded as a lower limit on the actual initial mass value.

From a practical point of view the code proceeds as follows to estimate the cluster's parameters. Firstly, individual three dimensional G vs $(B - V)$ vs $(U - B)$ photometric diagrams are analyzed fixing the metallicity to a solar value ($z = 0.0152$) in order to reduce the dimensionality of the parameter space, and thus its complexity. Although several of the aforementioned diagrams contain, in the present case, a rather small number of stars due to the presence of the U filter, they are very useful to get reddening and thus extinction via the inspections of the $(U - B)$ vs $(B - V)$ diagrams (e.g., Vázquez et al. 2008).

The individual $E(B - V)$ values in each region were always checked against maximum values given by the Schlafly & Finkbeiner (2011) maps²⁶. The only information extracted from this first step, and in particular by inspection of the $(U - B)$ vs

$(B - V)$ diagram, is thus a reasonable range for the $E(B - V)$ parameter. Secondly, the analysis of the G vs $(B - V)$ vs $(V - I)$ diagram is carried out restricting now the reddening space to the $E(B - V)$ range obtained previously, while still fixing the metallicity to solar value. We get from this process estimates for the age, distance, and cluster mass. Finally, in a third stage the parameter ranges derived above are applied including now the metallicity as a free parameter. As a result of the entire procedure, we obtain a five parameter best model fit for each observed cluster, along with the associated one sigma uncertainties for each one. In all the cases we have adopted $R = A_v/E(B - V) = 3.1$ to produce absorption-free distance moduli.

During the maximum likelihood and bootstrap processes, each observed cluster is compared to $\sim 2 \times 10^7$ synthetic clusters. This number is obtained combining those synthetic clusters generated in the maximum likelihood and bootstrap processes, by varying the fundamental parameters values.

5. Cluster-by-cluster discussion on structural and intrinsic parameters provided by ASteCA

We now present the results from the spatial and photometric analysis carried out with ASteCA, together with the outcome of the application of the Anderson-Darling test that compares parallax and proper motion distributions in cluster regions with their respective field regions. It is important to emphasize that the code will always fit the best possible synthetic cluster to a given star distribution, no matter we face a true open cluster or not.

Our sample contains clusters with a large variety of properties: some are robust, bright, well detached from the cluster background and therefore with a clearly defined main sequence (TR 13, TR 12, NGC 4349, vdBH 87, vdBH 92), others are clusters which are faint, with sparse star population and easy to confuse with the background (vdBH 73, vdBH 85, vdBH 106, RUP 162, RUP 85). Therefore, given the amount of figures to be shown in this paper we decided to add them to an Appendix, and limited ourselves here to present the case of three extreme types of cluster according to the statement above: a poorly defined (vdBH 85), a well-defined (NGC 4349) and a not cluster (RUP 87).

5.1. van den Bergh-Hagen 85

The open cluster vdBH 85 appears in the sky slightly east of the center of the Vela constellation. The V chart in Fig. 3 shows a weak star concentration near the north side of the observed field extending a little bit to the south east. The color-color and color-magnitude diagrams (from now on CCD and CMDs respectively) of the entire field of view in Fig. 4 is just a dispersed star distribution ending in a compact accumulation at $(B - V) = 1$ and below $G = 17$ mag approximately. Another clear feature is a structure at $G = 16$ mag in the two CMDs and for $1.2 < (B - V) < 1.7$ mag, resembling a red clump.

Figure 5 represents the spatial analysis carried out by ASteCA. This is: results from the search of a stellar overdensity, the mean value for the stellar field density, the respective King profile attempting to fit the radial density profile, and the assumed radius. ASteCA detected here an overdensity not easily seen in Fig. 3, standing out from the stellar background contained in a radius of 2.2 arcmins. It is characterized by a smooth RDP with nearly six times the background density at its

²⁴ <http://stev.oapd.inaf.it/cgi-bin/cmd>

²⁵ Grid values: z range [0.0005, 0.0295] with a step of 0.0005; $\log(\text{age})$ range [7, 9.985] with a step of 0.015

²⁶ Through the NASA/IPAC service <https://irsa.ipac.caltech.edu/applications/DUST/>

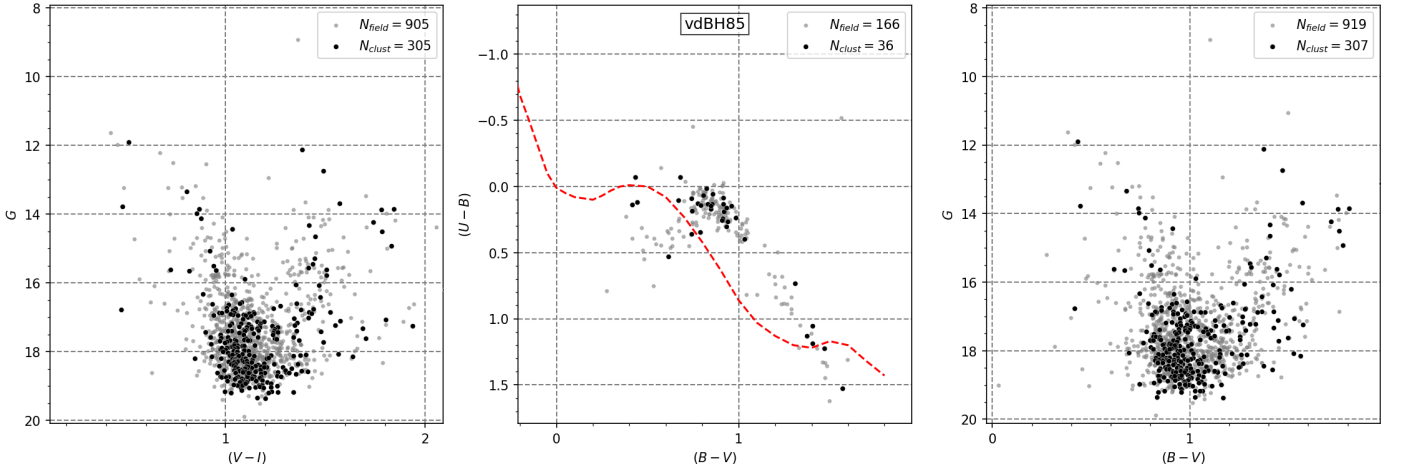


Fig. 4. From left to right: The G vs $(V - I)$, $(B - V)$ vs $(U - B)$, and V vs $(B - V)$ diagrams for all the stars observed in the region of van den Bergh-Hagen 85. The red dashed line in the two color diagram gives the position of the ZAMS (Aller et al. 1982). Insets in each diagram contain the number of stars in the cluster region (N_{clust} , black circles) and the surrounding field (N_{field} , grey circles)

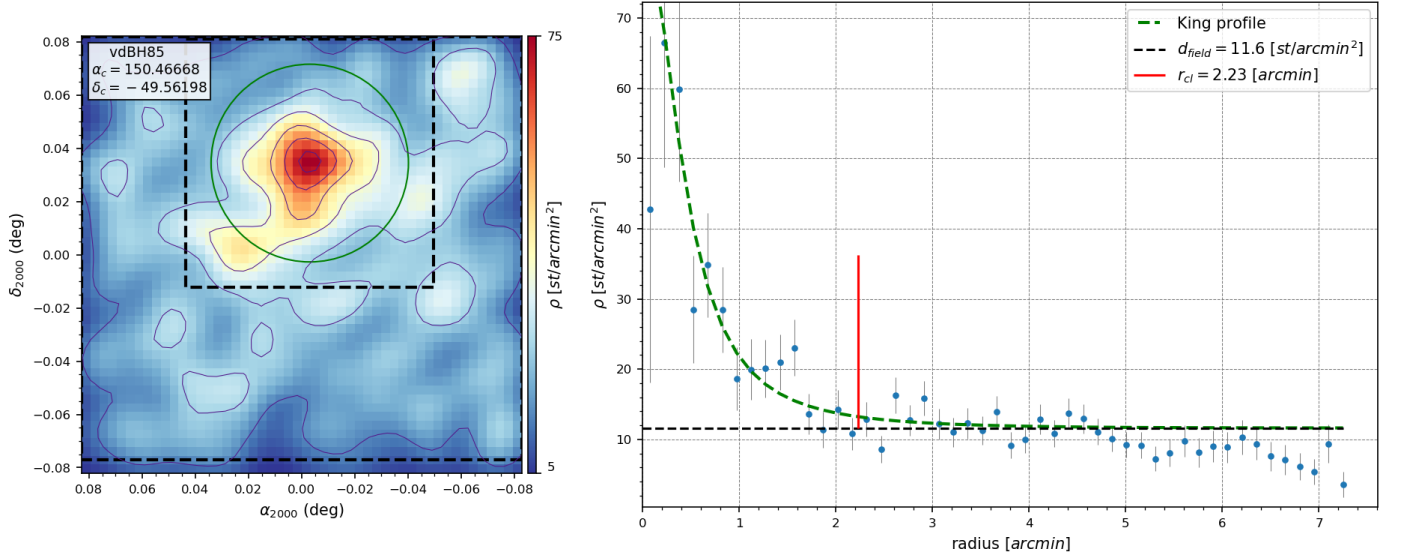


Fig. 5. From left to right. First panel: Contour plot showing the position of the overdensity associated to vdBH 85. Green inner circle gives the cluster size while the two black dashed lines squares enclose the region used for ASteCA to estimate the field stars properties. The lower density values at the frame's borders are an artifact of the kernel density estimate method employed to generate the density maps. Equatorial coordinates in decimal format are indicated. The colorbar denotes the star number per square arcmin (linear scale). These values are slightly different from those in the panel to the right because they are obtained with a different method (nearest neighbors). Second panel: The RDP is shown as blue dots with standard deviations shown as vertical black lines. King profile is shown in dashed green line. The horizontal black line is the mean field star density. Vertical red line is the adopted cluster radius.

peak, as shown in Fig. 5.

In the following step the removal of interlopers by comparison with the background field properties yields the field decontaminated CCD $(U - B)$ vs $(B - V)$ and CMDs, G vs $(B - V)$ and G vs $(V - I)$. This removal is performed comparing the star density on the cluster region's photometric diagram (whose stars already have membership probabilities provided by ASteCA) with that of the surrounding field regions. These diagrams are shown in Fig. 6. We insert in the mid panel of this figure the results from the best synthetic cluster fitting to the field decontaminated diagrams. In these three panels we show as well the isochrone curves from which the best synthetic cluster fit was generated. These isochrones are generated using the maximum likelihood values found for the metallicity and age, through averaging of

theoretical isochrones taken from the employed grid. Again, this is just to guide the eye since ASteCA does not fit isochrones.

Once the membership probabilities are established and the removal of field interlopers is done, the two CMDs of all stars show a short but evident main sequence below $G = 17$ mag. Three magnitudes above the cluster turn-off, at $G = 14$ mag a handful of stars appear, possibly part of the bright end of the giant branch. The comparison with the best fitting of a synthetic cluster throws the following characteristics for vdBH 85:

- a) the cluster is seen projected against a stellar field with moderate to low color excess. The best value corresponds to $E(B - V) = 0.3$ in correspondence with the maximum value of 0.46 mag stated by S&F2011.

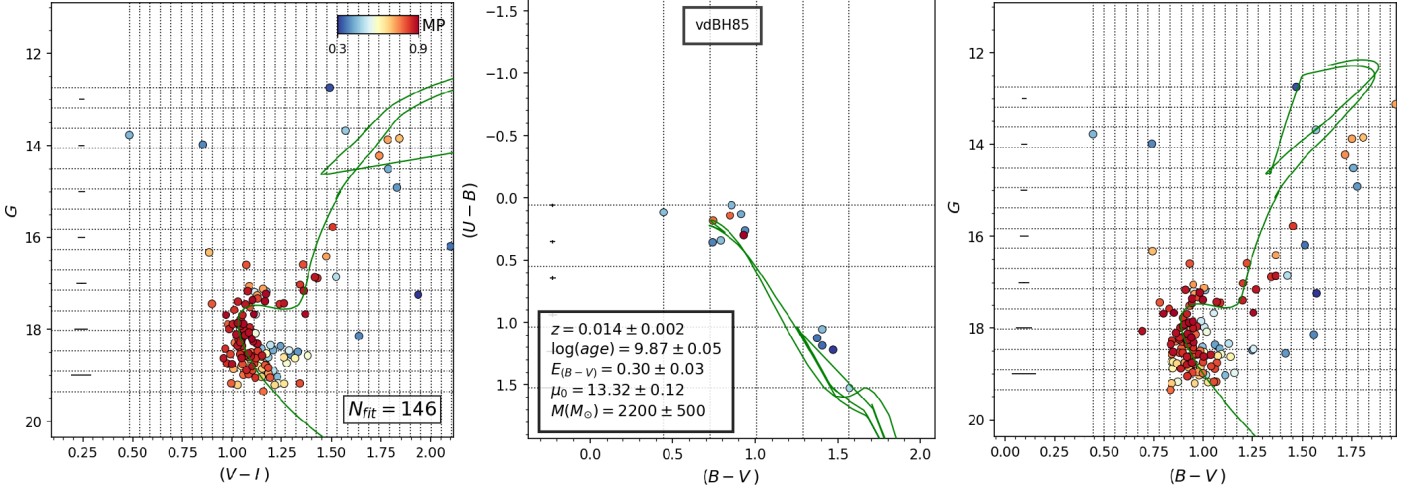


Fig. 6. From left to right: The G vs $(V - I)$, $(B - V)$ vs $(U - B)$, and G vs $(B - V)$ clean diagrams after the removal by field interlopers made by ASteCA over vdBH 85. The color of each star reflects its membership probability. Corresponding values are in the color bar at the upper right corner in the G vs $(V - I)$ diagram (left) labeled MP. The CCD in the middle will always show fewer stars due to the use of the U filter. Inset at the lower right corner in the G vs $(V - I)$ diagram shows the number of stars used by ASteCA to compare with synthetic clusters. Inset in the mid panel includes the final results for metallicity, $\log(\text{age})$, $E(B - V)$, the corrected distance modulus, and the cluster total mass provided by ASteCA. The green continuous line in the three diagrams is a reference isochrone. In particular, the green line in the color-color diagram, mid panel, shows the most probable $E(B - V)$ value fitting found by ASteCA.

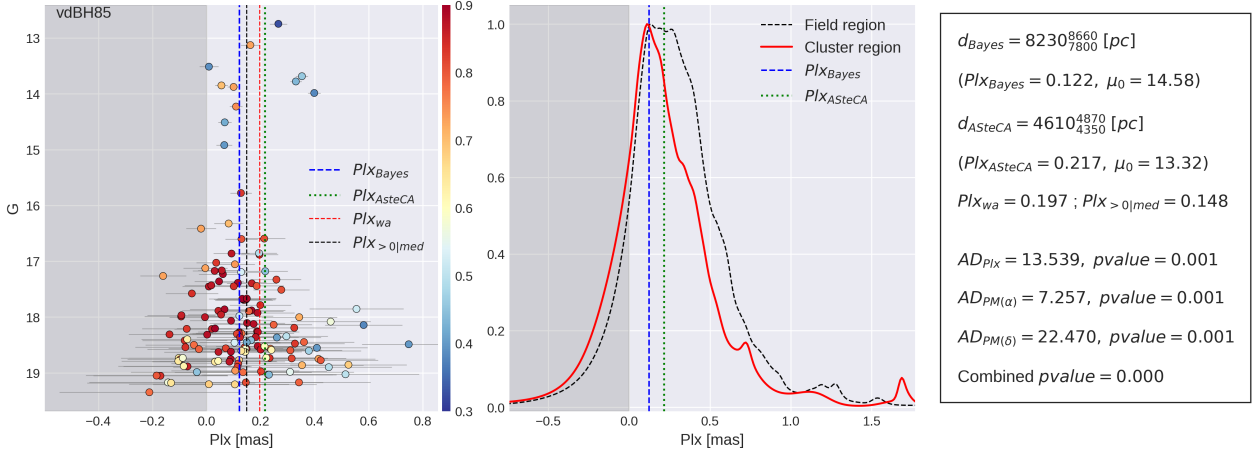


Fig. 7. Left panel: distribution of parallax for all stars with membership probabilities in the cleaned cluster region, as a function of the apparent magnitude G (vertical color scale is for the star membership probability) in vdBH 85. Horizontal bars are the parallax errors as given by Gaia. The different parallax value fittings are shown by dashed lines of different colors: blue is the Bayesian parallax estimate, green is ASteCA's photometric distance, red is the weighted average, and black is the median (without negative values). The mid panel is a normalized comparison between the parallax distributions inside the cluster region (red line) and outside it (dashed black line). The frame at the right summarizes the distances in parsecs according to the Bayesian analysis (d_{Bayes}) and ASteCA (d_{ASteCA}) followed by the parallax corresponding value, Plx , and corrected distance modulus (μ_0). Both fittings are indicated by the vertical blue and green dashed lines. The last four text lines in the right panel are the AD values for Plx , $PM(\alpha)$, $PM(\delta)$ followed by the corresponding p -values and, finally the combined p -value.

- b) The free absorption distance modulus of vdBH 85 is 13.32 ± 0.12 mag which implies a distance of 4.61 ± 0.26 kpc from the Sun. This fact explains by itself the extreme weakness of the cluster members.

Figure 7, finally, includes three panels. The left one shows the G mag vs Gaia parallax values (uncertainties indicated by horizontal bars) of cluster members, colored according to the estimated membership probabilities (colorbar to the right). The Bayesian distance (d_{Bayes}) found by the code is shown here by a vertical blue dashed line, the equivalent ASteCA distance (d_{ASteCA}) with a green dotted line, the weighted average with a red dashed line (where the weights are the inverse of the parallax errors), and the naive estimate of obtaining the median of

stars with parallax values greater than zero with black dashed line. The mid panel is the kernel density estimate of stars in the surrounding field region and the cluster region, in black and red lines respectively. For the Anderson-Darling test we used all the stars within the cluster region with Gaia data. In the right panel we summarize the distances in parsecs and errors, (d_{Bayes}) and d_{ASteCA} , followed by the corresponding parallax value, Plx , and corrected distance modulus, μ_0 . Both fittings are indicated by the vertical blue and green dashed lines. The final four text lines in the right panel are the AD values for Plx , $PM(\alpha)$, $PM(\delta)$ from the Anderson-Darling test, followed by the corresponding p -values and finally the combined p -value.

The distance estimated with parallax data from Gaia is almost 4 kpc larger than the one obtained through the photometric

analysis. This is most likely a failure of the Bayesian inference method employed, due to the large uncertainties associated to most of the probable cluster members. Further discussion is presented in Sect. 6. The Anderson-Darling test results in Fig. 7 suggest the null hypothesis can be safely rejected given the combined p -value of 0.0. The Plx , $PM(\alpha)$ and $PM(\delta)$ results from the Anderson-Darling test leave no doubt in the sense that cluster region and the surrounding comparison field come from quite different star populations.

We conclude that this object is a real and very old cluster, the oldest in our sample, approximately $7.50 \pm 0.80 \times 10^9$ yrs old. This age puts vdBH85 among the top ten oldest clusters cataloged in the WEBDA²⁷ and DAML²⁸ (Dias et al. 2002) databases.

5.2. NGC 4349

This is an object in the Crux constellation, placed slightly south of its geometric center. At first glance, the V image in Fig. 3 shows a distinguishable star accumulation. The overall photometric CCD and CMDs in Fig. 8 show a prominent star sequence emerging at $G \approx 15$ mag from the usual stellar structure produced by galactic disc stars. The CCD makes more evident the presence of a reddened but compact sequence of blue stars placed immediately below the first knee of the intrinsic line. Apart from this, other bluer stars appear for $(U - B)$ values smaller than 0.0.

ASteCA analysis revealed an extended overdensity of up to 70 stars per square arcmin. The observed frame's density map shows two regions with very distinct mean stellar densities of background. This is just an artifact generated by combining observations made with two different telescopes, as detailed in Sect. 3, and is the reason why the RDP shows such a strange shape, as seen in Fig. 9. We settle for a radius of ~ 4 arcmin, which seems to contain most of the overdensity, and limit the analysis to the inner frame. The ASteCA estimation of memberships shows that inside the adopted cluster radius the probable members of the cluster detach easily from the field region stars. This is shown in the respective CCD and CMDs of Fig. 10. If attention is drawn to the largest probabilities there appears in the three diagrams a somewhat narrow cluster sequence. In these cases (i.e., when a cluster sequence can be clearly defined down to the low mass region) probable members can be identified selecting a minimum probability value. We used $P > 70\%$ which produces a reasonably clean sequence with an appropriate number of estimated members.

Comparison with synthetic clusters yielded that NGC 4349 is a cluster with the following properties:

- A color excess of $E(B - V) = 0.41$ is found for the best fitting synthetic cluster. Since the maximum color excess provided by S&F2011 in this location is 2.83 one concludes that most of the absorption is produced behind the position of NGC 4349.
- The absorption free distance modulus of NGC 4349 is 11.38 ± 0.11 mag, placing it at a distance of $d = 1.88 \pm 0.05$ kpc from the Sun.

NGC 4349 is the only cluster in our sample with previous photographic photometry in the UBV system performed by

Lohmann (1961). Given the usual large differences between photographic and CCD photometry we performed no comparison between the Lohmann data-set and ours. According to Lohmann (1961), NGC 4349 is located at a distance of $d = 1.7$ kpc, almost 200 pc below our estimate. However, coincidences in terms of reddening, size and background star density have been found since Lohmann stated a cluster reddening of $E(B - V) = 0.38$ and similar cluster size. On the other hand, the Kharchenko Atlas²⁹ (Kharchenko et al. 2005) gives a reddening value of $E(B - V) = 0.38$ which is similar to ours with a distance reported of $d = 2.1$ kpc, slightly above our estimate.

The distance found for this cluster using Gaia parallax data with no applied offset (processed with the Bayesian method described in Sect. 4.1) is 2.04 ± 0.03 kpc, just 160 pc larger than the photometric distance found by ASteCA. Notice in Fig. 11 that this distance was obtained respecting the membership selection, thus ensuring that both analysis (the photometric analysis and this one) are performed over the exact same set of stars.

Parallax and proper motion distributions were tested using the Anderson-Darling statistics. With the exception of the comparison in the case of $PM(\delta)$ (where both samples, cluster and field, seem to come from the same distribution at a critical value just above 5%) the remaining two tests report quite different samples confirming, together with the photometric results, the true nature of NGC 4349.

High probability values for stars inside the overdensity and a clearly traced cluster sequence confirm the true nature of this object since the over density and the density profile are followed by a very well defined and extended photometric counterpart. Since all these facts are self-consistent, we are confident that NGC 4349 is an open cluster $0.29 \pm 0.09 \times 10^9$ years old. The Kharchenko Atlas gives quite a similar value for the cluster age, reporting $\log(t) = 8.32$ equivalent to 0.21×10^9 yrs.

5.3. Ruprecht 87

RUP 87 is in the east side of the Vela constellation. According to the respective Fig. 3 there is no relevant feature but a rather poorly populated stellar field with a few bright stars seemingly grouped towards the Northern portion of the frame. The photometric diagrams in Fig. 12 show no appreciable stellar structure defining the presence of an open cluster. The few stars with $(U - B)$ measures plotted in the respective CCD resemble that of a typical galactic field dominated by a handful of late F - and G -type stars followed by a pronounced tail of red stars presumably of evolved types. Stars in the region $0 < (U - B) < 0.5$ and $0 < (B - V) < 0.6$ could be reddened early A - or/and late B -types.

Accordingly, after many essays ASteCA could not define the presence of an overdensity as obviously seen in Fig. 13. The inability of our code to identify any overdensity simply means that the potential locus occupied by the cluster RUP 87 is not unambiguously separated from the field background stars. Lacking a clear overdensity we define the cluster region as that encircled by the green line, i.e., the sector containing the apparently grouped bright stars. The RDP emerging from this analysis is quite noisy.

Comparing the density of the defined cluster region with that of the remaining stellar field, the approximate number of probable members turns out to be around 20 stars. When dealing with (purported) clusters with such a low estimated number of members it is important to be extremely careful with the selection of

²⁷ <https://webda.physics.muni.cz/>

²⁸ <http://cdsarc.u-strasbg.fr/viz-bin/cat/B/ocl>

²⁹ <https://webda.physics.muni.cz/cocd.html>

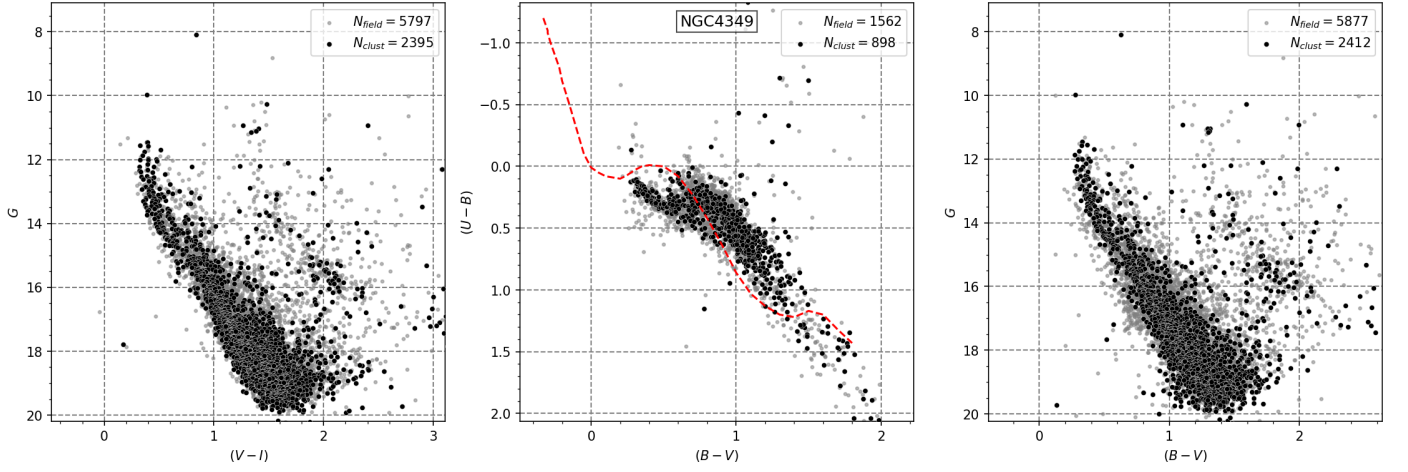


Fig. 8. Idem Fig. 4 for NGC 4349.

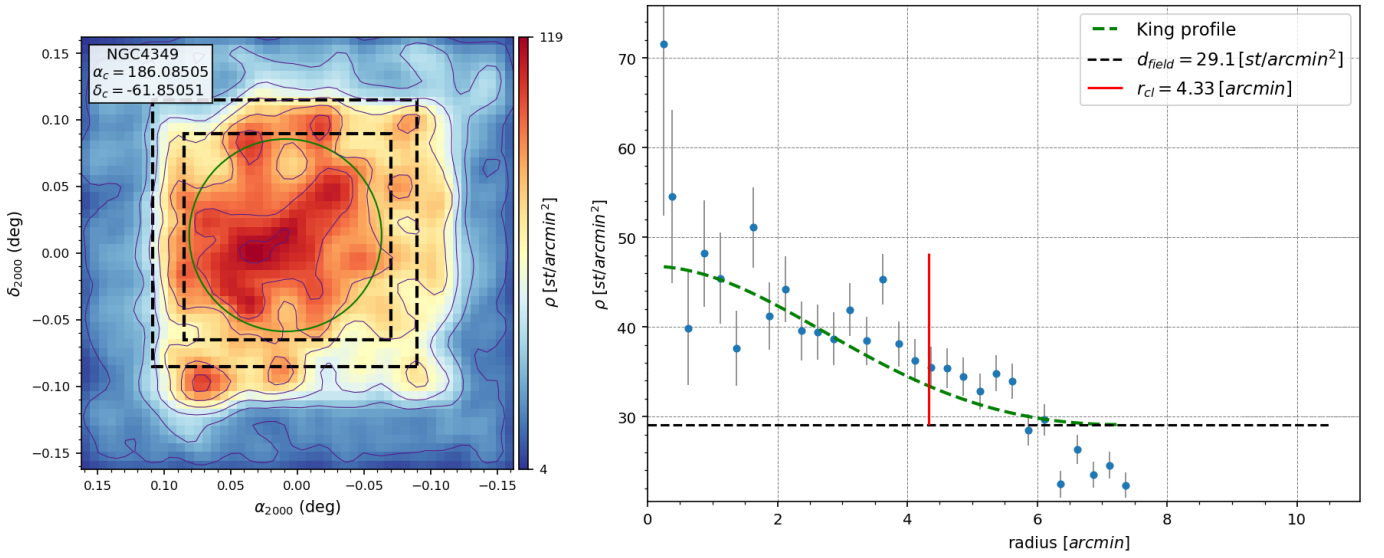


Fig. 9. Idem Fig. 5 for NGC 4349.

stars considered to be “members”. If we were to simply select a small group of stars within a similar parallax range and analyzed their photometric diagram with AStECA, we will probably obtain a somewhat reasonable fit. This is because the code will always find the most likely solution, no matter how dispersed the photometric diagram we give it might be. If we a priori hand-pick a few stars with a common distance (parallax values), they will be fitted by a synthetic cluster with a very similar distance modulus as that defined by the selected parallax values, and some “best fitted” values for the remaining parameters. Similarly the naive selection of stars with probabilities larger than 0.5 is not appropriate most of the times (unless a clear sequence can be defined, as in the case of NGC 4349), since this selection is biased towards brighter stars. This is because low mass stars not only have larger associated uncertainties, they are also located in denser regions of the CMDs. This makes them much more likely to be assigned lower membership probabilities. A simple cut on 0.5 would generally result in a cluster sequence composed mostly by bright stars, without respecting the actual photometric density of the purported cluster (given by the cluster region vs field region photometric density differences). Hence, the selected stars within the cluster region should be not only those with large

membership probabilities or sharing a similar physical attribute (i.e., parallax). They should also be properly distributed in the photometric diagrams and as close as possible in number to the estimated number of members. As stated above this is of particular importance for clusters with few members, as the process to find their best fit parameters is driven by a handful of stars which makes the analysis much more delicate.

In the case of RUP 87 we selected stars that had both large membership values, and were similar in number to the estimated number of members for the cluster region. The 24 stars that remain in the adopted region along with the best fit found can be seen in Fig. 14. The code fits a somewhat old (3.1×10^9 yrs) synthetic cluster at a distance of ~ 3900 pc.

As seen in Fig. 15 the distance estimated through Gaia parallaxes for the same set of stars is ~ 6200 pc, which is more than 2000 pc away from the photometric estimate. This difference is too large to be consistent with a real cluster, even taking possible offsets into account. To see if this discrepancy could be solved as we did for vdBH 85 (see Sect. 6) we run the same analysis described there using Bailer-Jones distances. The resulting weighted average for the distance is 4680^{+620}_{-3090} pc. This distance is

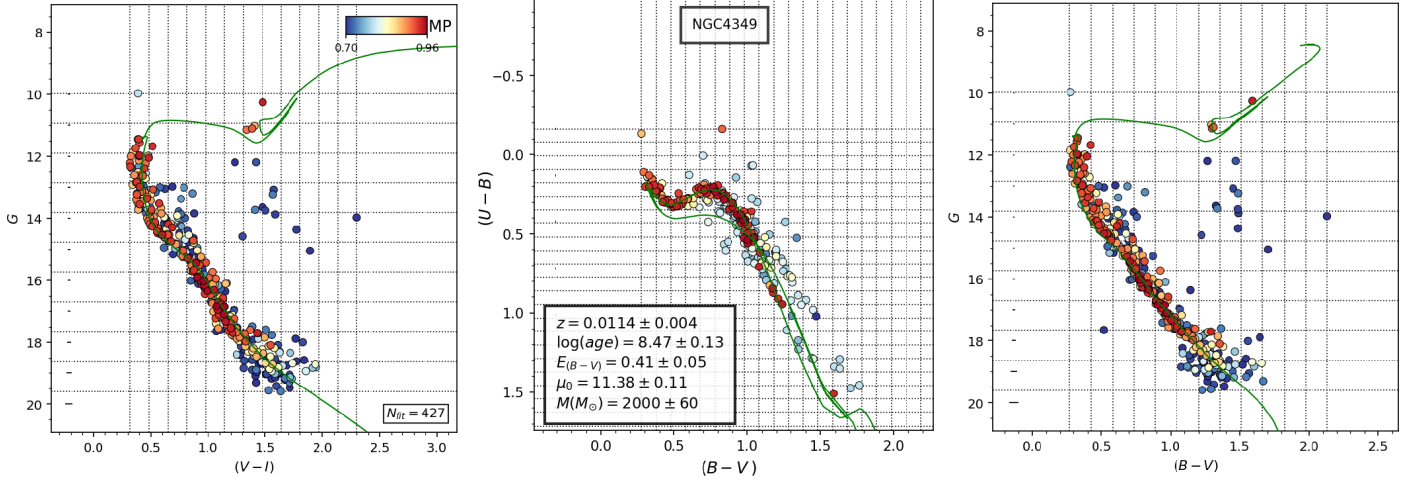


Fig. 10. Idem Fig. 6 for NGC 4349.

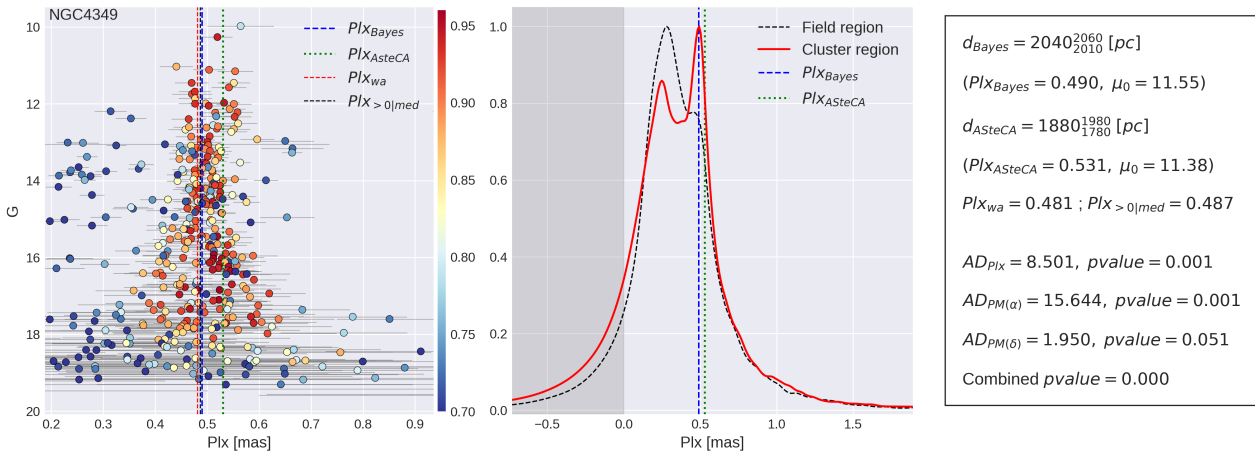


Fig. 11. Idem Fig. 7 for NGC 4349.

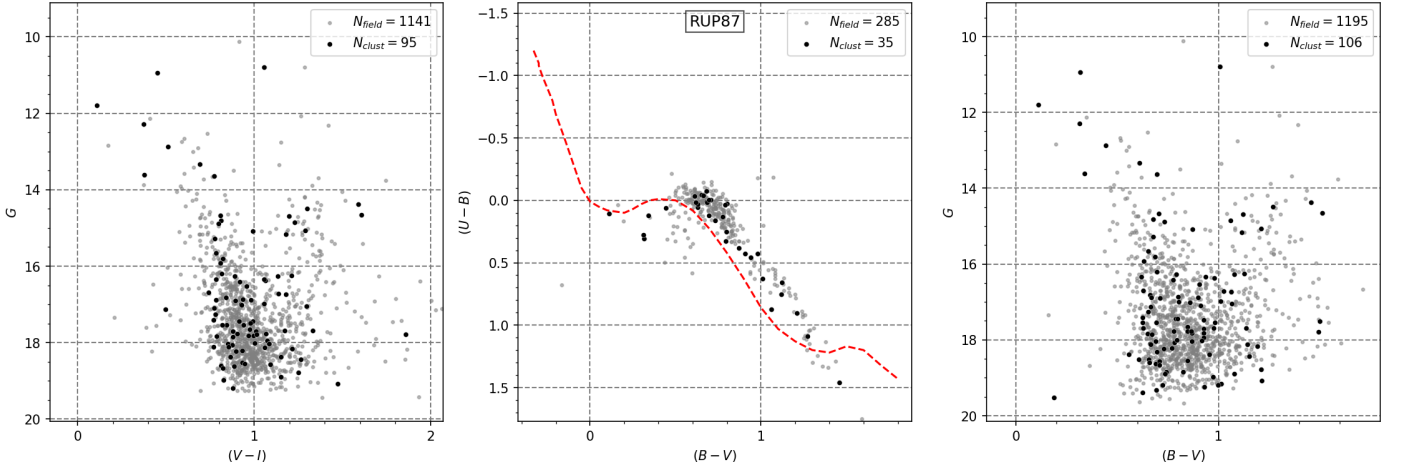


Fig. 12. Idem Fig. 4 for RUP 87.

almost 800 pc larger than the photometric estimate, and 1500 pc smaller than the Gaia parallax estimate. Such large differences are consistent with the fact that we are not analyzing an actual cluster.

The Anderson-Darling test values for Plx and proper motions do not confirm clear differences between the cluster region and the stellar background in terms of kinematics and distance.

The poverty of the photometric diagrams and the analysis of photometric distances versus parallax distances are all against the true existence of a cluster in the region RUP 87. In our interpretation this is not a real entity but a fluctuation of the star field.

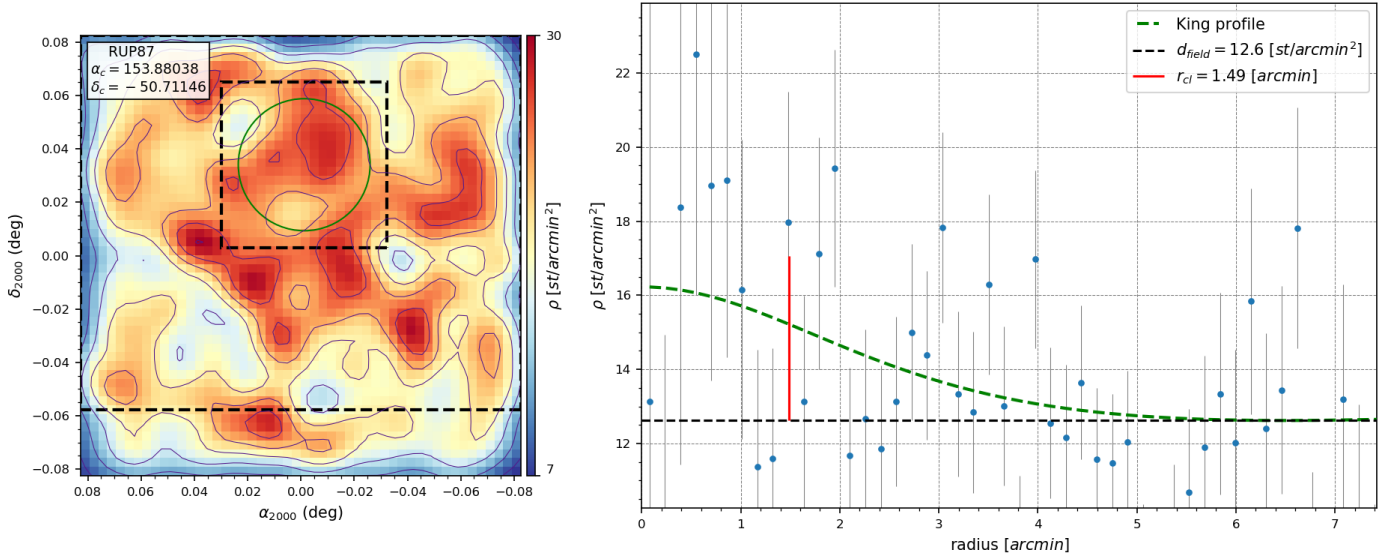


Fig. 13. Idem Fig. 5 for RUP 87.

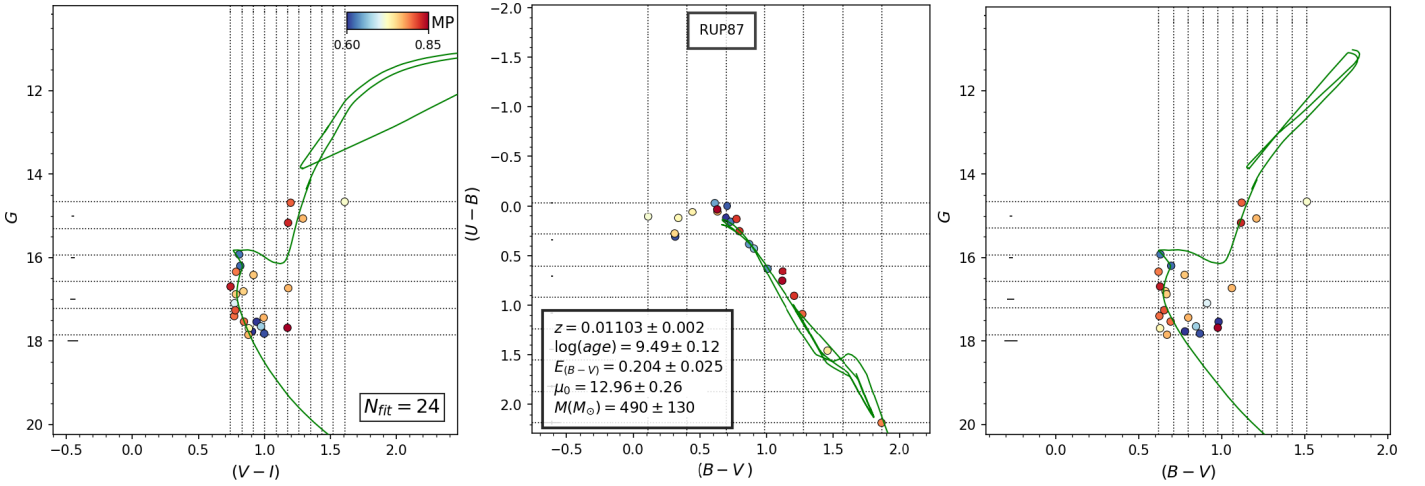


Fig. 14. Idem Fig. 6 for RUP 87.

6. Gaia parallax distances analysis

We shall close our analysis by taking a look at the matter of distances yielded by AStECA and those that can be obtained using parallaxes alone. Specifically, we cross-matched *Plx* data with our photometry, cluster by cluster, and processed them within a Bayesian framework (as explained in Sect 4.1). The intention is to visualize the change in estimated distances if no correction is applied to the parallaxes, and when current values taken from the literature are used.

In Fig. 16 we show the AStECA versus Bayesian (parallax) distances with no offset applied (left), and the Bayesian parallax for each cluster (as the inverse of the distance) versus its difference with the AStECA estimate (middle). It is evident from this figure that AStECA distances are systematically smaller than the ones coming from the computation of parallax alone. The mean of the AStECA minus parallax differences in distance is ~ -411 pc. The middle plot with the mean difference suggests that a correction of $+0.028$ mas should be applied to the Gaia DR2 parallax values. The cluster vdBH85 is omitted from Fig. 16 (left and middle plots) because the Bayesian framework applied

on its parallax data yielded results that were clearly wrong. This can be seen in Fig. 7 where the parallax distance estimated is above 8 kpc, versus the photometric distance obtained by AStECA of ~ 4.6 kpc. Out of the ten clusters in our list of confirmed plus dubious clusters, vdBH85 is the oldest one. This means that its main sequence is quite short and composed mostly of low mass stars. More than 60% of its 146 estimated members have $G > 18$ mag, and almost 75% have Gaia DR2 parallax values with uncertainties larger than 0.1 mas (with a mean parallax uncertainty of ~ 0.16 mas). Because of this, the Bayesian method fails to estimate a reasonable distance for this cluster, and we omit it from this analysis.

A number of recent articles have found that there is an offset present in Gaia's parallax data, covering a range of approximately $+0.05$ mas. We selected three of these articles that fully cover this range, to compare with our results obtained with no bias corrections: Lindegren et al. (2018), Schönrich et al. (2019), and Xu et al. (2019). In Lindegren et al. the authors processed the parallax of hundreds of thousands of quasars deriving a median difference with Gaia data of $+0.029$ mas. The work by Schönrich et al. analyzed the radial velocities subset of Gaia DR2 with their

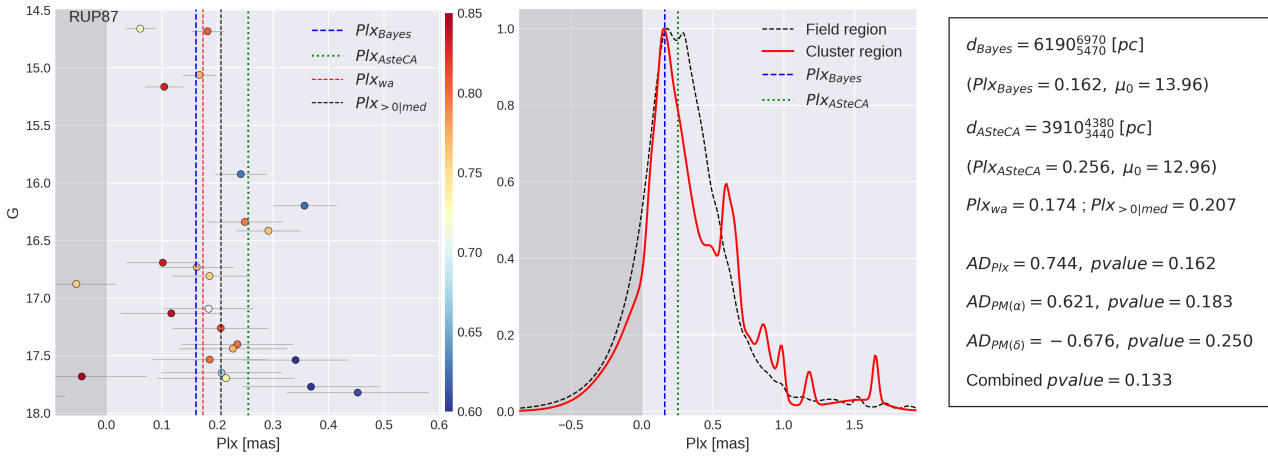


Fig. 15. Idem Fig. 7 for RUP 87.

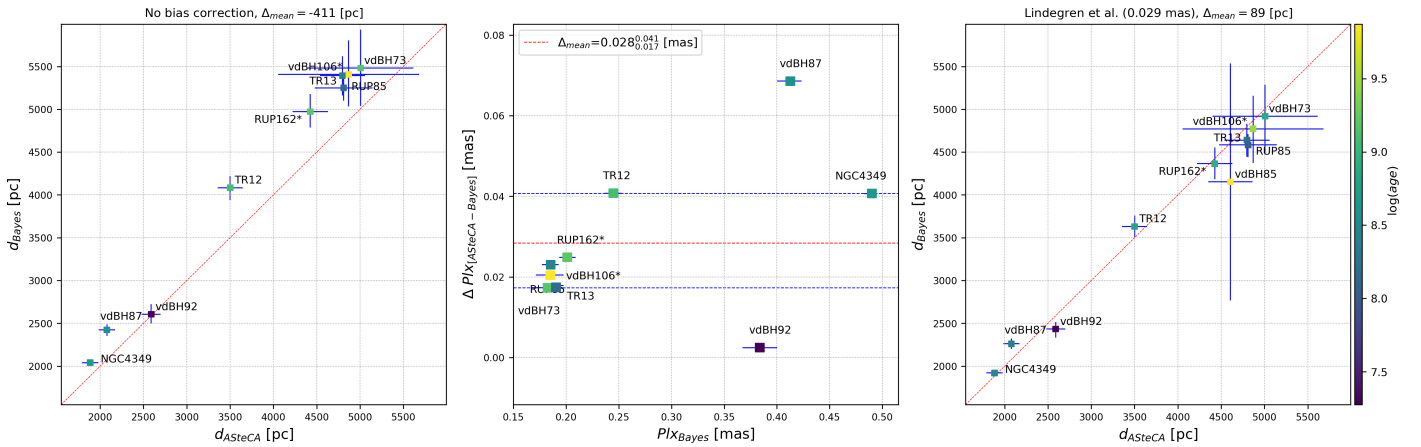


Fig. 16. Left: ASteCA (photometric) vs Bayesian (parallax) distances for the clusters listed in Table 4, confirmed to be real clusters. No bias correction applied to parallax data. Colorbar to the right indicates $\log(\text{age})$ values. Center: offset (ASteCA - Bayes) for distances expressed as parallax in milliarcseconds. Right: same as left plot, with bias corrections from Lindegren et al. (+0.029 mas). The cluster vdBH85 is included here with its distance value estimated from the list of Bailer-Jones et al. (2018) individual distances.

own Bayesian inference tool, and estimated a required +0.054 mas offset in the parallax data from Gaia DR2. Finally, Xu et al. used ~ 100 stars with Very Long Baseline Interferometry astrometry, and found an offset of +0.075 mas with Gaia DR2 parallaxes. If we add to the parallax data the offsets given in Lindegren et al., Schönrich et al., and Xu et al. (+0.029, +0.054, +0.075 mas, respectively) the agreement between ASteCA and parallax distances improves at first and rapidly worsens. The mean differences between photometric distances and parallax distances are of ~ 0.09 kpc, ~ 0.39 kpc, and ~ 0.62 kpc, using the Lindegren et al., Schönrich et al., and Xu et al. corrections, respectively.

In the case of vdBH85, being unable to apply the Bayesian method described in Sect. 4.1 (as explained above), we turn to the individual distance values obtained in Bailer-Jones et al. (2018). In this article the authors use Bayesian inference to estimate distances (in parsec) to more than 1 billion stars using the Gaia DR2 parallax values, applying the Lindegren et al. correction.³⁰ We cross match our list of members for vdBH85 and approximate the distance to the cluster as their average distance, weighted by the assigned uncertainties. Although this is a rather low quality estimate due to the large uncertainties in the indi-

vidual distances, as seen by the large error bars in Fig. 16 (right plot), it is still close to the photometric distance estimate. If we omit vdBH85 entirely, the Lindegren et al. mean difference improves to ~ 0.05 kpc.

Our analysis thus points to a required bias correction to Gaia parallaxes of +0.028 mas, which is very close to the one proposed by Lindegren et al.

In Sect 3.1 we saw that our $(B - V)$ color has a small offset of ~ 0.0153 mag when compared to the (transformed) Gaia photometry. ASteCA employs the extinction law by Cardelli et al. (1989, CCC law) with the O'Donnell (1994) correction for the near UV, to transform $E(B - V)$ values into absorptions for any filter. In our case, we used Gaia's G filter whose absorption A_G is related to $E(B - V)$ as: $A_G = c_0 A_V = c_0 3.1 E(B - V)$, where $c_0 \approx 0.829$ according to the CCC law. Hence the absorption A'_G , i.e., corrected by the offset in $(B - V)$, can be written as: $A'_G = 0.039 + A_G$. Given the range of distance moduli in this work ($\sim 11 - 14$ mag), the impact of this correction on the distance in parsec goes from ~ 30 to 100 pc. If we apply this $(B - V)$ offset to our photometric distances and re-run the analysis, the +0.028 mas bias in Gaia parallaxes that we found initially is reduced to +0.023 mas. This is a smaller value, but still very close to the Lindegren et al. bias.

³⁰ This should not be confused with the Bayesian inference method described in Sect. 4.1. These are two very different processes.

Certainly, analysis of a more extended sample of clusters is needed for arriving to conclusive results and establish the detailed relation between distances from photometry and DR2 parallaxes. The results of the exercise presented in this section are included in the last 4 columns of Table 4.

7. Discussion of results and concluding remarks

We have analyzed the fields of sixteen catalogued open clusters located in a Galaxy sector covering from 270° to 300° approximately in galactic longitude, and mostly close to the formal galactic plane at $b = 0^\circ$. The cluster parameter estimations presented in this article are based on precise *UBVI* photometry analyzed in a automatic way by our code *ASteCA*. The code searches for a meaningful stellar overdensity assigning membership probabilities by comparison with the surrounding stellar field. The next step establishes the physical properties of the best synthetic cluster that fits the distribution of cluster members in the CMDs and the CCD. Through this process reddening, distance, age, mass, and metallicity are given. The most relevant inconvenience we have found with the present cluster sample resides in the fact that some of them are extremely faint, which becomes evident in a visual inspection of their overall CCDs and CMDs. Things get more difficult because the $(U - B)$ index has been mostly available only for the bright and blue stars which reduced considerably the data analysis space. Despite this, we were able to keep the reddening solutions under control and obtain reliable distances estimations for those objects found true clusters by our code. This way, we can safely reject RUP 87, vdBH91, RUP 88, Lynga 15, Loden 565 and NGC 4230 that are most probably random stellar fluctuations. The results for true and probable open clusters are shown in Table 4 in self-explanatory format.

If we average the metallicity for each cluster, shown in the second column of Table 4, the metal content is $z = 0.0136 \pm 0.006$. The result is well in agreement with the assumption that the typical Milky Way open cluster has solar metallicity ($z = 0.0152$, Bressan et al. 2012).

Of the remaining ten objects, two are probable clusters with distances in the 4-5 kpc range. Ages of clusters sweep from a few million years to almost 8 billion years in the case of vdBH 85. The vdBH 106 cluster is one of the oldest but it is just a probable open cluster, so its age should be taken with reservation. Two other objects, TR 13 and vdBH 92, are young with ages close to and under 100 million years respectively, while the rest are all less than 1 billion years old.

A final remark concerns the spatial distribution of the eight real clusters plus two probable ones indicated in Table 4. These objects are plotted in Fig 17 in the X-Y (upper) and X-Z (lower) planes of the Milky Way -following the usual signs convention- where the Sun is placed at (0, 0). Superposed in this figure is the outline of the Carina Arm taken from Vallée (2005). All these objects are plotted with open circles except the two youngest, which are shown with red squares. TR 13, one of the youngest (0.1 Gyr) and farthest (4.8 kpc) objects, is located along the external side of the Carina arm but appears well below the Galaxy plane at about -0.2 kpc, thus accompanying the warp of this arm already mentioned by, among others, Cersosimo et al. (2009). The other young cluster, vdBH 92 (0.02 Gyr), is relatively far from the Carina Nebula nucleus in an intermediate zone between that region and the Sun but still seen close to the northwest side of the Carina Nebula at a distance that is comprised within the estimated maximum and minimum distance for Carina. vdBH 106 (3 Gyr) and vdBH 85 (7.5 Gyr) are the oldest objects found in

our search and are, in turn, placed well above the formal galactic equator (0.3-0.4 kpc). TR 12 (0.7 Gyr) is another quite old object placed below the plane (-0.2 kpc) together with RUP 162 (1 Gyr). The rest of the clusters are of middle age and relatively close to the Galaxy plane.

With respect to photometric versus parallax distances, we can conclude that by adding $\sim +0.028$ mas to the cluster computed parallaxes from Gaia DR2 the level of agreement with the photometric distances improves considerably. Taking into account the small offset found for the $(B - V)$ color, this value drops to $+0.023$ mas, which is only 0.006 mas smaller than the Lindegren et al. $+0.029$ mas correction. This reinforces the evidence pointing to this offset over larger values proposed in the literature. Our cluster sample is not large enough to permit us drawing stronger conclusions on this matter, particularly regarding the possible dependence of the correction with distance.

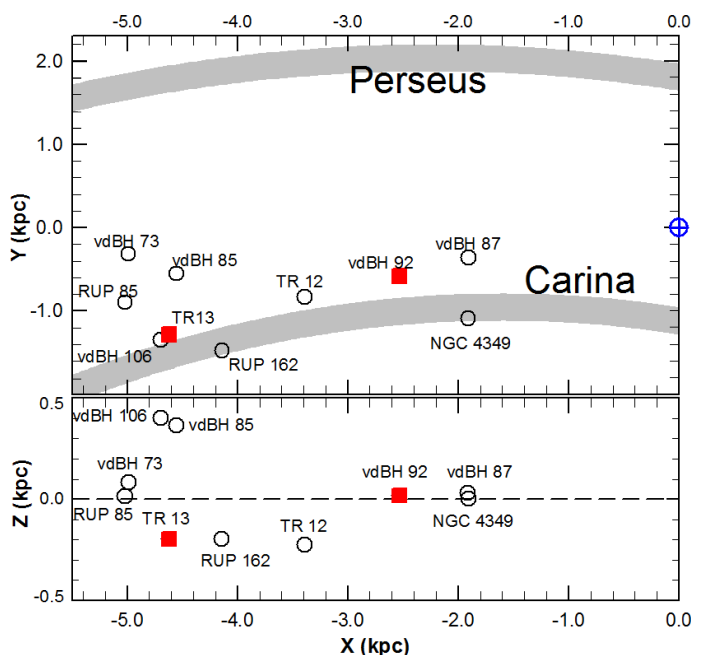


Fig. 17. The X-Y (upper panel) and X-Z (lower plane) projection of the true and probable clusters in our sample (open circles). The red squares enclose the youngest clusters in our list (see Table 4). In the upper panel the thick grey lines shows the trace of the Perseus and Carina arms according to Vallée (2005). The position of the Sun is shown by a blue circle with a cross inside. Dashed line in the lower panel depicts the galactic equator.

Acknowledgements. G.P., E.E.G., M.S.P. and R.A.V. acknowledge the financial support from CONICET (PIP317) and the UNLP. AM acknowledges the support from the Portuguese Strategic Programme UID/FIS/00099/2019 for CEN-TRA. The authors are very much indebted with the anonymous referee for the helpful comments and suggestions that contributed to greatly improving the manuscript. This research was made possible through the use of the AAVSO Photometric All-Sky Survey (APASS), funded by the Robert Martin Ayers Sciences Fund and NSF AST-1412587. This research has made use of the WEBDA database, operated at the Department of Theoretical Physics and Astrophysics of the Masaryk University. This research has made use of the VizieR catalogue access tool, operated at CDS, Strasbourg, France (Ochsenbein et al. 2000). This research has made use of “Aladin sky atlas” developed at CDS, Strasbourg Observatory, France (Bonnarel et al. 2000; Boch & Fernique 2014). This research has made use of NASA’s Astrophysics Data System. This research made use of the Python language v3.7.3 (van Rossum 1995) and the following packages: NumPy³¹ (Van Der Walt et al. 2011); SciPy³² (Jones et al. 2001); Astropy³³, a

³¹ <http://www.numpy.org/>

³² <http://www.scipy.org/>

³³ <http://www.astropy.org/>

Table 4. The symbol “*” indicates probable clusters. The $d_{noofset}$ values are those obtained using the Bayesian method and no bias correction applied on the Gaia DR2 parallax data. The remaining distances were obtained applying the indicated offsets to the parallax values.

Cluster	z	Age (10^9 yr)	$E(B - V)$ mag	Mass ($10^3 M_{\odot}$)	$d_{AS\&CA}$ (kpc)	$d_{noofset}$ (kpc)	$d_{Lindegren}$ (kpc)	$d_{Schönrich}$ (kpc)	d_{Xu} (kpc)
vdBH 73	0.019±0.004	0.78±0.09	1.06±0.04	2.6±0.9	5.01 ± 0.61	5.48 ± 0.44	4.92 ± 0.41	4.46 ± 0.31	4.05 ± 0.33
RUP 85	0.021±0.003	0.18±0.03	1.06±0.03	2.6±0.5	4.80 ± 0.26	5.39 ± 0.23	4.64 ± 0.19	4.16 ± 0.15	3.83 ± 0.14
vdBH 85	0.014±0.002	7.50±0.80	0.30±0.03	2.2±0.5	4.61 ± 0.26	—	4.15 ± 1.38	—	—
vdBH 87	0.025±0.002	0.25±0.08	0.55±0.04	1.4±0.2	2.08 ± 0.09	2.42 ± 0.07	2.26 ± 0.06	2.13 ± 0.05	2.05 ± 0.05
TR 12	0.009±0.002	0.70±0.10	0.31±0.03	0.7±0.1	3.50 ± 0.15	4.08 ± 0.14	3.63 ± 0.13	3.31 ± 0.10	3.11 ± 0.09
vdBH 92	0.009±0.004	0.02±0.01	0.65±0.03	0.4±0.1	2.59 ± 0.11	2.61 ± 0.11	2.43 ± 0.09	2.28 ± 0.07	2.17 ± 0.07
TR 13	0.007±0.004	0.11±0.02	0.56±0.02	0.7±0.2	4.81 ± 0.33	5.25 ± 0.16	4.58 ± 0.14	4.10 ± 0.11	3.75 ± 0.09
vdBH 106*	0.012±0.003	3.00±0.80	0.30±0.04	0.5±0.2	4.87 ± 0.81	5.41 ± 0.39	4.77 ± 0.39	4.31 ± 0.33	4.06 ± 0.30
RUP 162*	0.009±0.002	0.80±0.20	0.54±0.03	1.2±0.2	4.43 ± 0.20	4.97 ± 0.20	4.37 ± 0.18	3.94 ± 0.15	3.66 ± 0.13
NGC 4349	0.011±0.004	0.29±0.09	0.41±0.05	2.0±0.1	1.88 ± 0.05	2.04 ± 0.03	1.92 ± 0.02	1.83 ± 0.02	1.76 ± 0.01

community-developed core Python package for Astronomy (Astropy Collaboration et al. 2013); matplotlib³⁴ (Hunter et al. 2007); emcee³⁵ (Foreman-Mackey et al. 2013); corner.py³⁶ (Foreman-Mackey 2016).

References

- Aller, L. H., Appenzeller, I., Baschek, B., et al., eds. 1982, Landolt-Börnstein: Numerical Data and Functional Relationships in Science and Technology - New Series "Gruppe/Group 6 Astronomy and Astrophysics" Volume 2 Schaifers/Voigt: Astronomy and Astrophysics / Astronomie und Astrophysik "Stars and Star Clusters / Sterne und Sternhaufen
- Astropy Collaboration, Robitaille, T. P., Tollerud, E. J., et al. 2013, A&A, 558, A33
- Avedisova, V. S. 2002, Astronomy Reports, 46, 193
- Bailer-Jones, C. A. L., Rybizki, J., Founesneau, M., Mantelet, G., & Andrae, R. 2018, AJ, 156, 58
- Boch, T. & Fernique, P. 2014, in Astronomical Society of the Pacific Conference Series, Vol. 485, Astronomical Data Analysis Software and Systems XXIII, ed. N. Manset & P. Forshay, 277
- Bonnarel, F., Fernique, P., Bienaymé, O., et al. 2000, AAPS, 143, 33
- Bossini, D., Vallenari, A., Bragaglia, A., et al. 2019, A&A, 623, A108
- Bressan, A., Marigo, P., Girardi, L., et al. 2012, MNRAS, 427, 127
- Cantat-Gaudin, T., Jordi, C., Vallenari, A., et al. 2018, A&A, 618, A93
- Cardelli, J. A., Clayton, G. C., & Mathis, J. S. 1989, ApJ, 345, 245
- Carraro, G., Costa, E., & Ahumada, J. A. 2010, AJ, 140, 954
- Carraro, G., Vázquez, R. A., Moitinho, A., & Baume, G. 2005, ApJ, 630, L153
- Cersosimo, J. C., Mader, S., Figueroa, N. S., et al. 2009, ApJ, 699, 469
- Charbonneau, P. 1995, The Astrophysical Journal Supplement Series, 101, 309
- Dias, W. S., Alessi, B. S., Moitinho, A., & Lépine, J. R. D. 2002, A&A, 389, 871
- Dolphin, A. E. 2002, Monthly Notices of the Royal Astronomical Society, 332, 91
- Efron, B. & Tibshirani, R. 1986, Statist. Sci., 1, 54
- Foreman-Mackey, D. 2016, The Journal of Open Source Software, 1, 24
- Foreman-Mackey, D., Hogg, D. W., Lang, D., & Goodman, J. 2013, PASP, 125, 306
- Gaia Collaboration, Brown, A. G. A., Vallenari, A., et al. 2018, ArXiv e-prints [arXiv:1804.09365]
- Hunter, J. D. et al. 2007, Computing in science and engineering, 9, 90
- Janes, K. & Adler, D. 1982, The Astrophysical Journal Supplement Series, 49, 425
- Jones, E., Oliphant, T., Peterson, P., et al. 2001, SciPy: Open source scientific tools for Python, [Online; accessed 2016-06-21]
- Kharchenko, N. V., Piskunov, A. E., Röser, S., Schilbach, E., & Scholz, R.-D. 2005, A&A, 438, 1163
- King, I. 1962, AJ, 67, 471
- Kroupa, P. 2002, Science, 295, 82
- Landolt, A. U. 1992, AJ, 104, 340
- Lindegren, L., Hernández, J., Bombrun, A., et al. 2018, A&A, 616, A2
- Lohmann, W. 1961, Astronomische Nachrichten, 286, 105
- Luri, X., Brown, A. G. A., Sarro, L. M., et al. 2018, ArXiv e-prints [arXiv:1804.09376]
- Magrini, L., Stanghellini, L., Corbelli, E., Galli, D., & Villaver, E. 2009, VizieR Online Data Catalog, J/A+A/512/A63
- Moitinho, A. 2010, in IAU Symposium, Vol. 266, Star Clusters: Basic Galactic Building Blocks Throughout Time and Space, ed. R. de Grijs & J. R. D. Lépine, 106–116
- Moitinho, A., Vázquez, R. A., Carraro, G., et al. 2006, MNRAS, 368, L77
- Monteiro, H. & Dias, W. S. 2019, MNRAS, 487, 2385
- Ochsenbein, F., Bauer, P., & Marcout, J. 2000, A&AS, 143, 23
- O'Donnell, J. E. 1994, ApJ, 422, 158
- Perren, G. I., Piatti, A. E., & Vázquez, R. A. 2017, A&A, 602, A89
- Perren, G. I., Vázquez, R. A., & Piatti, A. E. 2015, A&A, 576, A6
- Ruprecht, J., Balazs, B., & White, R. E. 1996, VizieR Online Data Catalog, VII/101A
- Schlafly, E. F. & Finkbeiner, D. P. 2011, ApJ, 737, 103
- Schönrich, R., McMillan, P., & Eyer, L. 2019, MNRAS, 487, 3568
- Sollima, A., Carballo-Bello, J. A., Beccari, G., et al. 2010, MNRAS, 401, 577
- Soubiran, C., Cantat-Gaudin, T., Romero-Gómez, M., et al. 2018, A&A, 619, A155
- Späth, H. 2004, Mathematical Communications, 9, 27
- Stetson, P. B. 1987, PASP, 99, 191
- Stetson, P. B., Davis, L. E., & Crabtree, D. R. 1990, in Astronomical Society of the Pacific Conference Series, Vol. 8, CCDs in astronomy, ed. G. H. Jacoby, 289–304
- Tadross, A. L. 2011, Journal of Korean Astronomical Society, 44, 1
- Trumpler, R. J. 1930, Lick Observatory Bulletin, 420, 154
- Vallée, J. P. 2005, AJ, 130, 569
- van den Bergh, S. & Hagen, G. L. 1975, AJ, 80, 11
- Van Der Walt, S., Colbert, S. C., & Varoquaux, G. 2011, Computing in Science & Engineering, 13, 22
- van Rossum, G. 1995, Python tutorial, Report CS-R9526, pub-CWI, pub-CWI:adr
- Vázquez, R. A., May, J., Carraro, G., et al. 2008, ApJ, 672, 930
- Xu, S., Zhang, B., Reid, M. J., Zheng, X., & Wang, G. 2019, arXiv e-prints, arXiv:1903.04105
- Yen, S. X., Reffert, S., Schilbach, E., et al. 2018, ArXiv e-prints [arXiv:1802.04234]

³⁴ <http://matplotlib.org/>

³⁵ <http://emcee.readthedocs.io>

³⁶ <https://corner.readthedocs.io>

The thirteen clusters in this Appendix are ordered according to their longitude, as shown in Table 1. The remaining three analyzed clusters were presented in Sect. 5.

Appendix A: van den Bergh-Hagen 73

The cluster vdBH 73 is placed in almost the center of the Vela constellation well at the northeast border of the Carina Constellation. The visual chart of the region in Fig. 3 shows a small and compact grouping of stars at the very center of the frame surrounded by a dense stellar field. The inspection of the CCD and CMDs for all the stars observed in the targeted region in Fig. A.1 gives no clear hints about the presence of a cluster there, likely due to the effect of field star contamination. There are in the CMDs of Fig. A.1 few stars above $G = 15$ mag and at larger magnitudes the CMDs strongly widen. The reddening in the CCD, right panel in Fig. A.1, is quite strong and displaces the bulk of stars entirely toward the red side. A few blue stars with negative $(U - B)$ values appear strongly affected by variable reddening.

The left panel in Fig. A.2 shows a pronounced star overdensity of 2.2 arcmin radius, coincident with the location expected for vdBH 73. This overdensity appears immersed in a region of large field star contamination. As seen in the RDP to the right, the density peak is about four times above the mean for the field.

The CMDs in Fig. A.3, left and right panels, put in evidence a cluster main sequence subtending 1.5 magnitudes and a faint giant branch with stars up to $G = 15$ mag. The $(B - V)$ vs $(V - I)$ CCD is shown in the middle panel instead of the $(B - V)$ vs $(U - B)$ diagram because the latter did not contain enough stars to be of use in the extinction estimation process. Although the CMDs after the removal of interlopers look somewhat noisy, those stars with membership probabilities above ~ 0.7 clearly trace the sequence of an evolved cluster.

The best fitting of a synthetic cluster yields the following results:

- The cluster is immersed in a region of moderate absorption since the mean of reddening comes to be $E(B - V) = 1.06$, a value compatible with the ones provided by Schlafly & Finkbeiner (2011) (hereafter S&F2011) who found a maximum $E(B - V)$ of about 1.2 mag towards vdBH 73.
- The absorption-free distance modulus turns out to be 13.50 ± 0.26 mag placing this object at 5.01 ± 0.61 kpc from the Sun.

From the photometric point of view the existence of a well outlined cluster main sequence and the high probability memberships of the stars seen in it confirm the real entity of vdBH 73.

The usage of parallax data from Gaia shows a good agreement in distance reaching up 5.48 ± 0.44 kpc in the sense that Gaia parallaxes place the cluster farther than photometry does. This difference improves when offset is applied to the parallax data, as shown in Sect. 7. The Anderson-Darling test applied to parallax and proper motion data demonstrates that the null hypothesis can indeed be rejected with a combined p -value of 0.0, pointing to a real cluster present in this region.

We conclude from our analysis that van den Bergh-Hagen 73 is an intermediate aged cluster around $0.78 \pm 0.09 \times 10^9$ years old.

Appendix B: Ruprecht 85

Ruprecht 85 belongs to the south side of the Vela Constellation close to the border of the Carina region. This cluster appears in Fig. 3 as a slight increment in the stellar field towards the north part in the respective frame. The overall stars photometric diagrams as shown in Fig. B.1 do not show the presence of any cluster sequence but a vertical strip of stars emerging from a poorly populated stellar field above $G = 14$ mag defined by disk stars.

The structural analysis performed by ASteCA yields a clean overdensity at the location of this object that appears subtending an almost circular area with a radius between 2-3 arcmins, Fig. B.2 left panel. As shown in Fig. B.2 right panel, the RDP is well developed and with a star density five times above the background level. The photometric diagrams, CCD and CMDs of stars with membership probabilities above 0.48 and up to 1.0 shown in Fig. B.3 depict a rather noisy main sequence sweeping 3.5 magnitudes. Combining structural evidences with evidences coming from the photometric diagrams we conclude that RUP 85 is a real entity. As for the cluster parameters of the best synthetic cluster fitting the observations it is found that:

- As was the case with vdBH 73, RUP 85 is also placed in a region of moderate color excess. The cluster has $E(B - V) = 1.06$ also entirely in line with a maximum $E(B - V)$ of 2 mag according to S&F2011.
- The free absorption distance modulus is 13.40 ± 0.12 mag corresponding to a distance $d = 4.80 \pm 0.26$ kpc.

The results from the Anderson-Darling test in Fig. B.4 applied to Plx , $PM(\alpha)$ and $PM(\delta)$ indicate clearly that the cluster region and the surrounding background population come from quite different star populations. Therefore, the null hypothesis can be rejected.

We conclude that RUP 85 is a real open cluster around $0.18 \pm 0.03 \times 10^9$ years old.

Appendix C: van den Bergh-Hagen 87

Like RUP 85, vdBH 87 is seen toward the south of Vela Constellation close to the border with Carina. A weak grouping of stars placed towards the north of the frame is seen in Fig. 3. In turn, the CMDs in Fig. C.1 seem to reflect a typical star disk sequence up to $G = 15$ mag approximately with an amorphous distribution at the bright end. The CCD is, on the other side, rather poor.

A stellar overdensity reaching ~ 7 times the field star density is seen in Fig. C.2. The spatial structure of this overdensity suggests an elongation in right ascension and a RDP characterized by a very narrow density peak followed by a star coronal distribution at about 1.5 arcmins from the center. The clean CMDs in Fig. C.3 leave no doubt as for the nature of vdBH 87 since inside this overdensity a robust and narrow cluster main sequence is evident. Its sequence extends for more than 5 mag in the CMDs, including stars with very low membership probabilities well detached from the sequence, in the range from 0.0 to 0.98. The parameters of the synthetic cluster that best fits the real star distributions are:

- The color excess is $E(B - V) = 0.56$ indicating thus a moderate absorption in the cluster direction. In turn, this color ex-

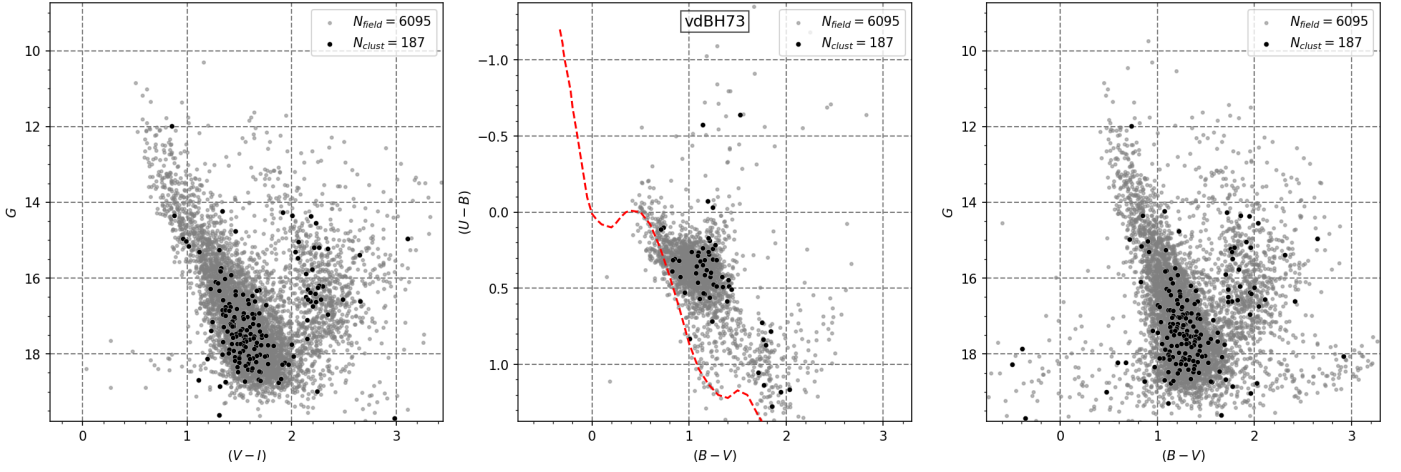


Fig. A.1. Idem Fig. 4 for vdBH 73.

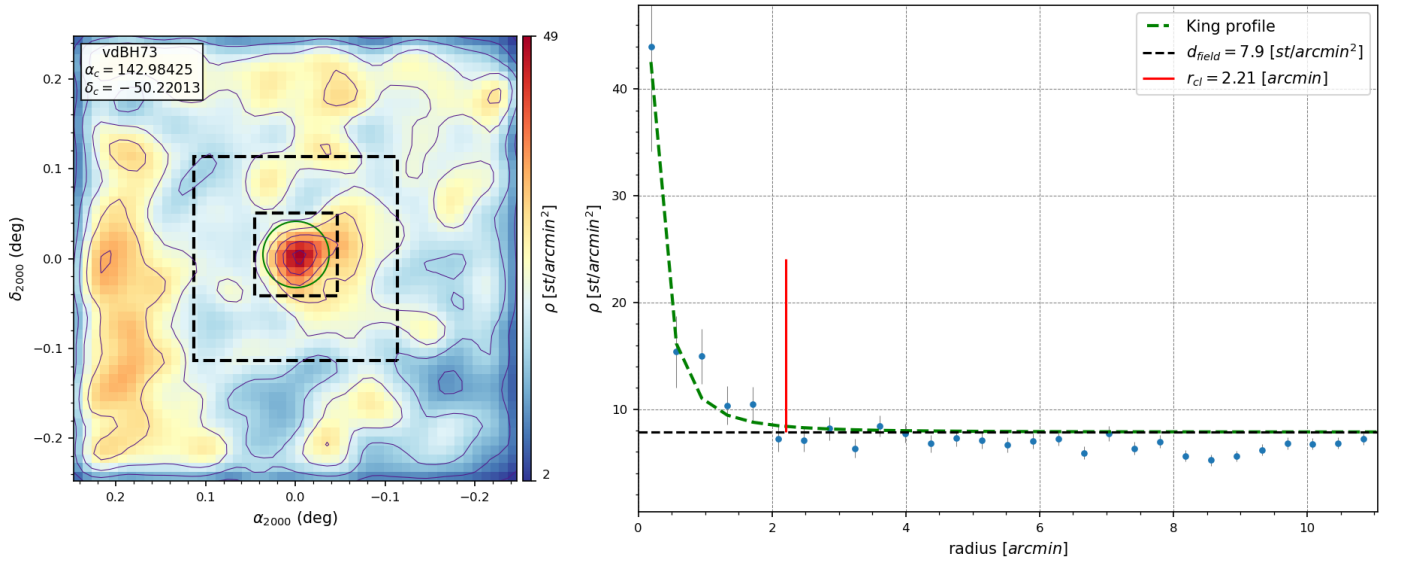


Fig. A.2. Idem Fig. 5 for vdBH 73.

cess value is below the maximum reddening $E(B - V) = 2.9$ computed in the region for S&F2011.

- b) The corrected distance modulus is 11.59 ± 0.09 mag implying a distance of $d = 2.08 \pm 0.09$ kpc. The cluster is not far from the Sun and this closeness explains the moderate color excess found.

The results of the application of the Anderson-Darling test in Fig. C.4 are coincident with what AStECa have found. This is that cluster and field regions are quite different not only from the photometric perspective but also from a kinematic view.

In conclusion vdBH 87 is a real open cluster $0.25 \pm 0.08 \times 10^9$ years old.

Appendix D: van den Bergh-Hagen 92

Placed south of Vela, near the eastern border with Carina, vdBH 92 is a relevant handful of bright stars as seen in the V image of Fig. 3. The CMDs and CCD for all stars in the region, as shown in Fig. D.1, depict a narrow star sequence with some scatter at their respective bright ends. Particularly the CCD shows, not far from the intrinsic line, a group of F - and G -type stars and

another group of stars below the intrinsic line that could be B - and A - type stars displaced by the reddening effect.

The AStECa analysis in Fig. D.2 revealed the presence of a well isolated star overdensity rising above the field stars density of about 6 stars per square arcmin. We identify this overdensity with vdBH 92. Notwithstanding the noisy RDP the limits of the overdensity can be well established. As indicated in Fig. D.3 few stars have been found inside the cluster limits with mostly large membership values. Despite the low number of members, a 7 magnitude extended cluster main sequence can be seen. The comparison with synthetic clusters made by AStECa yields:

- a) the best fitting of a synthetic cluster to the clean data in Fig. D.3 indicates a color excess of $E(B - V) = 0.65$. Since the maximum color excess provided by S&F2011 is 2.34 for this zone we conclude that most of the absorption is produced behind the position of vdBH 92. This object is therefore placed in front of a strong absorption region.
- b) The absorption free distance modulus becomes 12.07 ± 0.09 mag, which places vdBH 92 at a distance of $d = 2.59 \pm 0.11$ kpc.

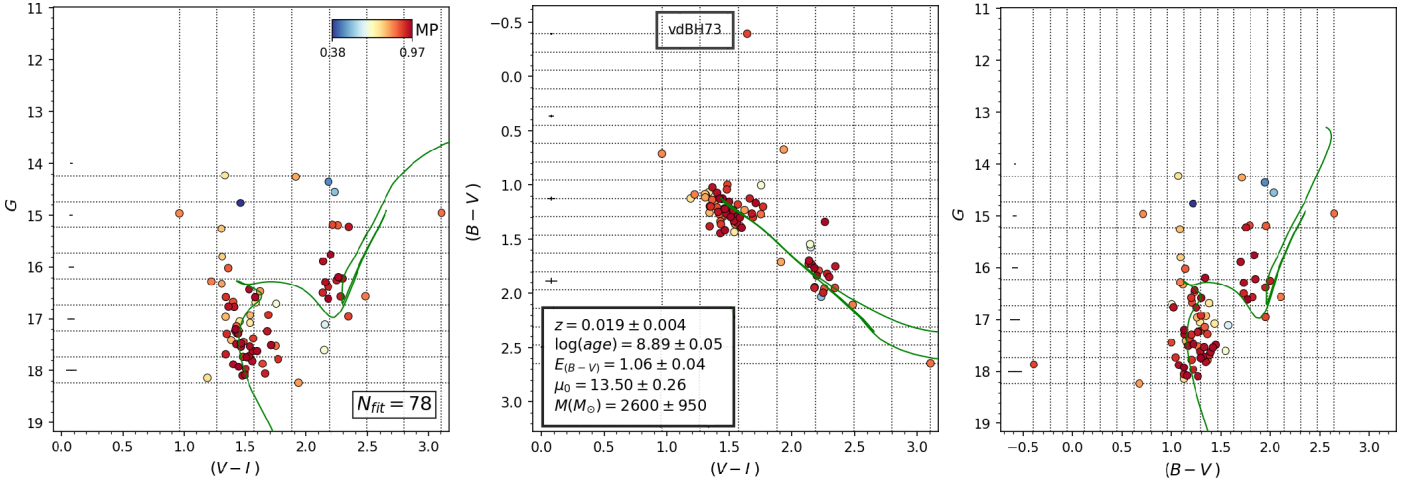


Fig. A.3. Idem Fig. 6 for vdBH 73 with the $(B - V)$ vs $(V - I)$ diagram instead of the $(B - V)$ vs $(U - B)$ diagram.

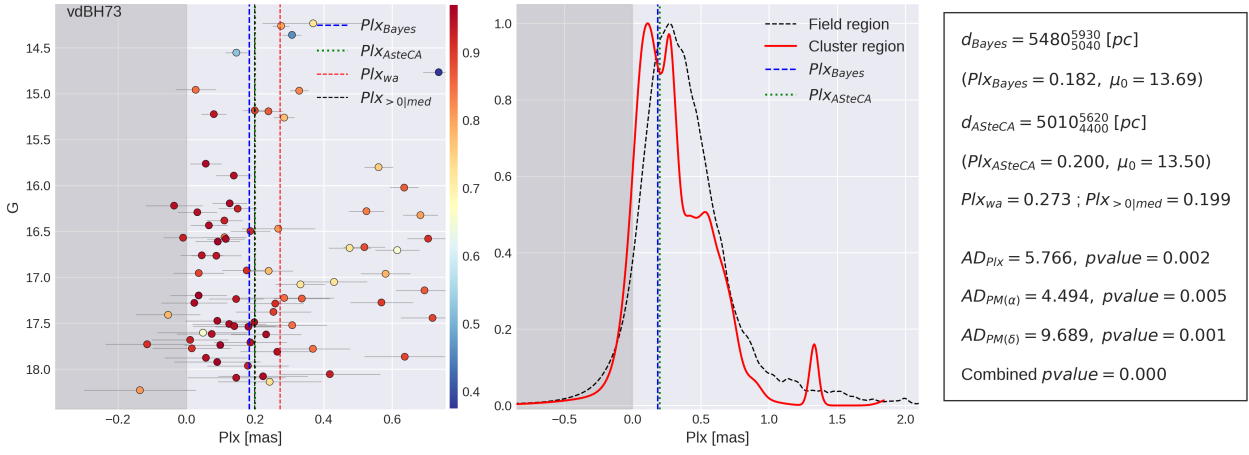


Fig. A.4. Idem Fig. 7 for vdBH 73.

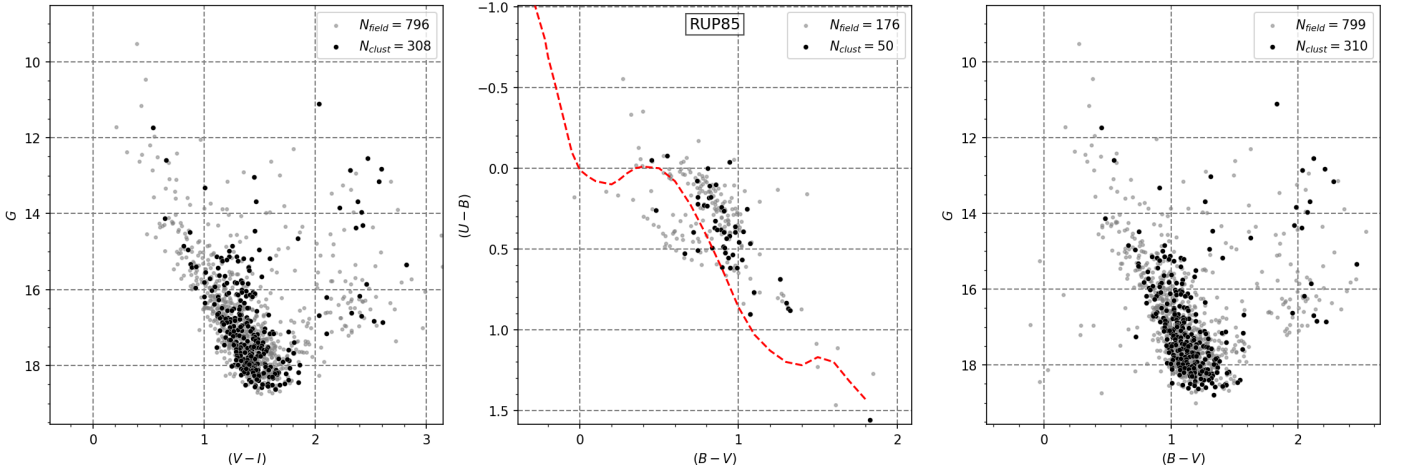


Fig. B.1. Idem Fig. 4 for RUP 85.

By applying the Anderson-Darling test it is noticed that the parallax distributions for stars inside and outside the cluster boundaries are not sufficiently different from each other to reach the 5% critical value, as indicated in the right panel of Fig. D.4. However, proper motions are quite different in both regions. We combine this last finding with the presence of a well defined overdensity that, in turn, shows a reasonable and extended

cluster main sequence to conclude that both samples come from different populations.

These results together confirm the true nature of vdBH 92. This is a young cluster $0.02 \pm 0.01 \times 10^9$ years old, the youngest true cluster in our sample.

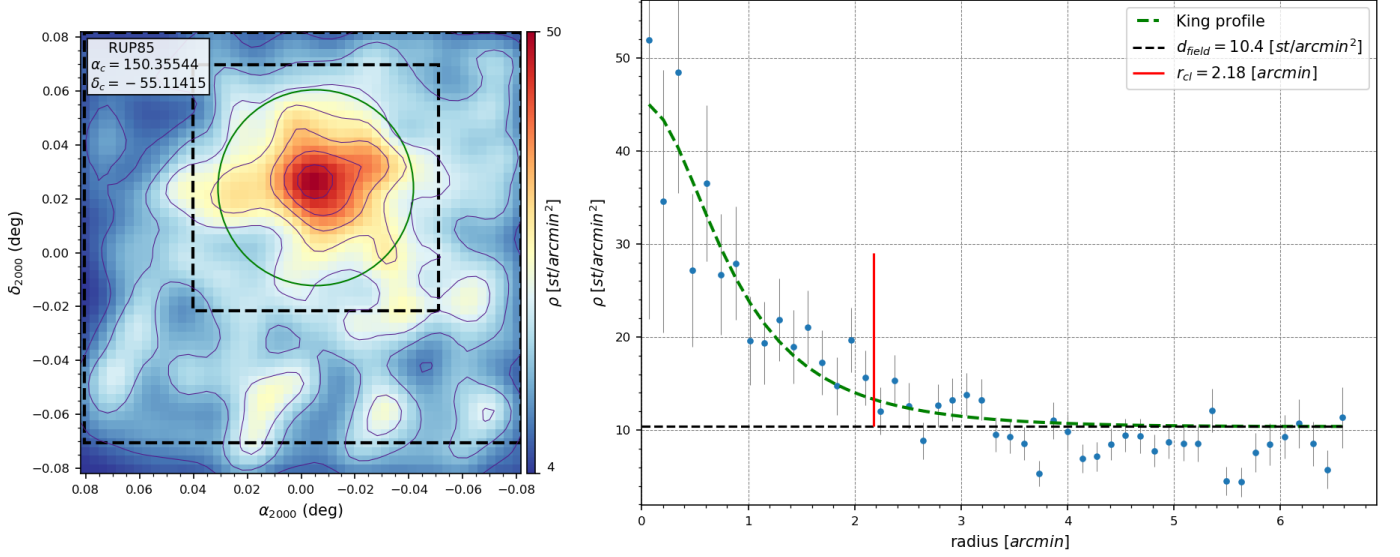


Fig. B.2. Idem Fig. 5 for RUP 85.

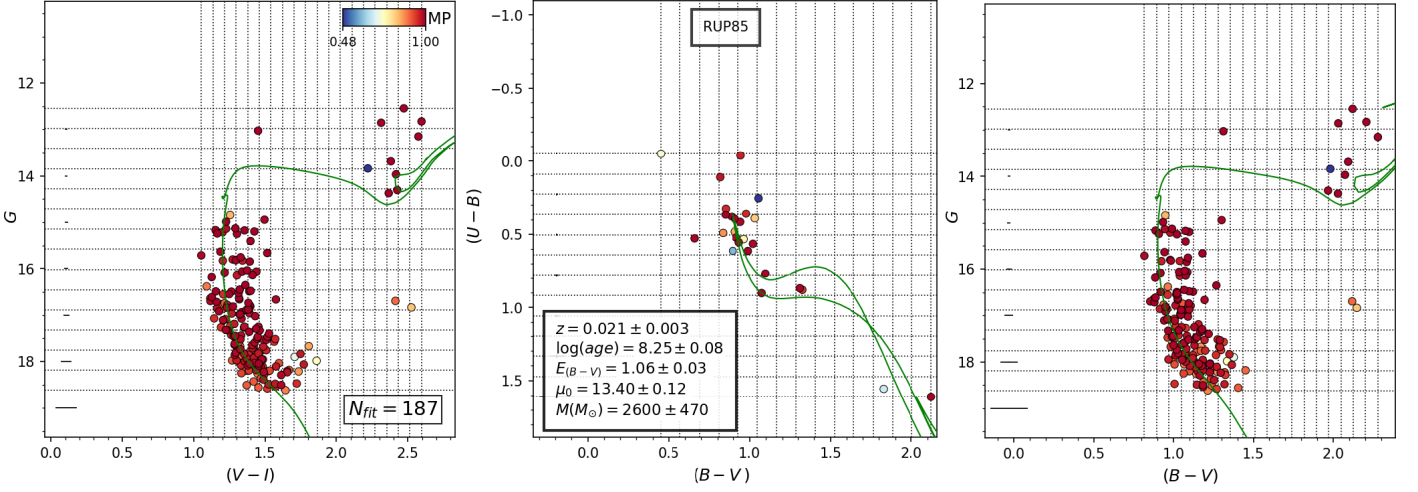


Fig. B.3. Idem Fig. 6 for RUP 85.

Appendix E: Trumpler 12

This object is placed in the west side of the Carina HII region where it appears as a sparse handful of bright stars in Fig. 3. The CMDs in Fig. E.1, including all stars in the region, show the following patterns: there is a wide grouping of stars below $G = 18$ mag but to the right side of it, and also at this magnitude value, a narrow structure of stars up to $G = 14$ mag slightly displaced to the blue side emerges. From $G = 18$ mag a typical vertical galactic disk population rises too.

AStEa detected a main overdensity in a region of high stellar contamination, as shown in Fig. E.2. This overdensity is characterized by a quite noisy RDP, a fact explained in part because at the peak of the RDP there is less than twice the density of the background. Under this condition it is not an easy task to fix an appropriate radius for the overdensity. We tentatively adopt ~ 2 arcmin radius as a reasonable compromise. The membership probabilities in the zone of the overdensity are mostly above 0.5 as indicated in Fig. E.3. Again, as in vdBH 87, the handful of low membership stars are very well detached from the main cluster sequence. A clear cluster main sequence can be seen in Fig. E.3

spanning roughly 4-5 mag. These stars belong to the tiny blue and narrow sequence detected easily in the diagrams of Fig. E.1 between $G = 12$ and $G = 16$ mag. Comparison with synthetic clusters yields the following values:

- A color excess of $E(B-V) = 0.31$ is found for the best fitting. Since the maximum color excess provided by S&F2011 is 0.50 we find that TR12 is placed in a zone of low absorption.
- The absorption free distance modulus is 12.7 ± 0.09 mag, representing a distance of 3.50 ± 0.15 kpc. At such a distance and with low absorption it is reasonable to find a high background stellar density as seen in Fig. E.2.

From the Anderson-Darling statistics shown in Fig. E.3 we see that proper motions for the cluster and for the field population belong to different samples. On the other hand, the parallaxes can not be safely separated into distinct stellar regions.

The clear cluster sequence and the low p -value (0.003) obtained with the AD test, leads us to conclude that TR 12 is a real cluster about $0.70 \pm 0.10 \times 10^9$ years old.

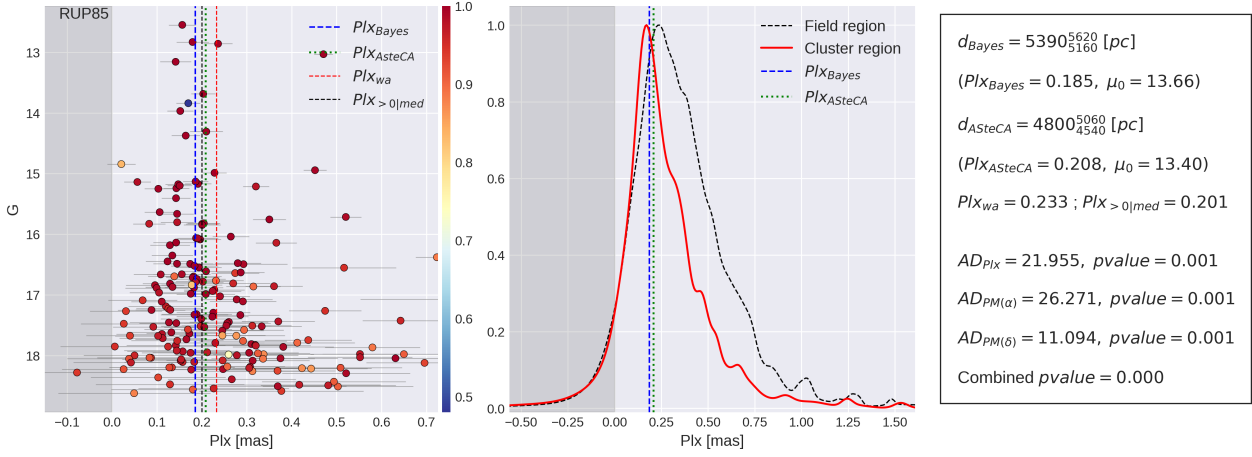


Fig. B.4. Idem Fig. 7 for RUP 85.

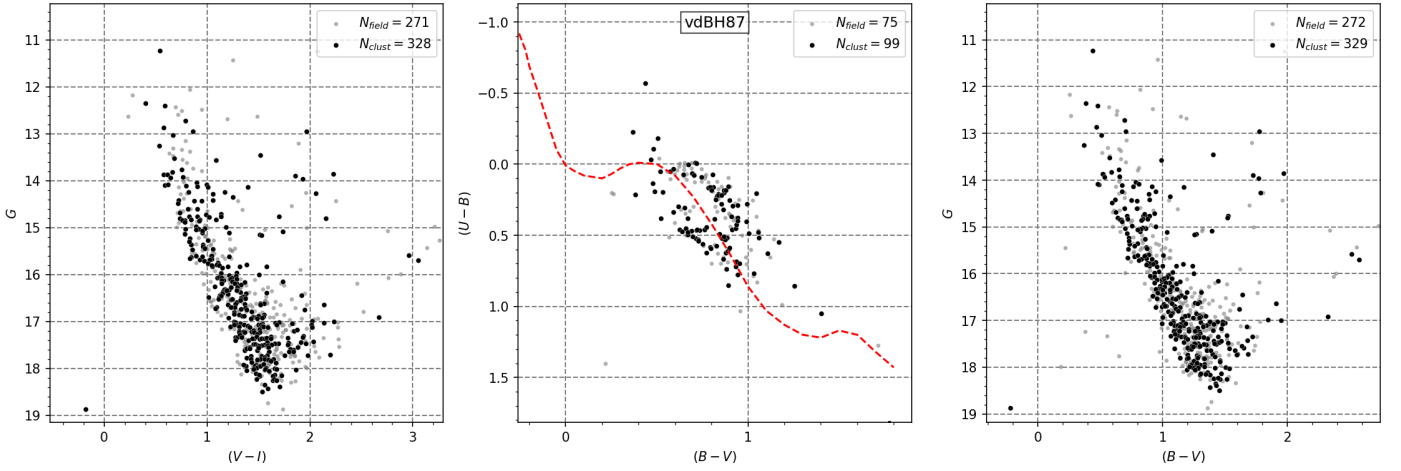


Fig. C.1. Idem Fig. 4 for vdBH 87.

Appendix F: van den Bergh-Hagen 91

vdBH 91 is a potential cluster at the west side of Carina HII region, specifically near the northern border of this constellation with Vela. No relevant stellar structure appears in the V image of Fig. 3 but a common pattern of a galactic field star near the galactic plane. The overall CMDs in Fig. F.1 show a stellar sequence that, at first sight, resemble the usual diagrams for open clusters. In turn, the CCD is dominated by a tail of F - and G -type stars prolonged by red stars. It is noticed as well the presence of some reddened early type stars for negative $(U - B)$ indices.

ASteCA found two well separated stellar overdensity peaks in Fig. F.2 whose relevance in terms of structure is not important given the overall low stellar density of the field. The noisy RDP proves by itself the poverty of the entire field surveyed in term of star number. After some attempts looking for a cluster sequence we ask ASteCA to estimate the probabilities for stars inside an adopted radius of ~ 2.5 arcmin, shown in Fig. F.2 (right). As seen in Fig. F.3 almost one hundred stars inside the circle associated to vdBH 91 were found in the CMDs. No clear cluster sequence is traced by stars with large probabilities, which are scattered across the entire CMDs. The absence of a cluster sequence combined with the poor and noisy overdensity are all against the reliability of this cluster.

The Anderson-Darling test in Fig. F.4, right panel, is clear regarding the true nature of vdBH 91 since the high combined p -value indicates that the null hypothesis (cluster and field areas come from the same originating distribution) can not be reasonably rejected. This result is against the Kharchenko et al. (2005) study where the authors found that vdBH 91 is a cluster at 0.75 kpc, approximately 0.16×10^9 yr old and affected by a mean color excess $E(B - V) = 0.08$.

We conclude that vdBH 91 is a random fluctuation of the stellar foreground/background, and not a real entity.

Appendix G: Trumpler 13

TR 13 is a weak object also at the south west of the Carina HII region, seen as a diffuse but extended star accumulation near the center of the V image in Fig. 3. The two CMDs in Fig. G.1 show an uncommon pattern: we see that above $G = 17.5$ mag the star sequence splits into two branches with one of them extending to the bluest side while other branch follows the common representation of galaxy disc stars. In the CCD the situation is the same: a wide and reddened band of potential B -type stars is placed for $(B - V) < 0.45$ and for $-0.25 < (U - B) < 0.5$ with a few more stars at negative $(U - B)$ index while another strip of stars goes from the characteristic place for F -type stars

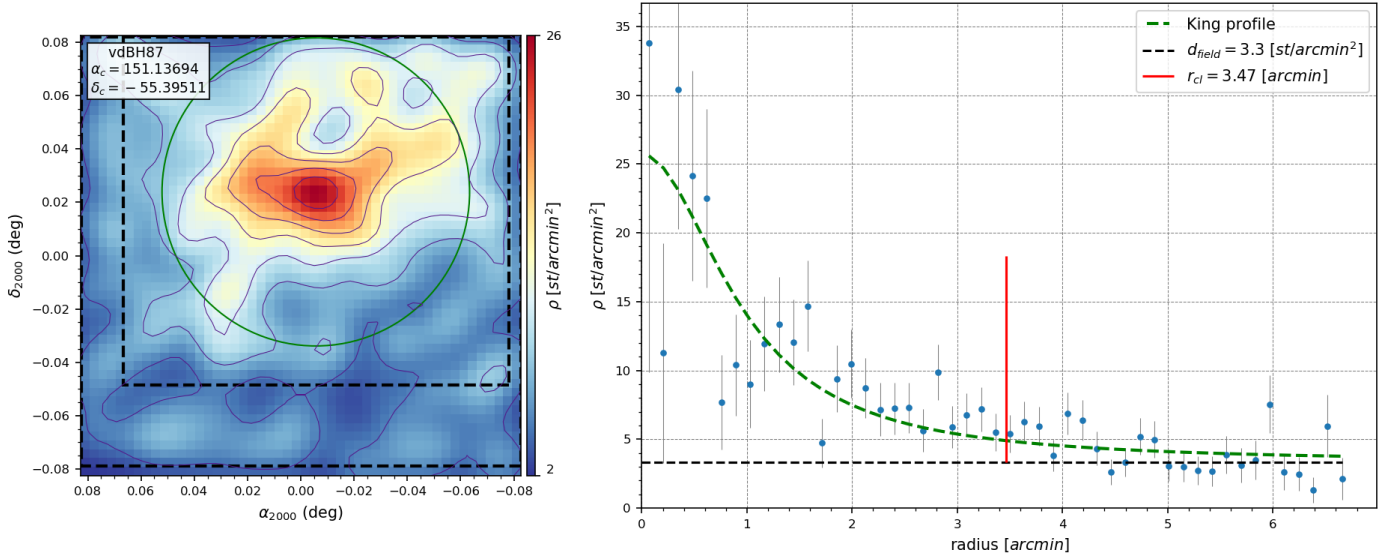


Fig. C.2. Idem Fig. 5 for vdBH 87.

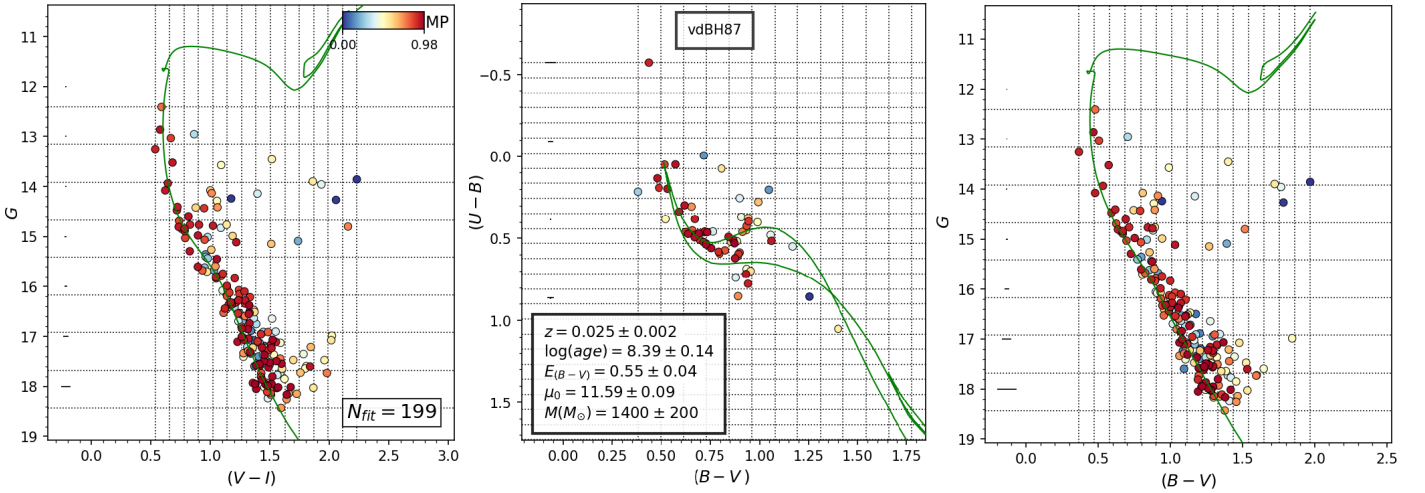


Fig. C.3. Idem Fig. 6 for vdBH 87.

extending to the red tail including probable giant stars.

Fig. G.2 indicates that ASteCA found a spatially extended overdensity mostly elongated north-south, which, at its peak is nearly 4 times above a mean field stellar density of ~ 26 stars per square arcmin. Given the shape and extension of the overdensity we adopted a formal radius of ~ 2.5 arcmin and asked ASteCA to compute the membership probabilities for those stars inside the area. ig. G.3 shows that after the removal of field interlopers, almost 170 stars are left composing a narrow cluster main sequence for more than 5 magnitudes. Consequently, when comparing with synthetic clusters the results yield:

- A color excess of $E(B - V) = 0.56$ is found for the best fitting of a synthetic cluster. Since the maximum color excess provided by S&F2011 is 1.94 it is reasonable to conclude that most of the absorption is produced behind the position of TR 13.
- The absorption free distance modulus of TR 13 is estimated to be 13.41 ± 0.15 mag, placing it at a distance of 4.81 ± 0.33 kpc from the Sun.

The Anderson-Darling statistics in Fig. G.4, right panel, confirm the photometric results: cluster area and the surrounding field region possess quite different properties.

The selected probable members inside the overdensity confirm the true nature of this object since the over density and the density profile are followed by a very well defined and extended photometric counterpart. All these facts combined with the results from the Anderson-Darling test are self-consistent, so that we are confident that TR 13 is a young cluster of $0.11 \pm 0.02 \times 10^9$ years old.

Appendix H: van den Bergh-Hagen 106

This cluster is placed at the south-east of the Vela constellation. The not so dense stellar field where it is placed has no relevant features except a few moderately bright stars as shown in Fig. 3. The CMDs shown in Fig. H.1 represent typical photometric features structures of galactic fields with no cluster inside. As for the CCD in the same figure it shows a reduced number of stars below the intrinsic line (probably reddened late *B*- and *A*-types) and a tail of stars from of late *F*-types to *M*-type stars –some

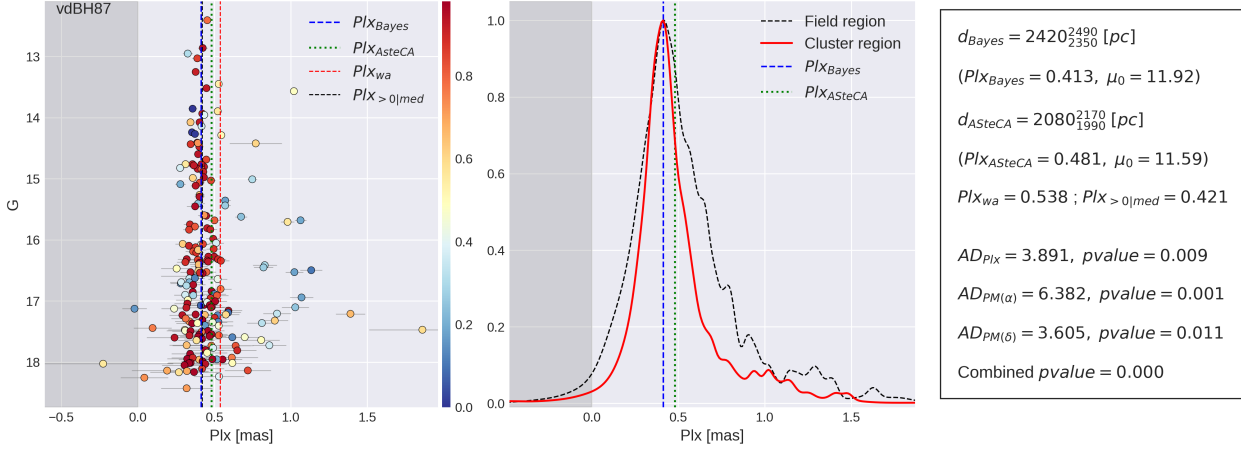


Fig. C.4. Idem Fig. 7 for vdBH 87.

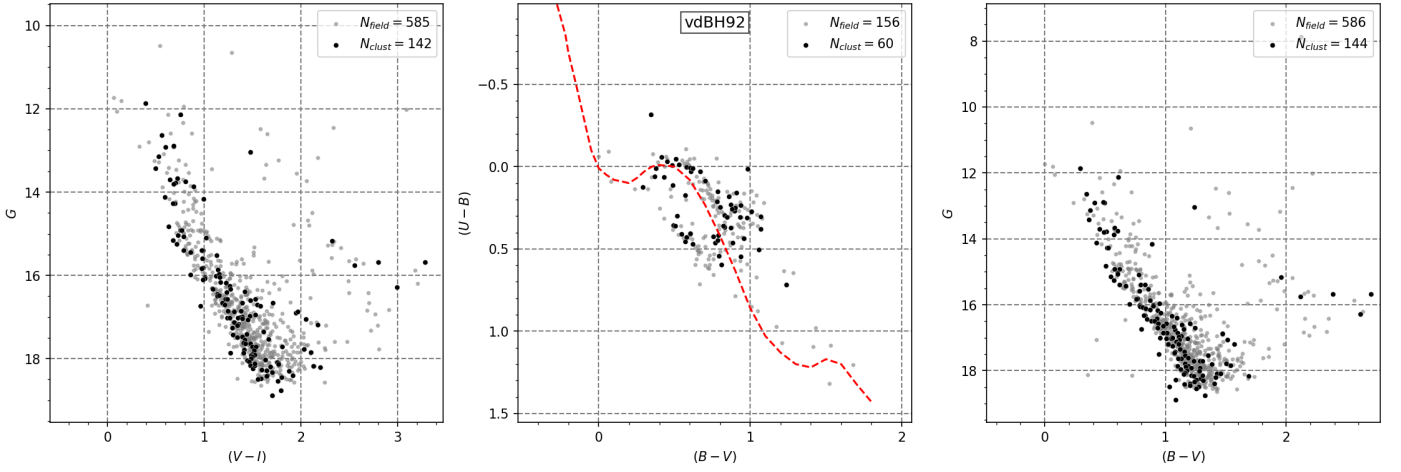


Fig. D.1. Idem Fig. 4 for vdBH 92.

of them probably giant- at the red end. ASteCA spatial analysis found some star clumps as seen in Fig. H.2, left panel. We focus the attention on the main one at the very center of the frame, since here we see the highest overdensity peak with ~ 3 times more stars than at the mean stellar background density of ~ 11 stars per square arcmin. We assume that most of stars in vdBH 106 must be included there so the cluster parameters should be well established. The RDP to the right appears not well defined since it reflects the irregular and poor star density even inside the zone selected to investigate the cluster parameters. Only 82 stars have been selected as probable members inside this area. Those stars having probabilities near the maximum values in this region would seem to outline a (rather noisy) cluster sequence that can be fitted with a synthetic cluster which yields the following parameters:

- A color excess of $E(B - V) = 0.30$ has been found to affect the cluster. This value is well in line with the maximum color excess provided by S&F2011, $E(B - V) = 0.57$ in this direction.
- The absorption free distance modulus of vdBH 106 was found to be 13.44 ± 0.36 mag, putting the cluster at a distance of $d = 4.87 \pm 0.81$ kpc from the Sun.

In this region we found from the application of the Anderson-Darling test that the parallax and proper motion distributions seem to belong to the same originating distribution,

as seen in Fig. H.4. Indeed, the large combined p -value makes the rejection of the null hypothesis difficult, if not impossible

Despite a trace of a sequence belonging to a typical old cluster is noticeable in Fig. H.3, we are cautious as to confirm its nature. Clearly deeper photometric observations (particularly in the U filter) are needed. Meanwhile and under the assumption that we are facing a true object vdBH 106 could be an old open cluster around $3.00 \pm 0.80 \times 10^9$ years old.

Appendix I: Ruprecht 88

RUP 88 is another potential cluster south of the Carina HII region. Like other objects in this paper no obvious stellar grouping is perceived in the V image of Fig. 3. The overall star CMDs in Fig. I.1 show a scattered star distribution above $G = 16$ mag. From this magnitude down the common pattern of galactic disc stars takes place in the CMDs. The CCD in Fig. I.1 suggests that no blue and therefore young star is present in the region of RUP 88. In the range $0.2 < (B - V) < 0.8$ we see a handful of stars that could be reddened late of late B -types or A - F -type stars. The remaining of this diagram is a trace composed by A - to M -type stars.

As with other clusters in the present sample, when the spatial distribution of stars in the frame is analyzed no clear star

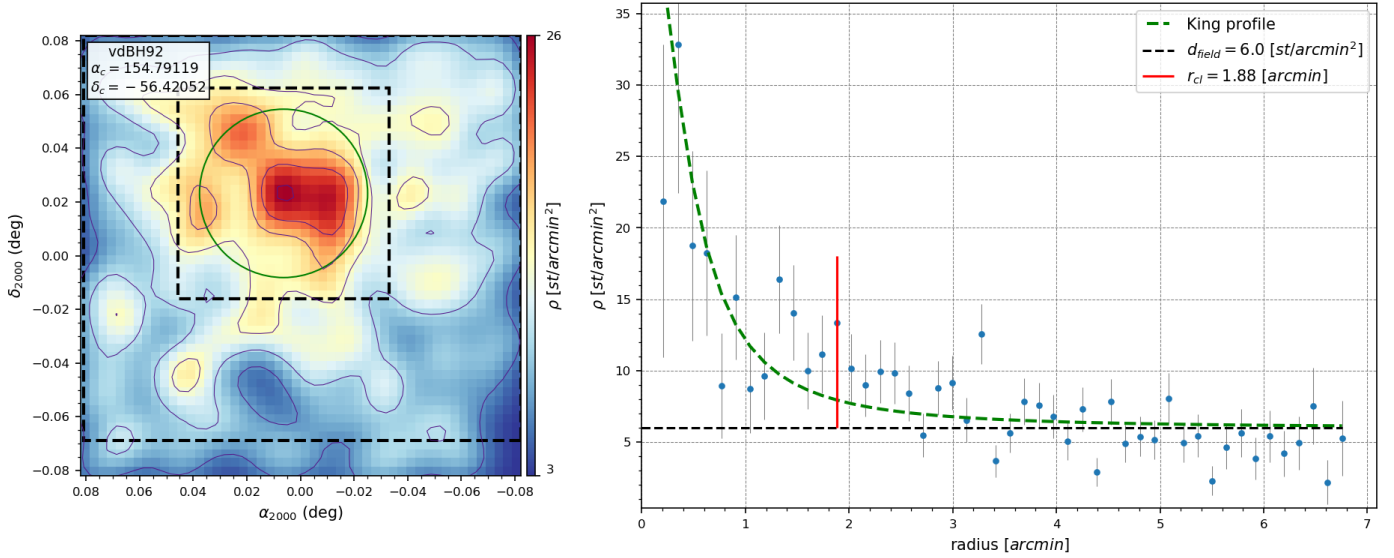


Fig. D.2. Idem Fig. 5 for vdBH 92.

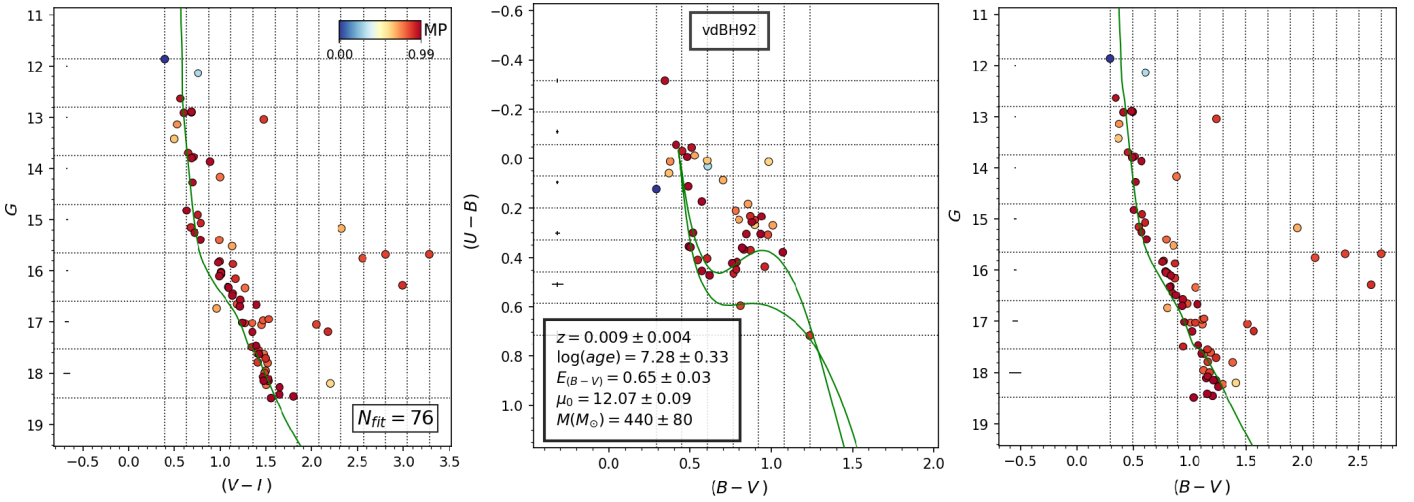


Fig. D.3. Idem Fig. 6 for vdBH 92.

overdensity appears in the location where RUP 88 is supposed to exist. In fact, the contour plot in Fig. I.2, left panel, shows a poor star number enhancement from south west to northeast of the frame extending north west. Given the difficulties to state the position of the cluster center (if it exists) we ask ASteCA to inspect the region encircled in green in Fig. I.2, where a reasonable density profile could be found. The RDP is still noisy because of a rather poor star number contained between the assumed cluster limits. If we look at the CMDs in Fig. I.3 only 42 stars with a wide range of probabilities remain inside the adopted cluster region after interlopers are removed, with no trace of a cluster sequence found. The three photometric diagrams in Fig. I.3 confirm this point as only an amorphous distribution of stars scarcely resembling a cluster main sequence can be seen.

The Anderson-Darling test in Fig. I.4, right panel is unable to separate the cluster population from the one from the field region, for the three explored dimensions. The combined p -value for proper motions and parallaxes is large, suggesting that both samples come from the same population. The necessary requirement that there is a reasonable main sequence is absent and,

combined with this result, precludes concluding that RUP 88 is a true cluster.

Appendix J: Ruprecht 162

Placed to the south east of the Carina HII region, the V image of the region in Fig. 3 where the cluster is supposed to exist shows a moderate number of stars resembling a star grouping placed at the north-west in the frame. At first glance the CMDs in Fig. J.1 for the overall stars look as if a cluster main sequence is emerging from the trace of the disk star distribution. In the same figure, middle panel, the CCD splits into two star groups: one of them is mostly placed below the intrinsic line for $0.0 < (B - V) < 0.8$ and resembles a strip of reddened blue stars (including early and late B -types and, perhaps, some A -type stars); the other group shows a distribution of F - to M -type stars strongly affected by reddening in appearance.

ASteCA detected an extended and irregular region at the north-west of the frame in Fig. J.2 (where the cluster is supposed to be). Given the difficulties to set a clear overdensity we decided to focus the attention on the ~ 3 arcmin zone encircled

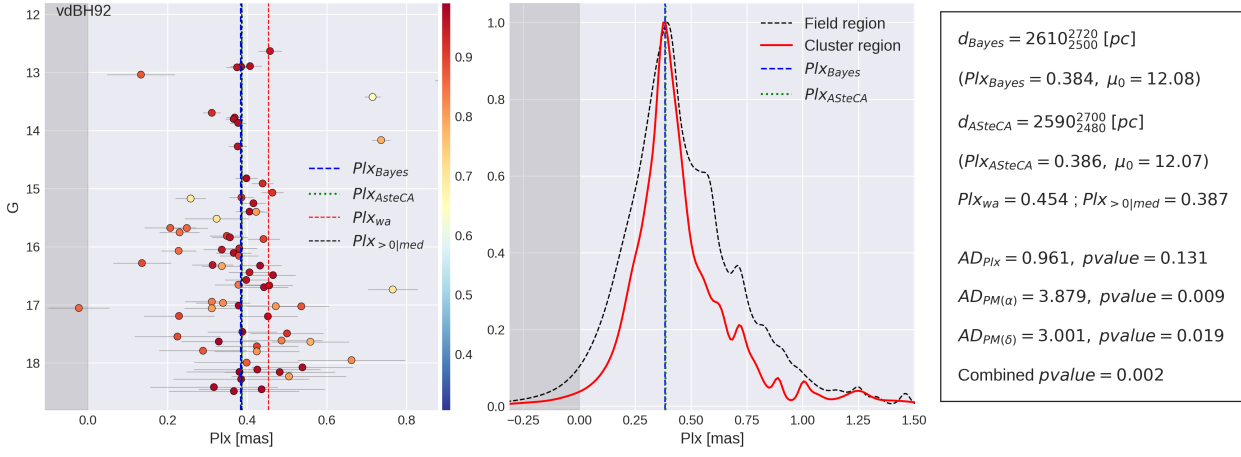


Fig. D.4. Idem Fig. 7 for vdBH 92.

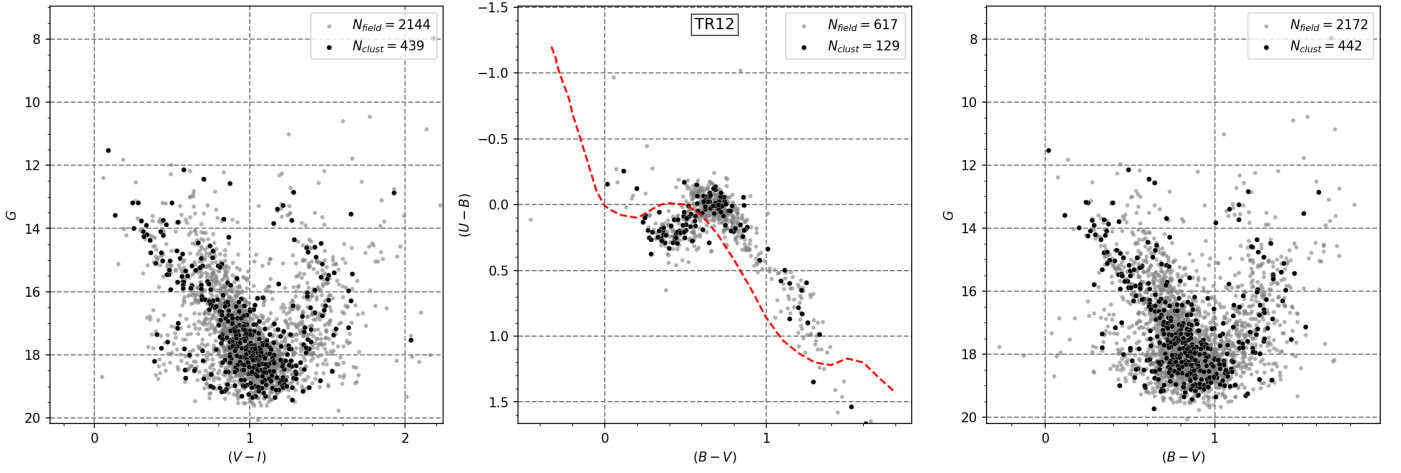


Fig. E.1. Idem Fig. 4 for TR 12.

in green in Fig. J.2, left panel. The background mean star density is over 20 stars per squared arcmin and, at the most, the overdensity is just 40 stars at the maximum. This produces unavoidably a noisy RDP (it is hard to establish a meaningful radius and there is a quite irregular star distribution across the zone).

The CMDs and CCD in Fig. J.3, after the removal of field interlopers, show more than 200 dispersed stars, most of them with large probabilities assigned. The large scatter in the CMDs and the large MP values assigned even to stars that are clearly not part of any cluster sequence, point against the existence of a true cluster in the region. On the other hand the cleaned CCD, Fig. J.3 mid panel, shows a blue sequence of stars suffering some internal color scatter followed by a tail of F - to K -type stars. Therefore this object could be more extended than supposed. ASteCA found the best fitting with a synthetic cluster with the following properties:

- The color excess affecting the cluster is $E(B-V) = 0.54$, well below the maximum value given by S&F2011 who estimate $E(B-V) = 1.07$.
- The absorption free distance modulus is 13.23 ± 0.10 mag corresponding to a distance of $d = 4.43 \pm 0.20$ kpc.

Anderson-Darling statistical test results are shown in Fig. J.4, right panel. Parallaxes and proper motions $PM(\alpha)$ and $PM(\delta)$ in the location of RUP 162 and the surrounding field

region do not seem to be different enough from each other as to be efficiently disentangled.

Although weak enough the presence of a probable main sequence in the panels of Fig. J.3, make us cautious leaving some chance for RUP 162 to be a true cluster about $0.80 \pm 0.20 \times 10^9$ years old. An additional reinforcement as for the hypothetical true entity of this young object is the existence of a sudden gap along the main sequence at $G = 16.5$ mag and the presence of high probability stars at the red side resembling traces of a pre-main sequence. Certainly we are just speculating on this fact so that more and deeper observations are needed to arrive to a concluding result for RUP 162.

Appendix K: Lynga 15

This is an intriguing object placed in Centaurus, south west between Crux and the east border of Carina. More specifically, Lynga 15 is about 1° north-east of the star formation region SFR293.64-1.41 (Avedisova 2002). Like in many other cases already shown in the V images in Fig. 3 this region does not show, at first glance, any prominent stellar feature though some stars are bright enough as to attract attention to this place. However, the overall CMDs and CCD shown in Fig. K.1 are quite surprising since both CMDs depict an extended sequence (from $G = 8$ down to $G = 15.5$ mag) emerging toward the left

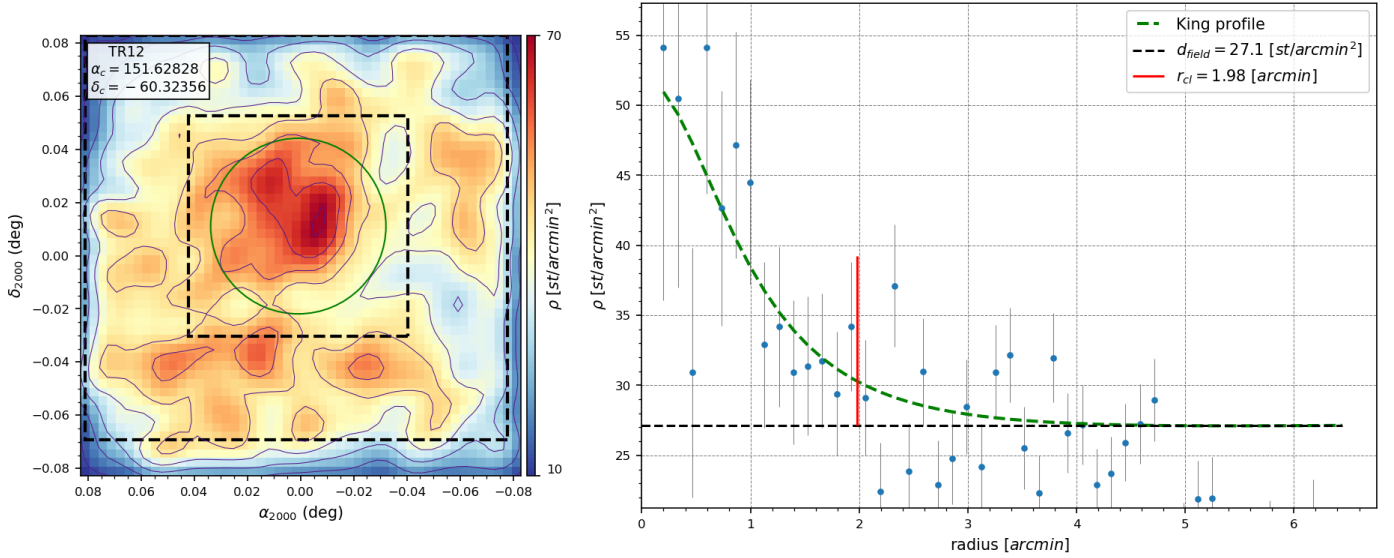


Fig. E.2. Idem Fig. 5 for TR 12.

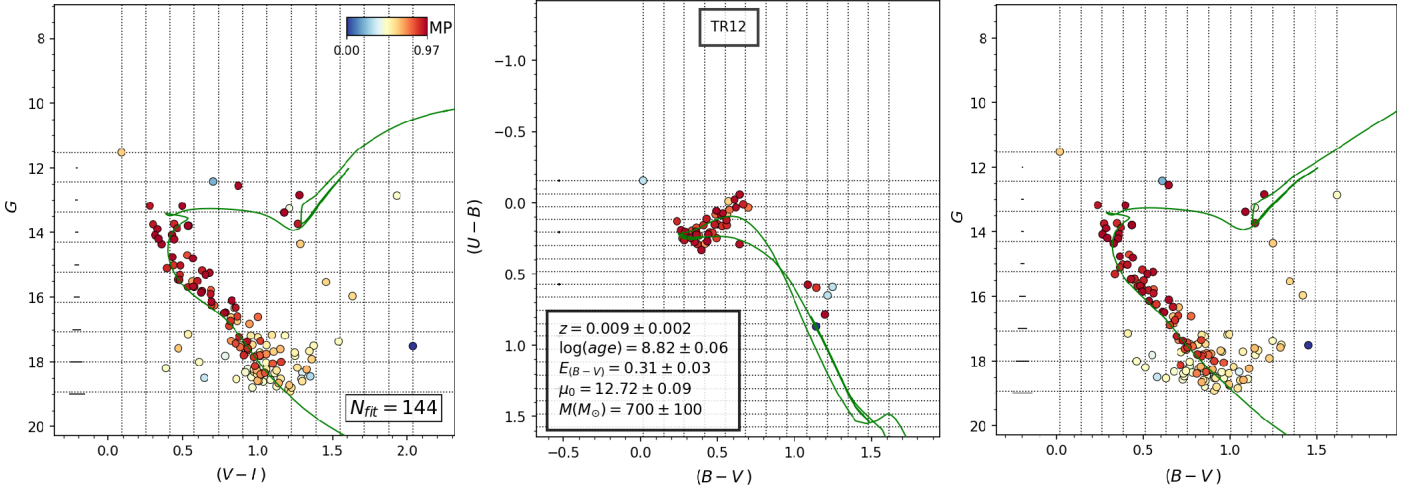


Fig. E.3. Idem Fig. 6 for TR 12.

side of the main disc population trace. In the same figure, middle panel, the CCD shows a strip of blue stars ($0.0 < (B - V) < 0.0$) accompanied by other, probable reddened early type stars, placed above $(U - B) = 0.0$. The picture seen in the three panels of Fig. K.1 induces to think of Lynga 15 as a quite young open cluster.

In turn, ASteCA analysis of the spatial structure found an extended and irregular stellar density with no indication of a clear overdensity. The observed frame's density map shows two very distinct stellar densities, explained by the combination of observations made by two different telescopes detailed in Sect. 3 (same as NGC 4349). After many attempts to look for the place where the star membership probabilities reach the highest values we adopted a ~ 2.9 arcmin radius and set the potential cluster center in the literature coordinates as indicated in Fig. K.2, left panel. In this place, the RDP displays a ~ 45 stars per squared arcmin peak above the stellar field density, as seen in the right panel of Fig. K.2. Even in this position ASteCA yields a conflictive result since the selected probable members show a large dispersion and, as seen in Fig. K.3 left and right panels, a probable cluster main sequence mostly composed by

lower probability stars appears below approximately $G = 17$ mag. Above this visual magnitude the main sequence vanishes and we are left with just a handful of stars with rather large probability values, scattered in color index and magnitudes. This is, no upper cluster main sequence is evident in the clean CMDs. The CCD in the mid panel of Fig. K.3 contains a few blue stars with no counterpart in the CMDs. This could be explained this way: all across the surveyed region there are blue stars (see the overall CCD in Fig. K.1) composing a sort of Blue Plume in the respective CMDs and just by chance some blue stars also appear in the potential cluster region after ASteCA analysis (mid panel Fig. K.3). It could be possible yet that Lynga 15 is an extended open cluster (even larger than the size of our frame), but the presence of the huge star gap above $G = 17$ mag is unexplainable in a CMD from a statistical point of view. In our opinion and from a photometric and spatial point of view Lynga 15 is not an open cluster. The application of the Anderson-Darling test inform us that the properties of stars inside the adopted cluster radius and outside of it are similar, with a probability of $\sim 6\%$ of mistakenly rejecting the null hypothesis that both samples arose from the same distribution.

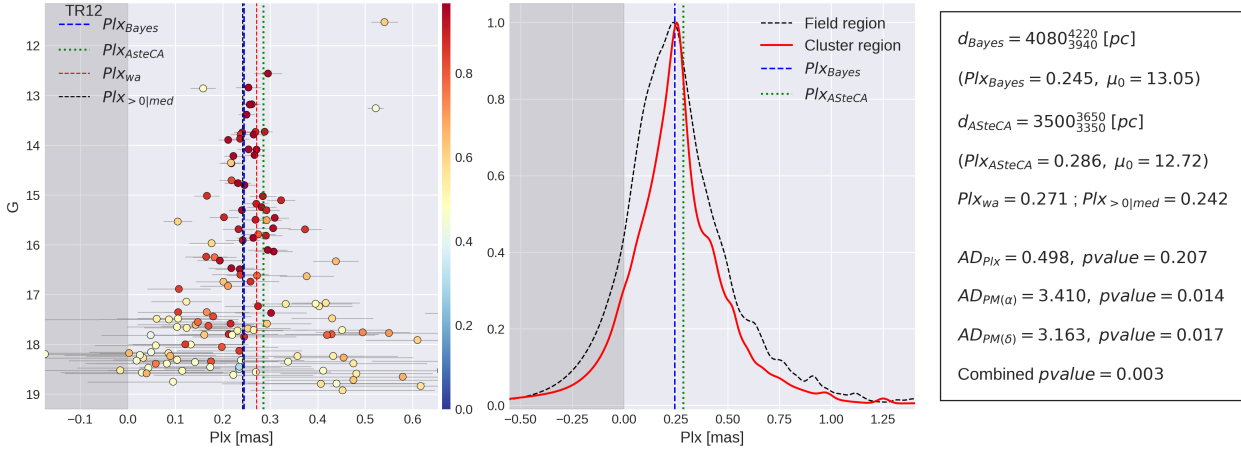


Fig. E.4. Idem Fig. 7 for TR 12.

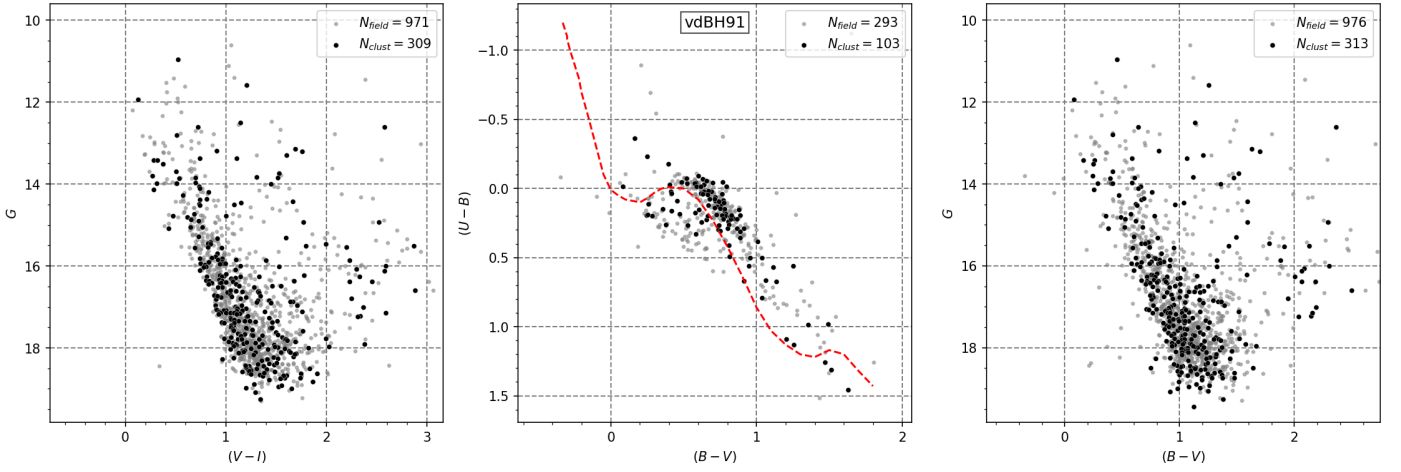


Fig. F.1. Idem Fig. 4 for vdBH 91.

We conclude that Lynga 15 is not a true cluster but a superposition of blue stars at several distances along the line of sight. This is not odd at all since this object is not far from the galactic equator so it is probable that blue stars are seen along the direction to this potential cluster.

Appendix L: Loden 565

Placed toward the west side of the Crux constellation the V image in Fig. 3 of Loden 565 does not show any evident star grouping. Inspection of the CCD and CMDs in Fig. L.1 only suggests the presence of a dispersed star group down to $G = 15 - 16$ mag approximately. From this magnitude down the overall CMDs show the common pattern of galactic disc star population and nothing relevant can be seen in the CCD in the mid panel of Fig. L.1, but a modest handful of probable slightly reddened late blue stars for $(B - V) < 0.6$.

ASteCA found an irregular overdensity at the north-west corner of the frame as seen in Fig. L.2, left panel. This is the only region across the entire field where a sudden increase in the star number per area unit is noticeable showing a ~ 40 stars per squared arcmin peak at its maximum in Fig. L.2, right panel. When looking for membership probabilities only a small number of 60 stars remain inside the adopted radius with larger probabilities scattered towards lower magnitudes. No clear

main sequence can be seen present in the CMDs in Fig. L.3. Notice that none of the stars that occupy the CCD of Fig. L.1 (right panel) with $0 < (B - V) < 0.6$, with some chances to be reddened early type stars, remain inside the adopted area after ASteCA's membership analysis. The stars that ASteCA identified inside the adopted radius could be members of an old group but we conclude that the photometric evidences are not conclusive at all. More extended and deeper observations are necessary. Previous estimates of the cluster parameters found for Loden 565 can be found in Kharchenko et al. (2005). These authors concluded that Loden 565 is a moderately young cluster placed at a distance of $d = 0.65$ kpc, affected by a mean reddening $E(B - V) = 0.2$ and a little older than 10^8 yrs. The Kharchenko et al. (2005) atlas shows a poor fitting to a very sparse available data. In addition, when inspecting the results from the Anderson-Darling test in the right panel of Fig. L.4, it becomes evident that the cluster region is indistinguishable from the stellar background in terms of parallax and proper motion distributions, exactly as the clean CCD and CMDs show in Fig. L.3.

In conclusion, Loden 565 is more probably a stellar fluctuation.

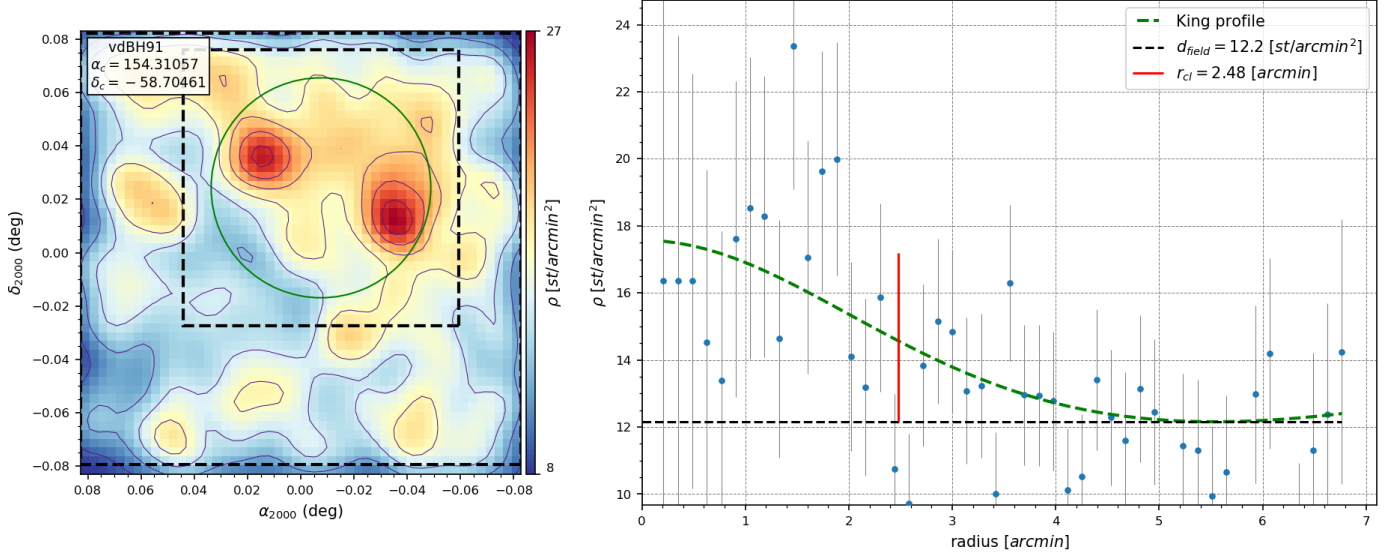


Fig. F.2. Idem Fig. 5 for vdBH 91.

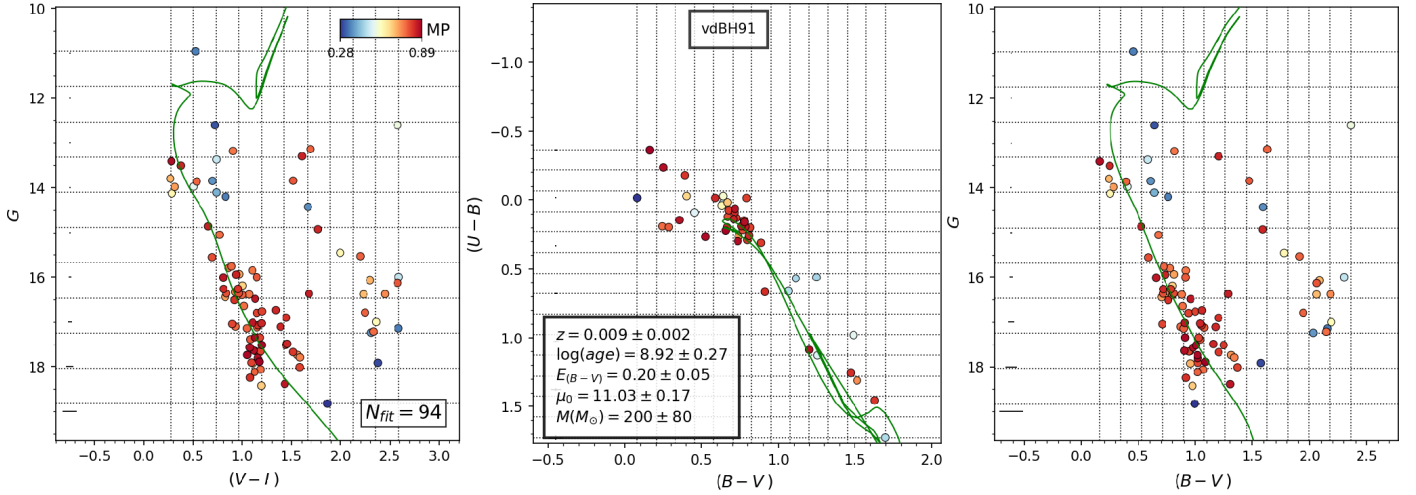


Fig. F.3. Idem Fig. 6 for vdBH 91.

Appendix M: NGC 4230

This object belongs to the Centaurus region immediately close to the upper border of Crux. The V image in Fig. 3 shows that we are facing just a modest star grouping near the high proper motion star HD 106826 with 8.8 mag. Nothing relevant is appreciable in the V image of the inspected zone except the star already mentioned. A highly scattered and diffuse star distribution resembling a galactic disc stellar pattern appears in the overall CCD and CMDs in the panels of Fig. M.1.

The spatial inspection performed by ASteCA detected a group of small stellar overdensities surrounding the central prominence as shown in Fig. M.2, left panel. The peak of the central overdensity shows that the number of stars per area unit is three times the mean of the background, and the respective RDP in the right panel of Fig. M.2 suggests a ~ 2 arcmin radius. However, ASteCA yielded a frustrating result in terms of what it is expected for a real cluster when analyzing the stellar properties inside and outside the overdensity. Only 46 stars remain inside the limits we adopted for NGC 4230. The synthetic cluster fit is found for the low mass stars with the

larger MP values. At this low number of members and with this large dispersion there is no way to confidently separate the stellar population into those objects belonging to a (putative) real open cluster and those others belonging to the stellar field. The CCD and CMDs of these stars in Fig. M.3 reflect the physical situation since no main sequence is evident at all. At most, there is a sort of badly defined giant star sequence whose meaning is dubious because there is no trace of a main sequence. The comparison with synthetic clusters performed by ASteCA fitted mainly a group of stars with low brightness, as shown in the CMDs of Fig. M.3. This cluster is analyzed in Tadross (2011) where the authors find an old 1.7 Gyrs cluster, younger to our result of ~ 8 Gyrs, and at a much closer distance (1445 pc versus our result of about 4300 pc) Therefore the studies do not coincide in the nature of this supposed cluster.

Results for the distribution of parallax values and proper motions for the cluster and field regions are shown in Fig. M.4, right panel. We see that the Anderson-Darling statistics reveals that the parallax and proper motions distributions are very similar to stars outside the cluster region.

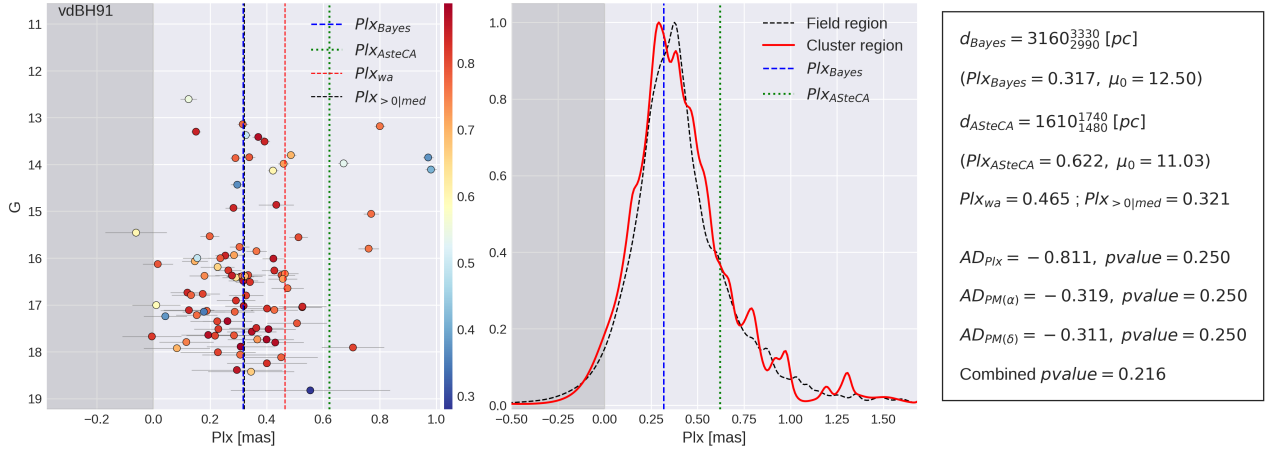


Fig. F.4. Idem Fig. 7 for vdBH 91.

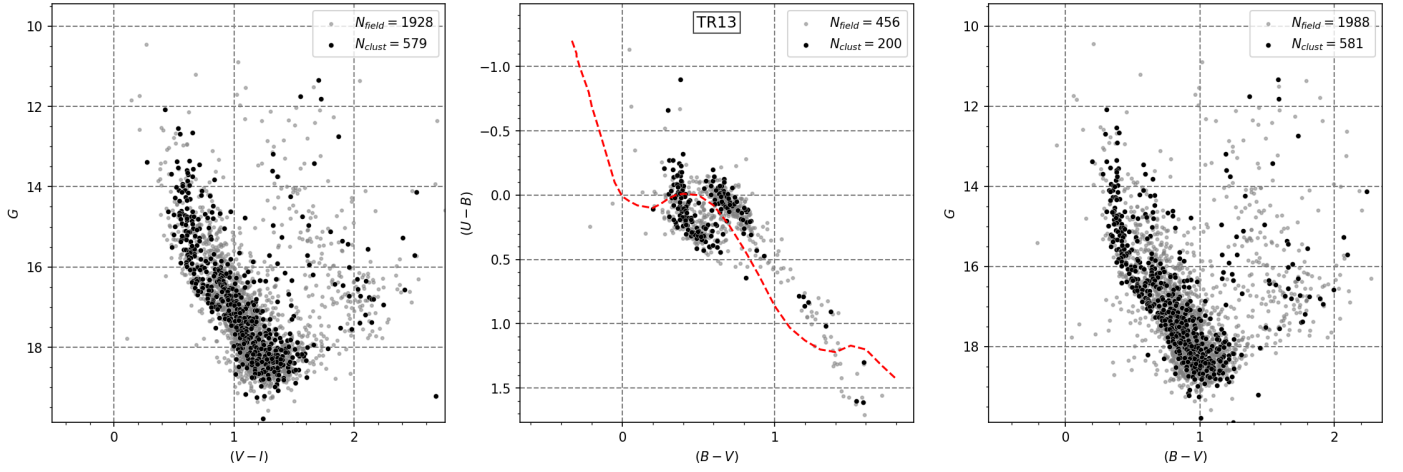


Fig. G.1. Idem Fig. 4 for TR 13.

The lack of a well-defined photometric sequence proper of an open cluster as demonstrated in Fig. M.3 together with the results from the statistical comparison is enough argument to exclude NGC 4230 as a true open cluster, becoming most probably a random fluctuation of the stellar field.

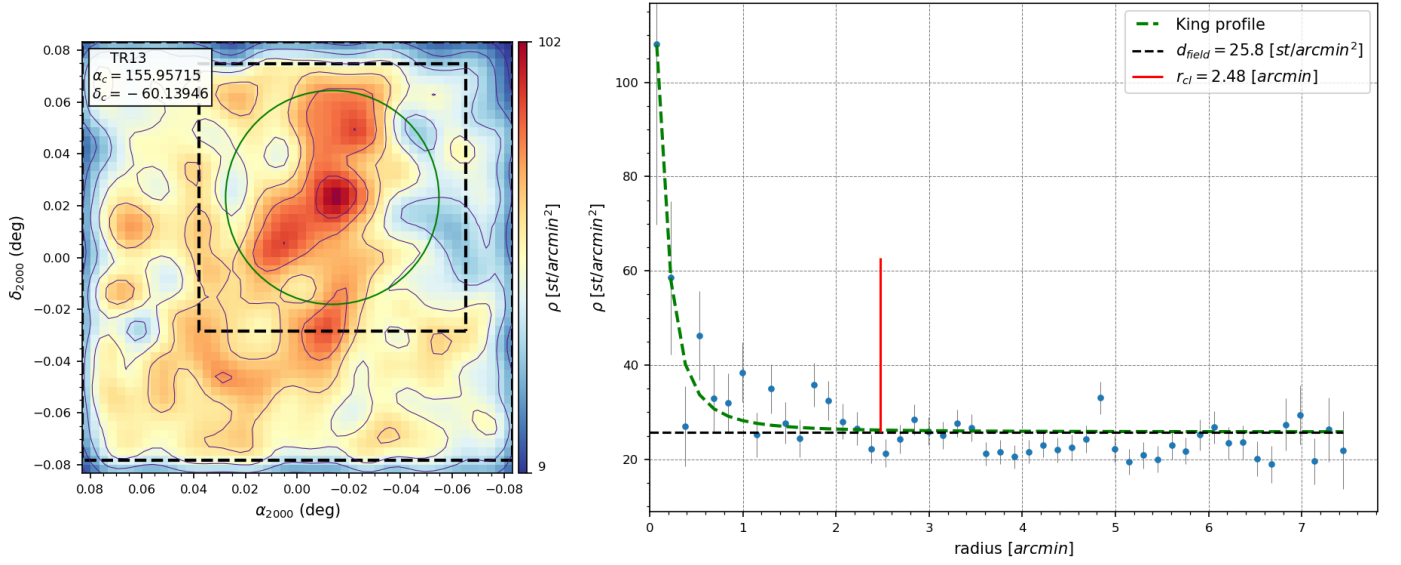


Fig. G.2. Idem Fig. 5 for TR 13.

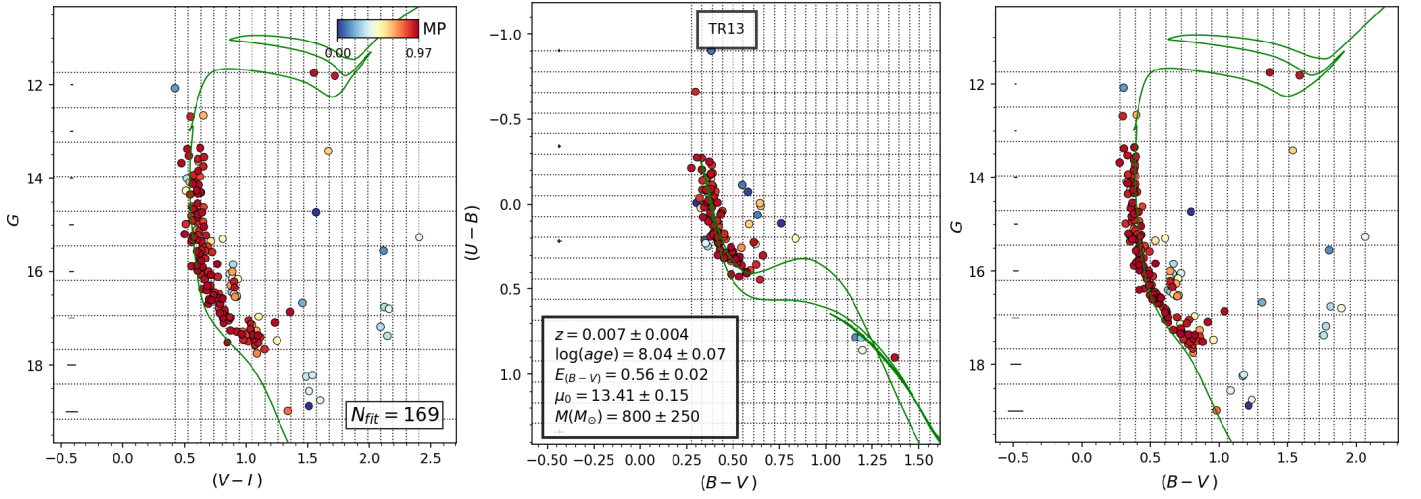


Fig. G.3. Idem Fig. 6 for TR 13.

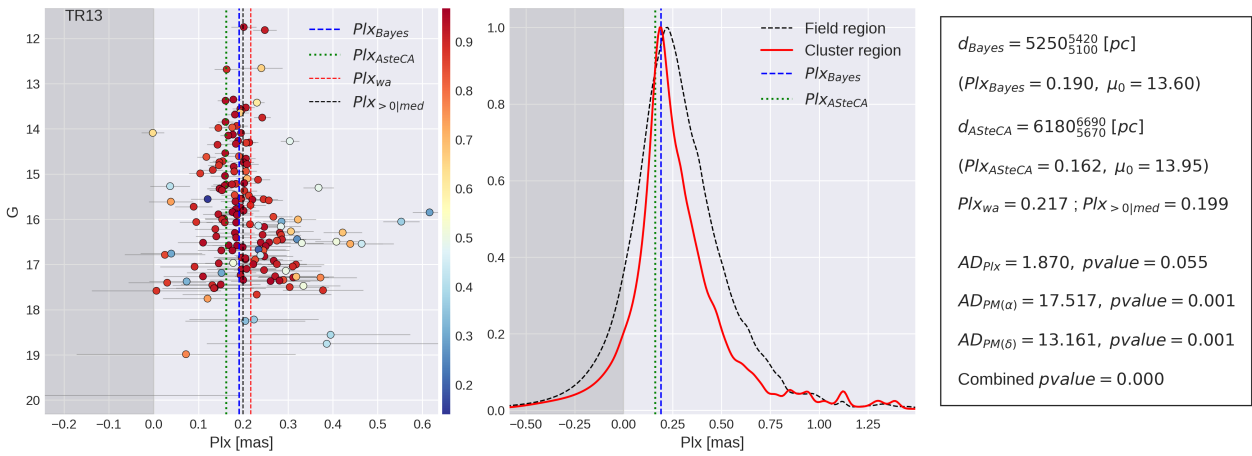


Fig. G.4. Idem Fig. 7 for TR 13.

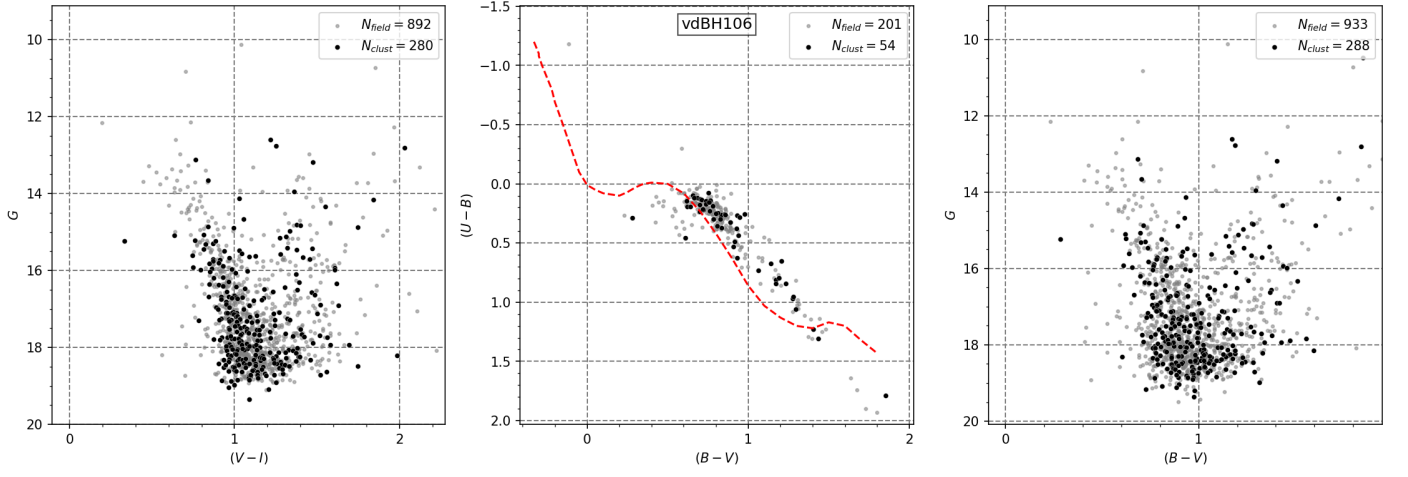


Fig. H.1. Idem Fig. 4 for vdBH 106.

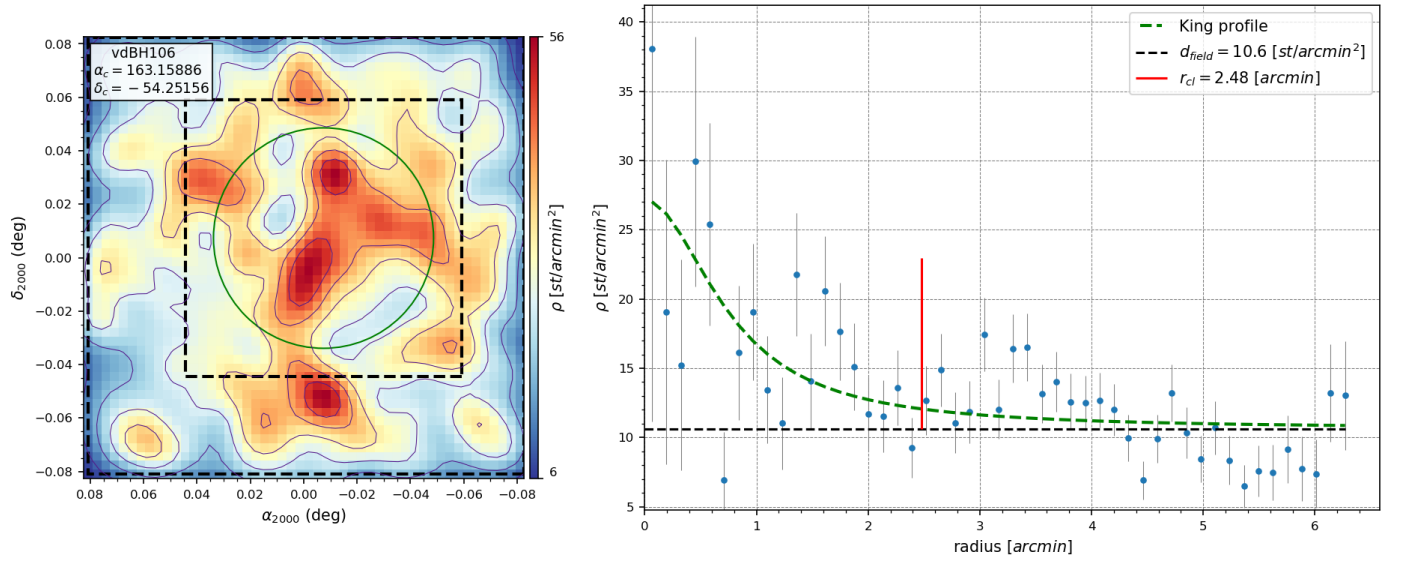


Fig. H.2. Idem Fig. 5 for vdBH 106.

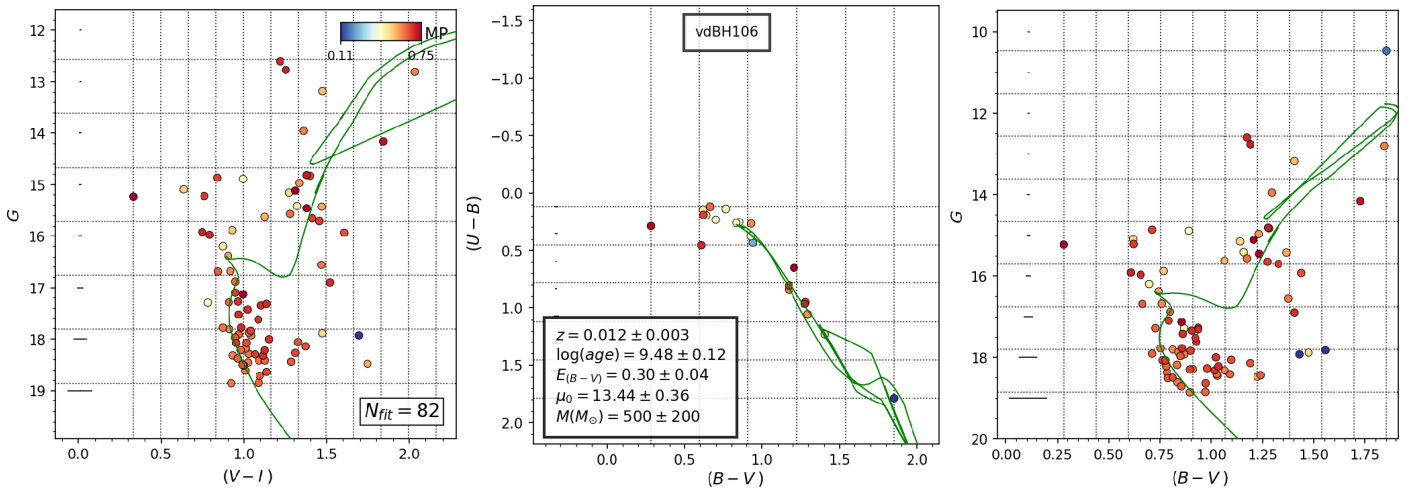


Fig. H.3. Idem Fig. 6 for vdBH 106.

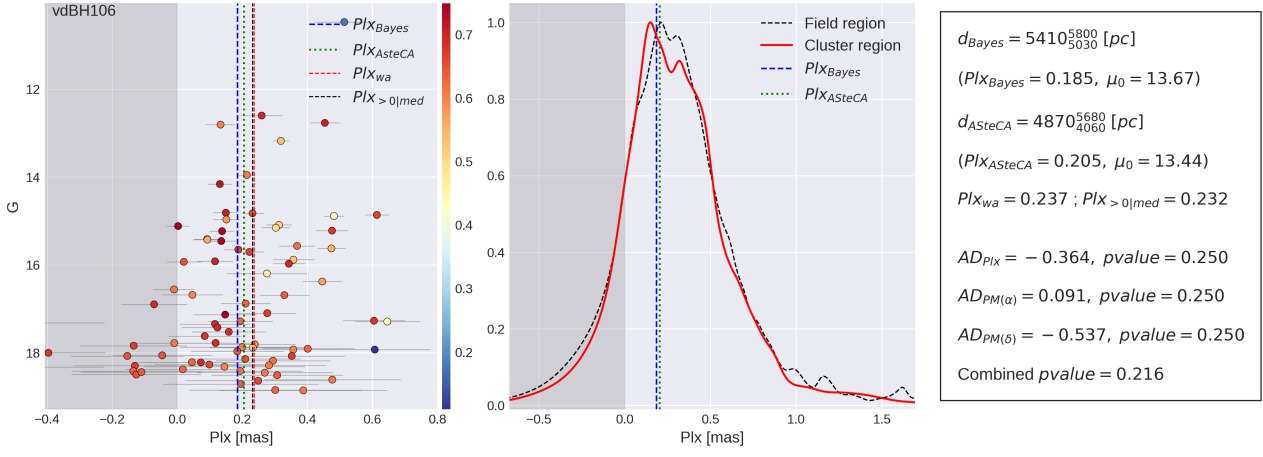


Fig. H.4. Idem Fig. 7 for vdBH 106.

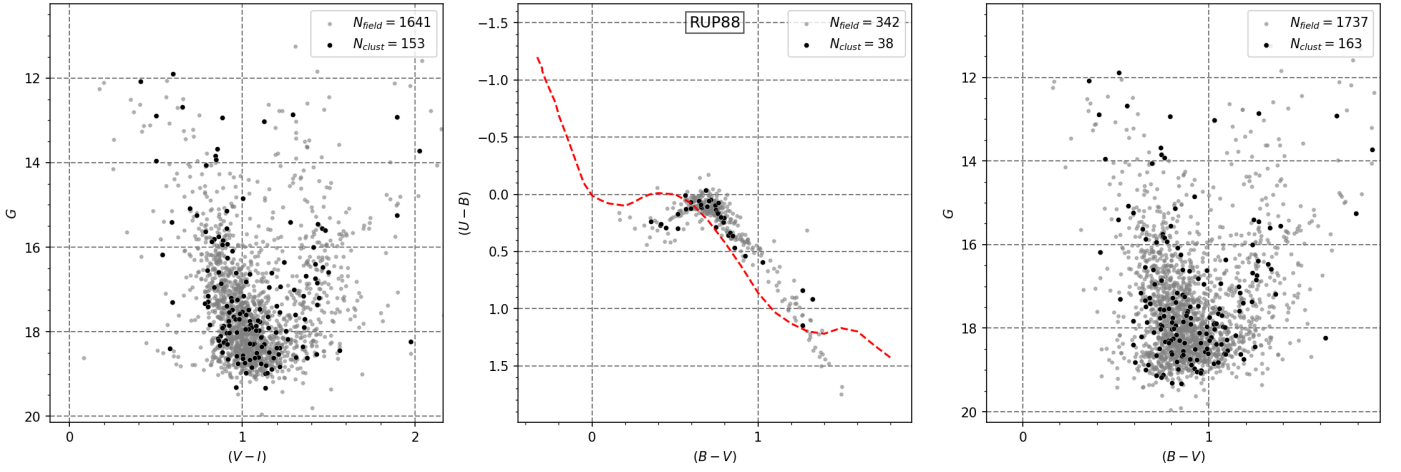


Fig. I.1. Idem Fig. 4 for RUP 88.

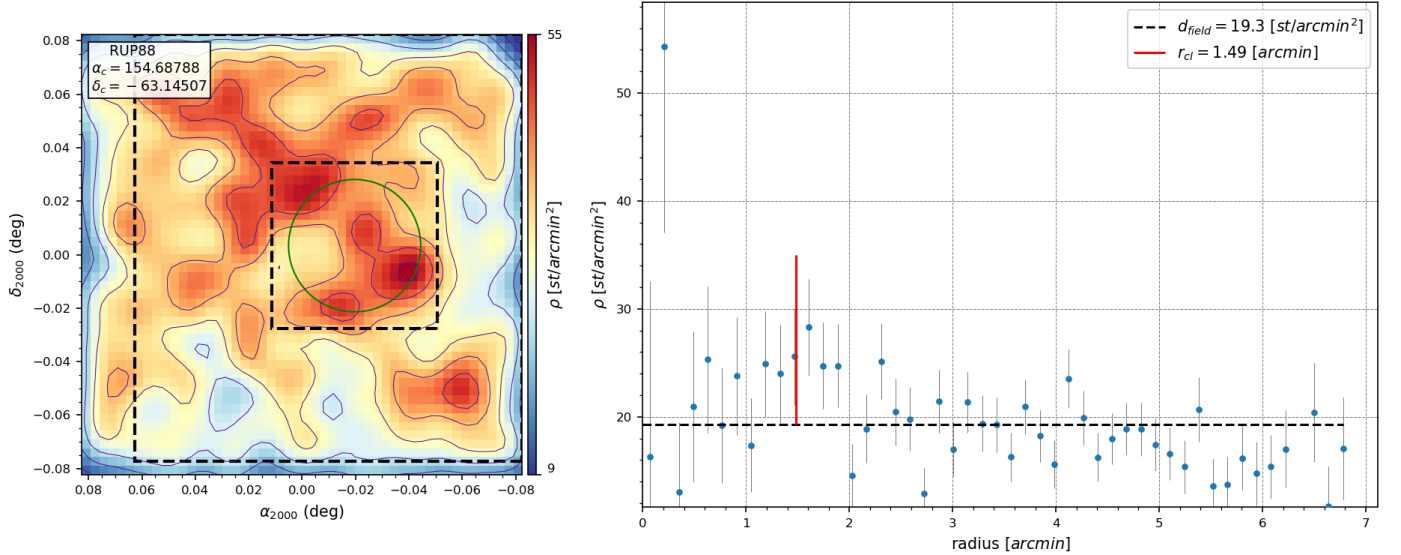


Fig. I.2. Idem Fig. 5 for RUP 88.

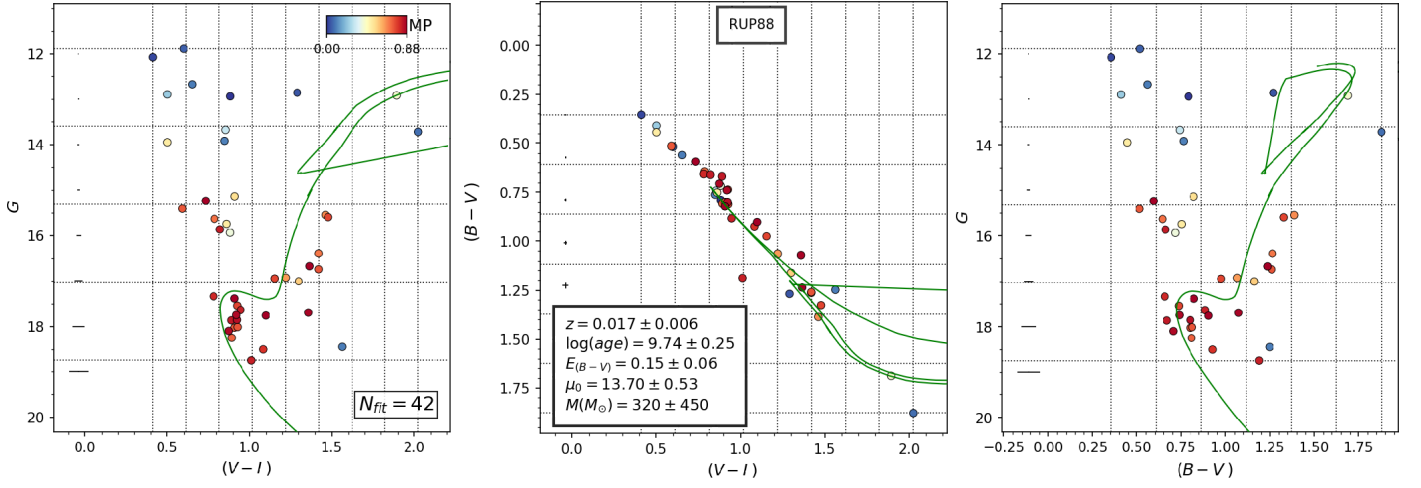


Fig. I.3. Idem Fig. 6 for RUP 88 with the $(B - V)$ vs $(V - I)$ diagram instead of the $(B - V)$ vs $(U - B)$ diagram.

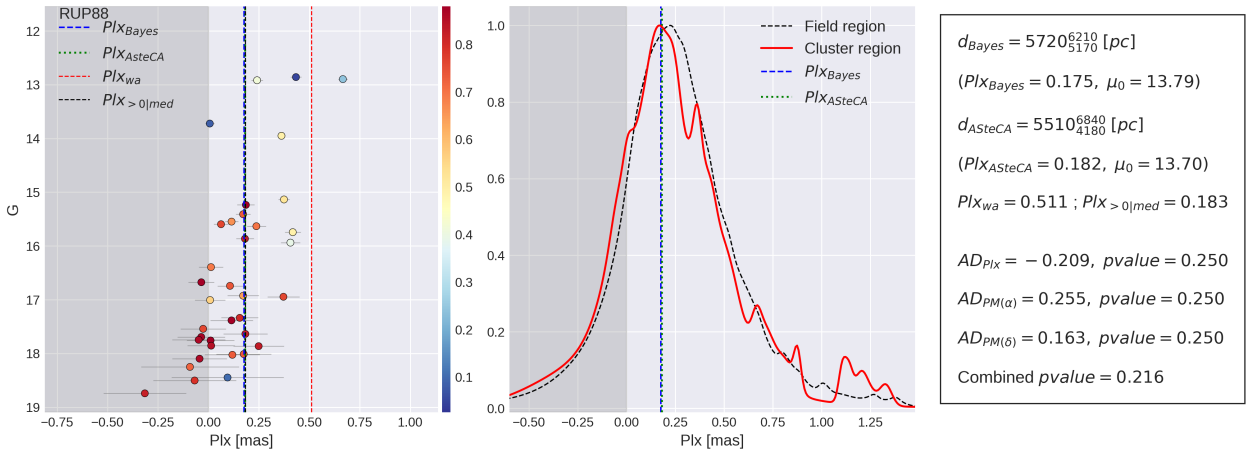


Fig. I.4. Idem Fig. 7 for RUP 88.

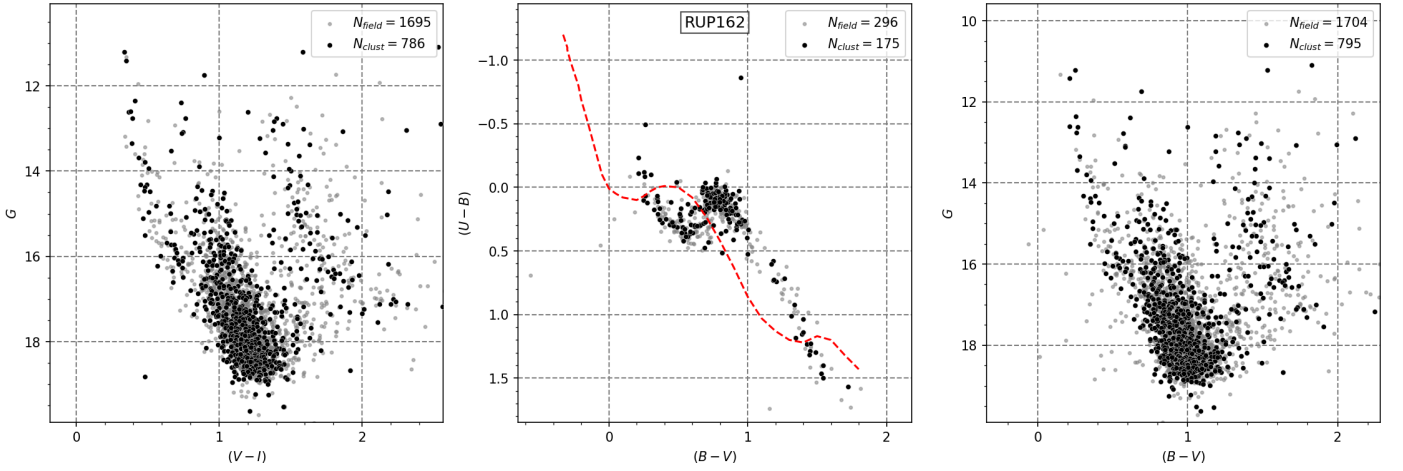


Fig. J.1. Idem Fig. 4 for RUP 162.

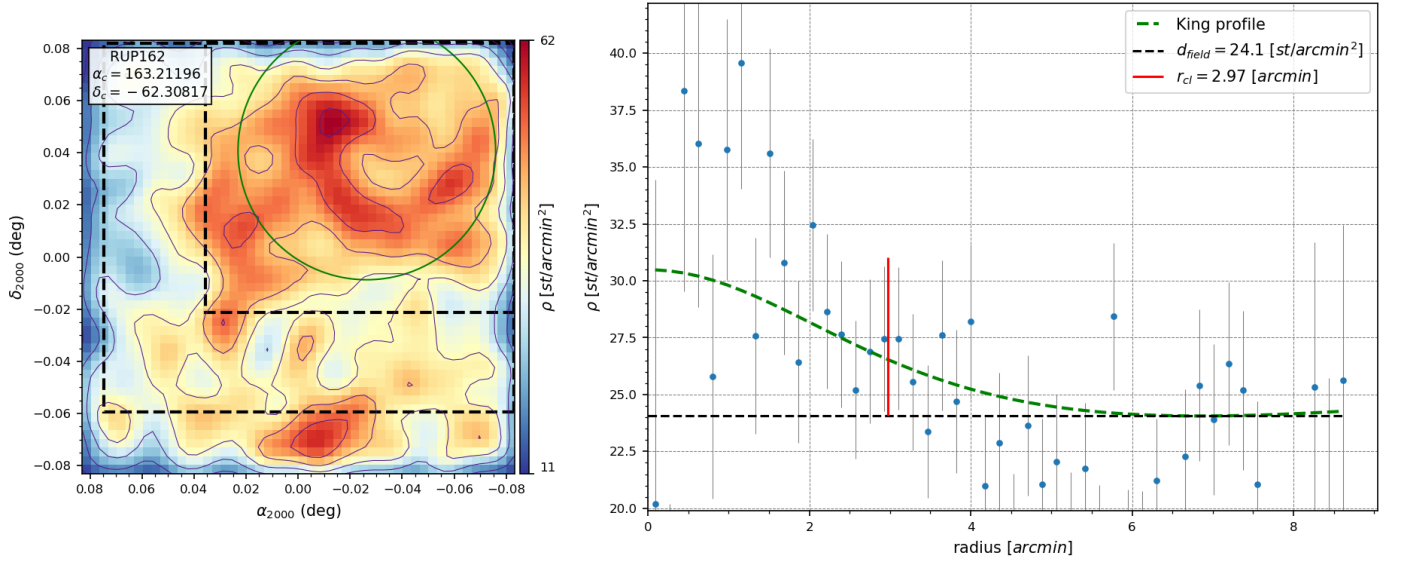


Fig. J.2. Idem Fig. 5 for RUP 162.

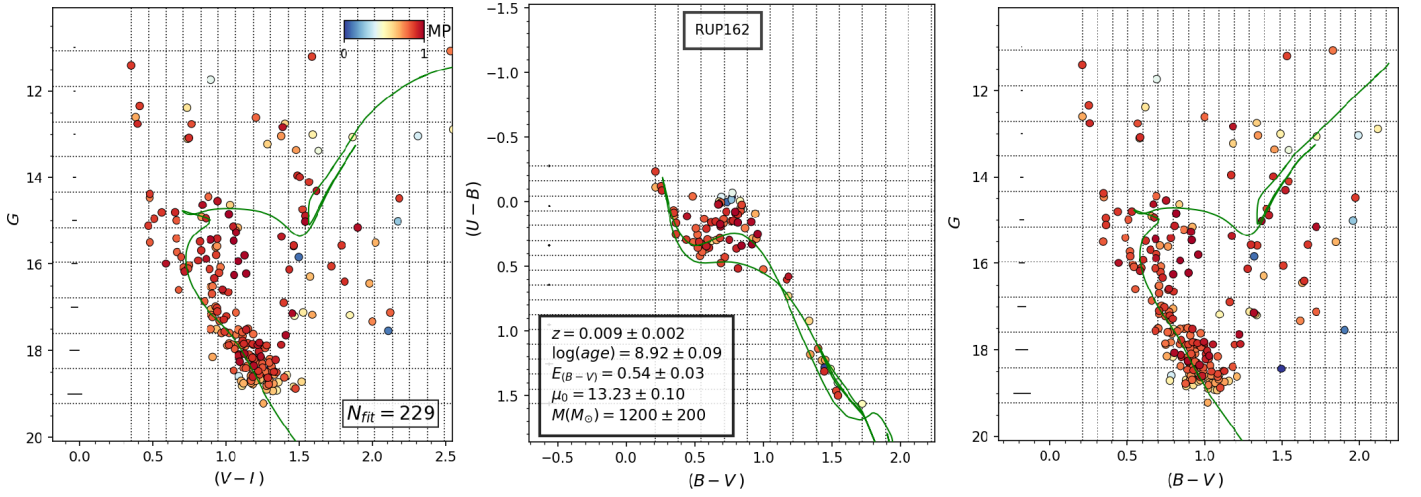


Fig. J.3. Idem Fig. 6 for RUP 162.

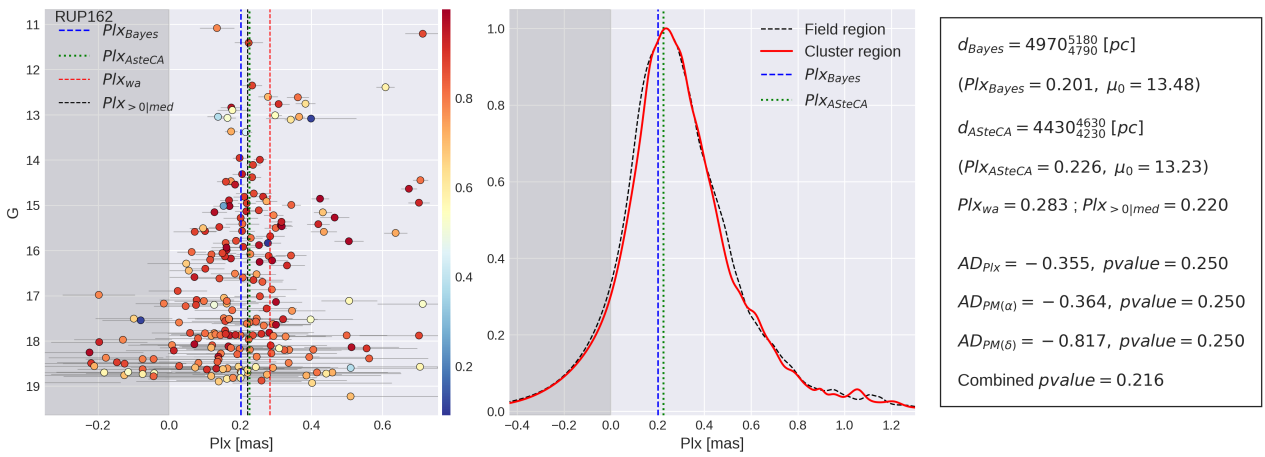


Fig. J.4. Idem Fig. 7 for RUP 162.

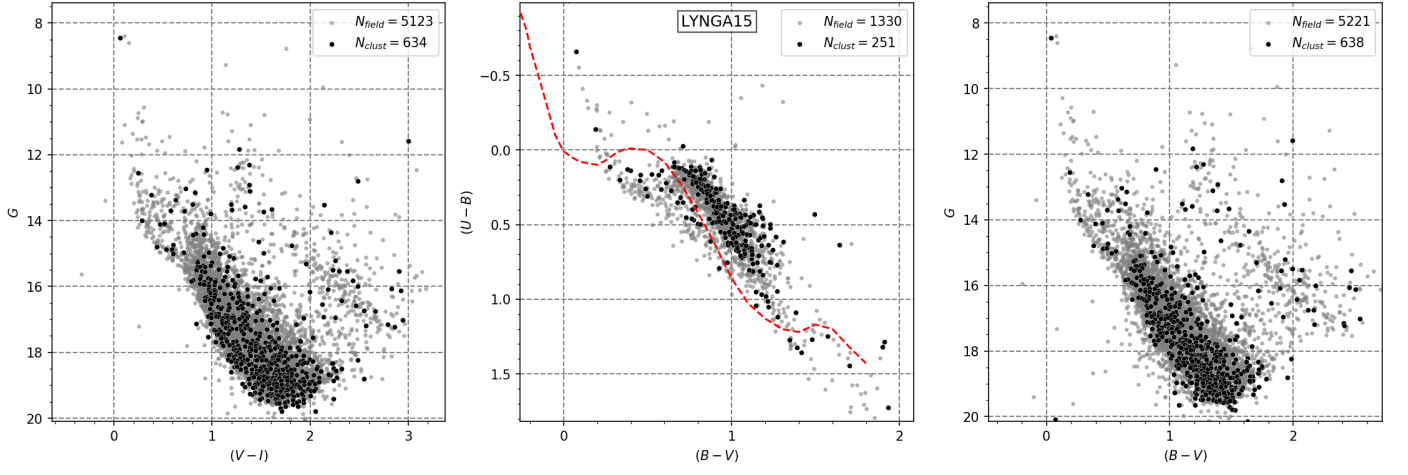


Fig. K.1. Idem Fig. 4 for Lynga 15.

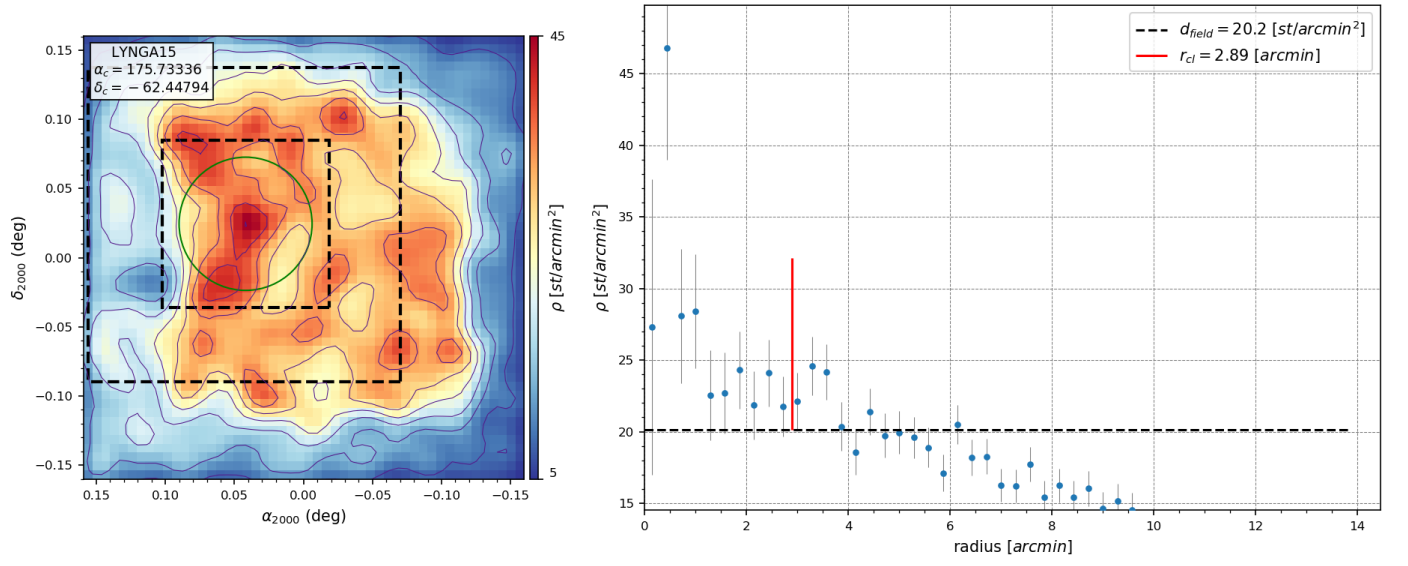


Fig. K.2. Idem Fig. 5 for Lynga 15.

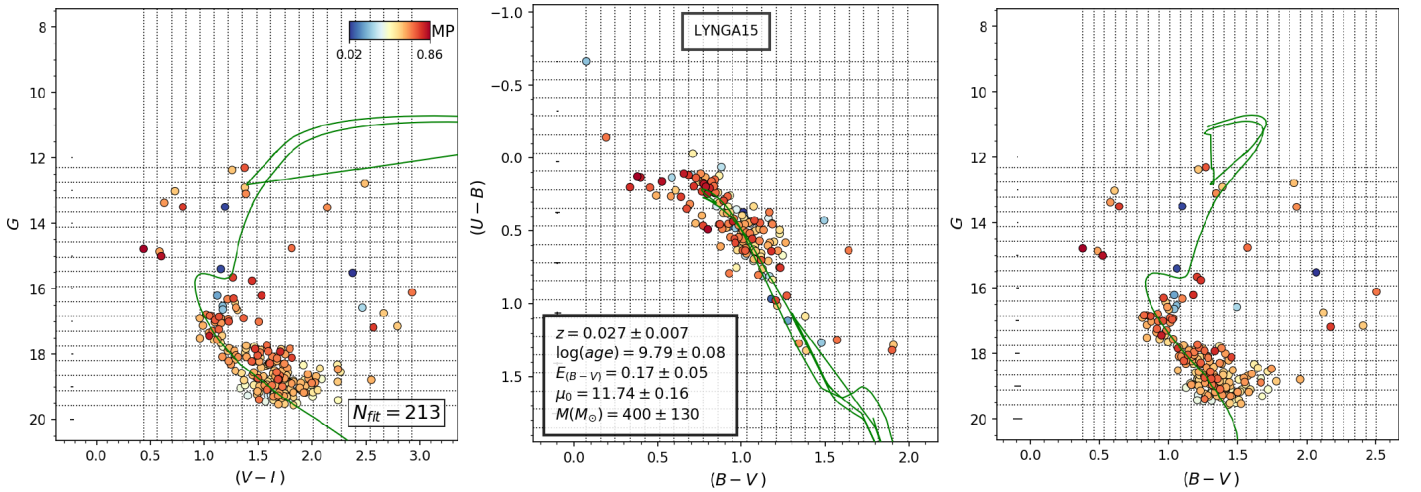


Fig. K.3. Idem Fig. 6 for Lynga 15.

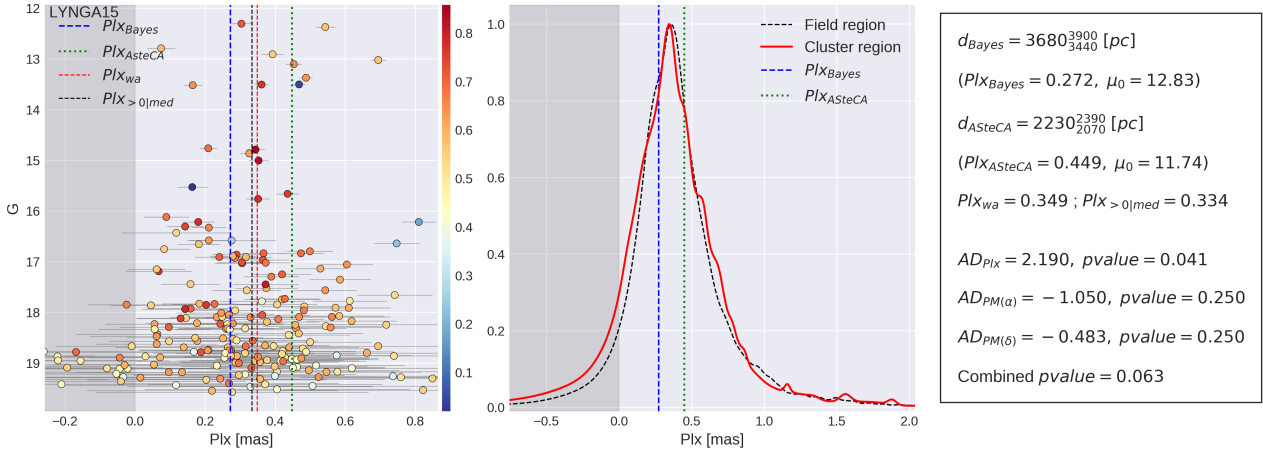


Fig. K.4. Idem Fig. 7 for Lynga 15.

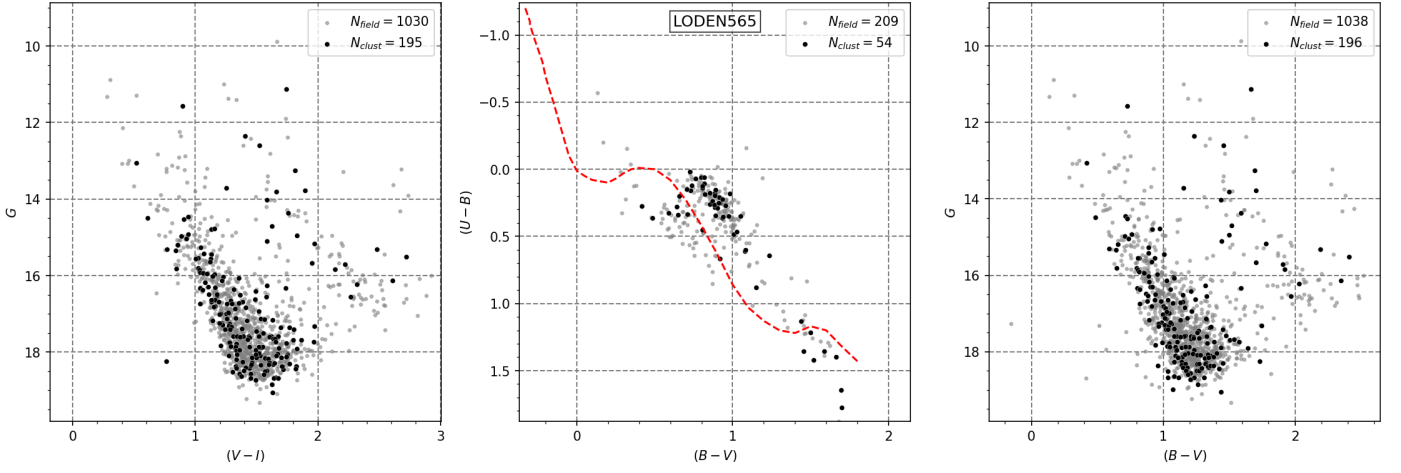


Fig. L.1. Idem Fig. 4 for Loden 565.

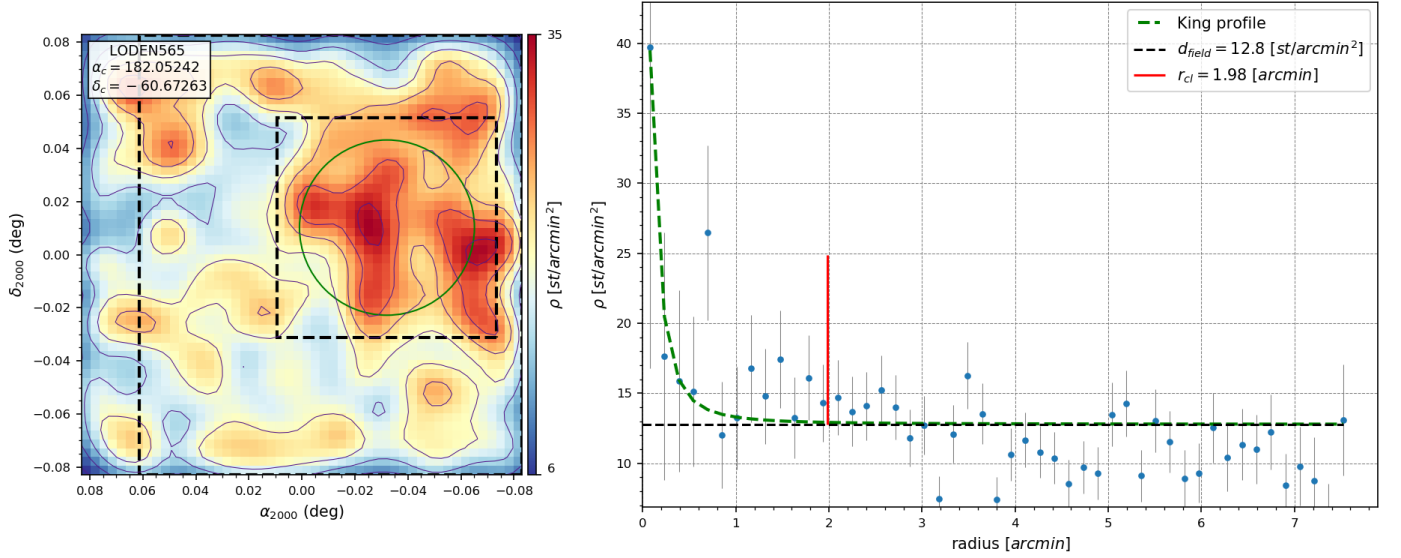


Fig. L.2. Idem Fig. 5 for Loden 565.

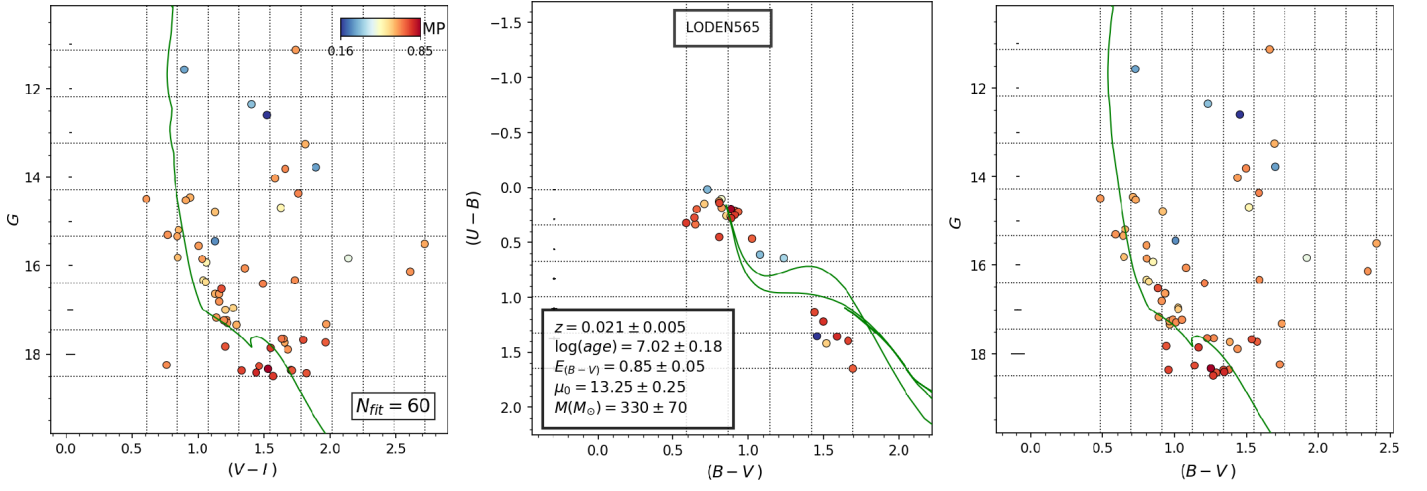


Fig. L.3. Idem Fig. 6 for Loden 565.

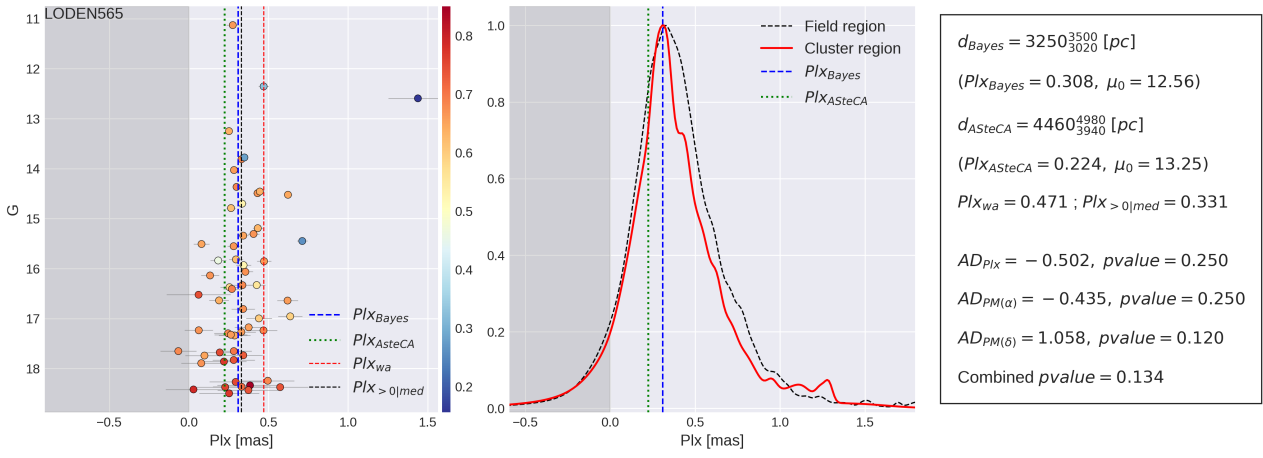


Fig. L.4. Idem Fig. 7 for Loden 565.

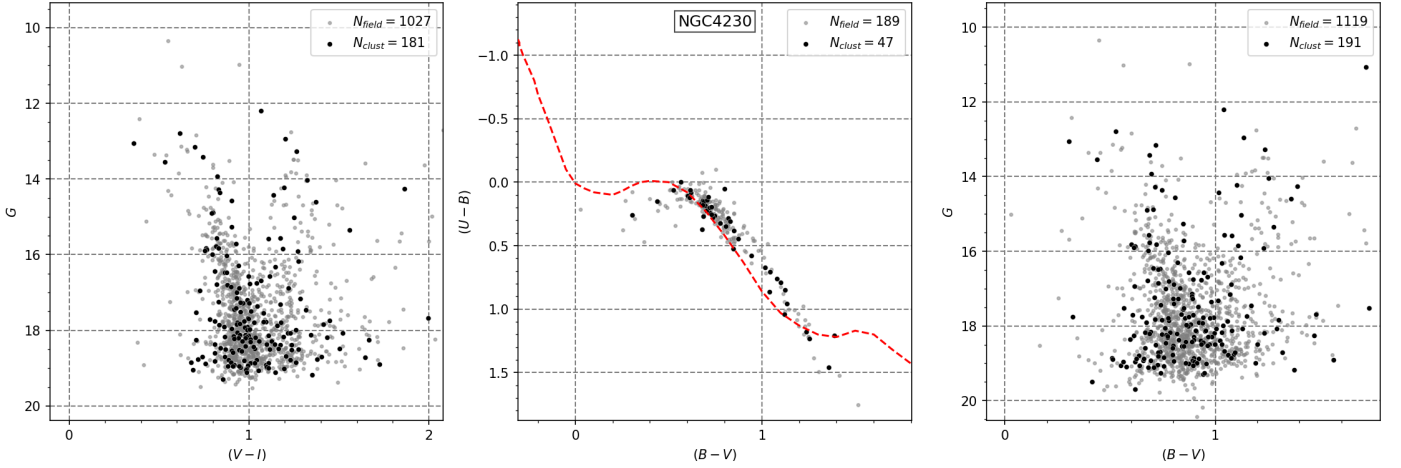


Fig. M.1. Idem Fig. 4 for NGC 4230.

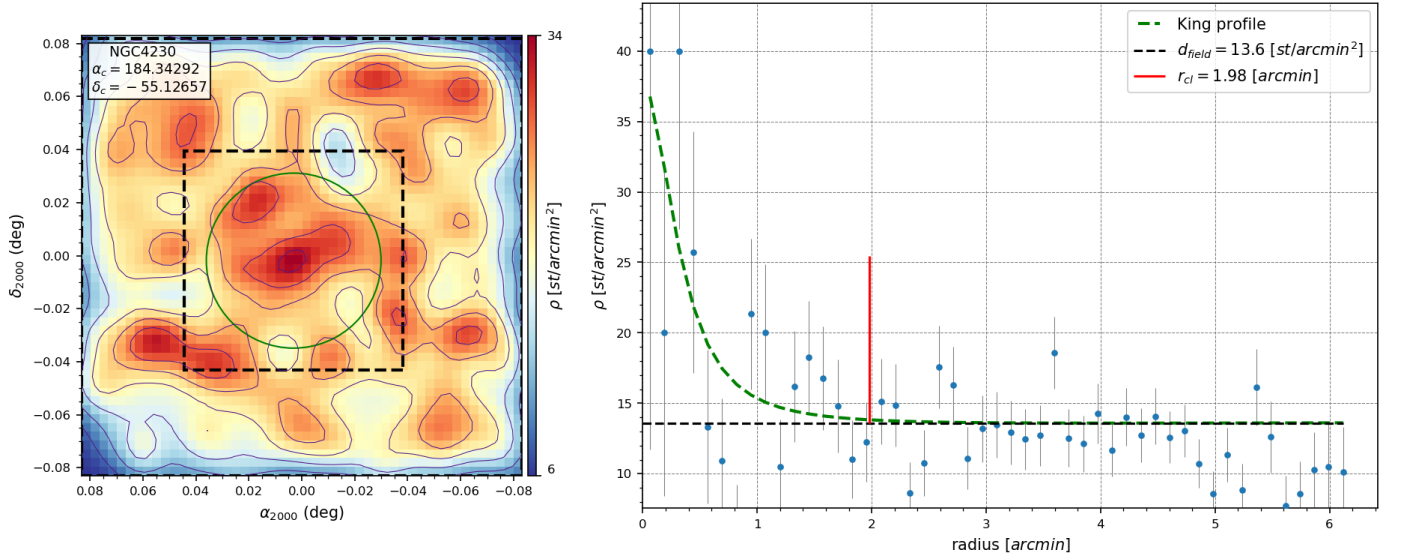


Fig. M.2. Idem Fig. 5 for NGC 4230.

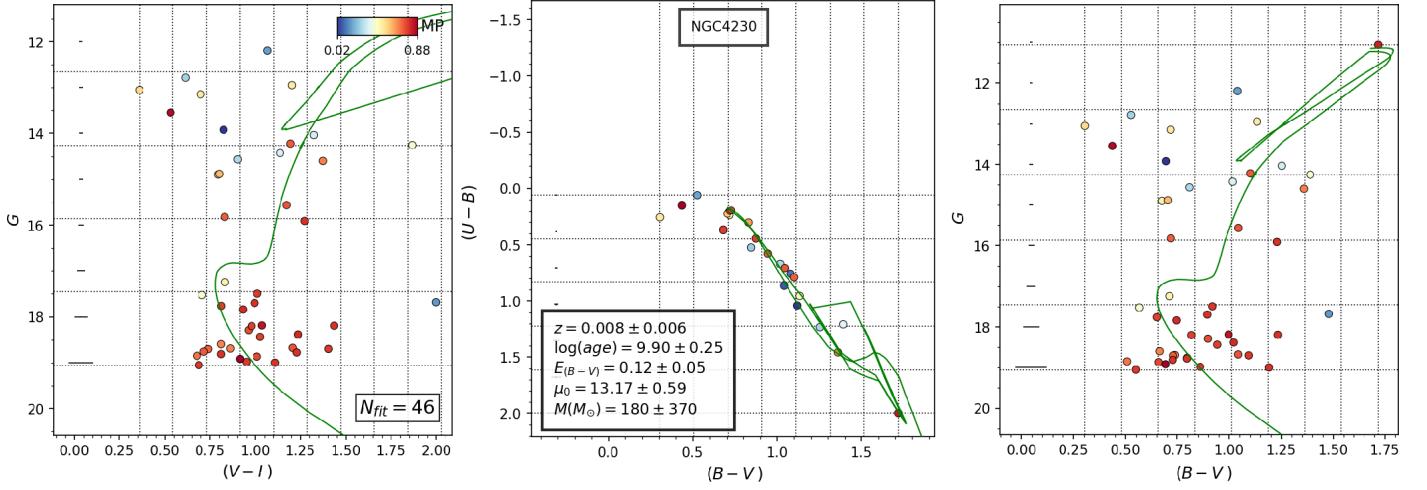


Fig. M.3. Idem Fig. 6 for NGC 4230.

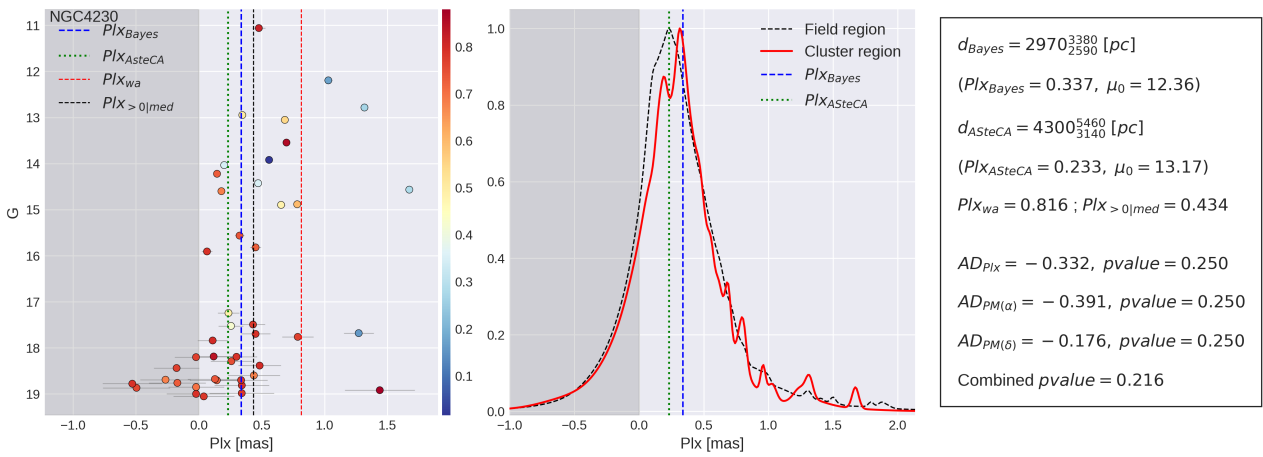


Fig. M.4. Idem Fig. 7 for NGC 4230.